



HAL
open science

Composites with bundle mesostructure : elastic properties and damage

Hana Zrida-Ammar

► **To cite this version:**

Hana Zrida-Ammar. Composites with bundle mesostructure : elastic properties and damage. Mechanics of materials [physics.class-ph]. Université de Lorraine, 2016. English. NNT : 2016LORR0280 . tel-01540873

HAL Id: tel-01540873

<https://theses.hal.science/tel-01540873>

Submitted on 16 Jun 2017

HAL is a multi-disciplinary open access archive for the deposit and dissemination of scientific research documents, whether they are published or not. The documents may come from teaching and research institutions in France or abroad, or from public or private research centers.

L'archive ouverte pluridisciplinaire **HAL**, est destinée au dépôt et à la diffusion de documents scientifiques de niveau recherche, publiés ou non, émanant des établissements d'enseignement et de recherche français ou étrangers, des laboratoires publics ou privés.



AVERTISSEMENT

Ce document est le fruit d'un long travail approuvé par le jury de soutenance et mis à disposition de l'ensemble de la communauté universitaire élargie.

Il est soumis à la propriété intellectuelle de l'auteur. Ceci implique une obligation de citation et de référencement lors de l'utilisation de ce document.

D'autre part, toute contrefaçon, plagiat, reproduction illicite encourt une poursuite pénale.

Contact : ddoc-theses-contact@univ-lorraine.fr

LIENS

Code de la Propriété Intellectuelle. articles L 122. 4

Code de la Propriété Intellectuelle. articles L 335.2- L 335.10

http://www.cfcopies.com/V2/leg/leg_droi.php

<http://www.culture.gouv.fr/culture/infos-pratiques/droits/protection.htm>

THÈSE

Pour l'obtention du titre de:

Docteur De L'université De Lorraine En Mécaniques et Énergétique.

Présentée par :

HANA ZRIDA AMMAR

Les composites avec mesostructure en faisceaux : Propriétés élastiques et endommagement

Thèse soutenue publiquement le 30 mai 2016 à Luleå (Suède) devant le jury suivant :

Prof. Steve Ogin	Department of Mechanical Engineering Sciences, University of Surrey, United Kingdom	Rapporteur
Prof. Yves Berthaud	Université Pierre et Marie Curie, Laboratoire de Mécanique et Technologie, Cachan, France	Rapporteur
Prof. Povl Bronsted	DTU WIND ENERGY, Department of Wind Energy, Technical University of Denmark	Examineur
Prof. Stepan Lomov	Composite Materials Group, University of Leuven, Belgium	Examineur
Prof. Ali Kallel	Laboratoire des Matériaux Composites, Céramiques et Polymères, Université de Sfax, Tunisie	Examineur
Prof. Zoubir Ayadi	Département Science et Ingénierie des Matériaux et Métallurgie-IJL, Université de Lorraine, Nancy, France	Directeur de thèse
Chaired Prof. Janis Varna	Department of engineering sciences and mathematics, division of material science, polymeric composite materials, Luleå university of technology, Sweden	Directeur de thèse

*Institut Jean Lamour –UMR 7198- Département SI2M – Equipe 305
Parc de Saurupt - CS 50840- 54011 NANCY Cedex*

Université de Lorraine – Pôle M4 : matière, matériaux, métallurgie, mécanique

“The important thing is to not stop questioning. Curiosity has its own reason for existence. One cannot help but be in awe when he contemplates the mysteries of eternity, of life, of the marvelous structure of reality. It is enough if one tries merely to comprehend a little of this mystery each day”

“Student: Aren't these the same questions as last year's physics final exam?”

Dr. Einstein: Yes; But this year the answers are different.”

Albert Einstein

Preface

The work presented in this thesis has been carried out within the Division of Materials Science in Luleå University of Technology in Sweden and in the Division of Mechanics of Materials (SI2M) in Jean Lamour Institute in University of Lorraine France during the period from October 2011 to December 2015.

This thesis could not have seen the light of day without the precious support of many persons.

There is no way I can ever thank my both supervisors Professor Janis Varna and Professor Zoubir Ayadi for their unconditional and unswerving help, for their precious time, for their valuable advices, for their patience and for their willingness to listen and their whole-hearted readiness to help when I most need it. Words just fail me whenever I try to express my gratitude for them, thank you for making my research experience ever so unique.

I gratefully acknowledge my co-author Dr. Erik Marklund for his assistance in my research and for shearing his knowledge and for his contributions.

I would like to express also my sincerest gratitude to my co-author Docent Patrik Fernberg for his support and guidance and for his fruitful suggestions and remarks.

It is a pleasure to thank the Joint European Doctoral Program in Material Science and Engineering (DocMase) for financing part of this project. My acknowledgments go also to the local government Norbotten in Sweden for financing part of this research work and also Swerea SICOMP for their support.

I would like to offer my special thanks to Professor Zouhir Fakhfakh from my home country (Tunisia) for his encouragement and his personal support. Special thanks go

also to Professor Roberts Joffe and Professor Lennart Wallström for their kind help. Many thanks go to my colleagues and my friends who were important to the successful realization of my thesis.

Finally, I owe my deepest gratitude to my relatives, my parents, my brother and my husband for their love, prayer, support, care and encouraging words that light my way and kindle my enthusiasm to bring out the best in me in all my academic endeavors.

Luleå, May 2016

A handwritten signature in blue ink that reads "Hana". The signature is written in a cursive style with a horizontal line underneath the name.

Hana Zrida Ammar

Abstract

Many types of composite materials are today used in various types of load carrying structures, due to their excellent strength and stiffness to weight ratio. Simplicity, reliability and low cost of the material processing are important factors affecting the final selection.

With the textile reinforced composites, the cost-efficiency is reached by using dry preforms which are impregnated by resin infusion, resin transfer molding etc.; this have made a break-through and have been widely used.

Textile composites with bundle meso-structure have been studied in this thesis for elastic properties and damage investigations.

In chapter I a state of the art was conducted the different methods for elastic properties determination in composites with bundle mesostructure and mesostructure heterogeneity. The different damage features occurring in such composite materials are also investigated.

Chapter II of this thesis deals with elastic properties modeling for Non-crimp fabric (NCF) based composites for investigating the effect of meso-structure defects on mechanical properties degradation. The objective of the work is to formulate a model for the NCF composite mesostructure in an attempt to investigate the effect of the waviness on stiffness reduction. Moreover, the stiffness calculation methods for the complex geometry are explained and justified and finally, the different geometrical parameters changes are taken into consideration and included in the calculation.

The damage initiation and development is presented in chapter III, where woven fabric composites designated for high temperature application were investigated under severe thermal conditions to study their thermal stability and their resistance to thermal damage. The mechanical performance of the same composites was studied. The effect of aging was also investigated. 3D models were realized with Finite elements in order to explain the edge effect on the evolution of the cracks observed during the tensile tests. In addition, the differences and similarities in cracking in

different layers were analysed using probabilistic approaches (a simple one as well as Monte Carlo simulations with Hashin's and also shear lag model) and fracture mechanics arguments.

List of relevant publications and presentations

Journal papers

[1] H.Zrida., E. Marklund., J.Varna and Z.Ayadi., “Effective stiffness approach for stiffness of biaxial composites with varying local bundle waviness”, International journal of solids and structures, 2016 (submitted)

[2] H.Zrida., P.Fernberg., J.Varna and Z.Ayadi., “Microcracking in thermally aged Carbon fibre/polyimide laminates subjected to tension”, Composites Part B: Engineering, 2016 (submitted)

[3] H.Zrida., P.Fernberg., J.Varna and Z.Ayadi., “Microcracking in thermally cycled and aged Carbon fibre/polyimide laminates”, Composites Part A: Applied science and manufacturing, 2016 (submitted)

[4] H.Zrida., E. Marklund., J.Varna and Z.Ayadi., “Master curve approach to axial stiffness calculation of biaxial composites with bundle waviness”, Composites Part B: Engineering, 2014 (64), 214-221.

[5] H.Zrida., E. Marklund., J.Varna and Z.Ayadi., “Effective stiffness of 0°-layer for stiffness determination of cross-ply non-crimp-fabric composites”, Journal of reinforced plastics and composites, 2014 (33), 1339-1352.

Conference papers

[6] H.Zrida., P.Fernberg., J.Varna and Z.Ayadi., "Effect of extreme temperatures on micro-damage development in CF/polyimide laminates", Conference paper: 20th international conference on composite materials ICCM 2015, Copenhagen, Denmark.

[7] H.Zrida., MS.Loukil., J.Varna and Z.Ayadi., "Crack opening displacement determination in damaged cross-ply laminate using electronic speckle pattern interferometry (ESPI)", Conference paper: IOP Conference series: Materials Science and Engineering, 2012

[8] H.Zrida., K.Giannadakis., J.Varna and Z.Ayadi., "The effect of meso-structure heterogeneity on the cracks initiation and the displacement distribution in NCF composites", Conference paper: IOP Conference series: Materials Science and Engineering, 2012

List of Conference Presentations

- ✓ 20th International conference on composite materials (**ICCM**) **July 2015**,
Copenhagen, Denmark (**Oral presentation**)

- ✓ 18th International conference on mechanics of composite materials (**MCM**),
June 2014, Riga, Latvia (**Oral presentation**).

- ✓ International conference on composite materials and renewable energy
applications (**ICCMREA**), **January 2014**, Sousse, Tunisia (**Oral presentation**).

- ✓ International conference **DFC12/S16**: 12th Deformation and fracture of
composites and 6th Structural Integrity, **April 2013**, Queen's College Cambridge,
United Kingdom (Oral presentation).

- ✓ 6th **EEIGM** International conference in Advanced Materials Research,
November 2011 Nancy, France, (**2 posters**).

Contents

Dedication.....	i
Preface	ii
Abstract.....	iv
List of relevant publications and presentations	vi
Chapter I. State of the art.....	2
1. Introduction: Fibre reinforced composites	2
2. Mechanical properties in composites with bundle meso-structure.....	6
3. The damage features in textile composites.....	9
3.1. Matrix crack (intralaminar cracking).....	10
3.2. Delamination (Interlaminar cracking)	11
3.3. Fibres break	11
3.4. Matrix cracks in bundles structures composites	12
3.4.1. Longitudinal cracks	13
3.4.2. Whole cracks (Transverse cracks).....	13
3.4.3. Half cracks (Transverse cracks)	14
3.4.4. Double cracks (Transverse cracks).....	14
3.5. More studies on damage accumulation in textile composites	15
Chapter II. Effect of mesostructure defects on elastic properties of textile composites	19

1. Introduction	19
2. FE modelling procedure (Material, geometry and assumptions)	23
3. Effective stiffness determination using isolated beam subjected to appropriate boundary conditions	26
3.1. Meso-scale homogenization	29
3.2. Effect of wavelength and amplitude on laminate stiffness.....	30
3.3. Predictions based on isolated curved layers with boundary conditions used in previous studies	31
3.4. The layers effective stiffness dependence on A/t_0 and L/t_0	32
3.5. Approximation of tractions at the 0/90 layer interface.....	36
3.6. Composite stiffness based on effective stiffness of an isolated 0-layer with surface loads.....	39
4. Effective stiffness determination using master curve approach	43
4.1. NCF stiffness knock down factor	47
4.2. Master curve approach.....	48
4.2.1. Knock down factor curve and fitting function.....	48
4.2.2. Validation and application of the master curve approach	50
5. Master curve approach for effective stiffness of composite with more complex geometries.....	56
5.1. Geometries.....	56
5.2. Development of the master curve approach	58
5.3. Engineering approach for the amplitude and wavelength's of an equivalent cell	60
5.4. Stiffness of chain of cells.....	63

5.5. Interaction effects of curved bundles in cells connected in parallel.....	65
6. Conclusions	73
Chapter III. Damage in carbon fibre/polyimide laminate	79
1. Introduction	79
2. Objectives	81
3. Experiments	81
3.1. Materials description	81
3.2. Experimental procedure.....	83
4. Results and discussions	85
4.1. Void content and initial damage state.....	85
4.2. Damage state at RT in thermally cycled composites.....	92
4.3. Damage state at RT in aged composites	97
4.4. Damage state in mechanically loaded composites	102
4.5. Damage accumulation analysis	107
4.5.1. Theoretical background	107
4.5.2. Multiple cracking in 90-+45 layers of not aged (NA) composites	112
4.5.3. Multiple cracking in 90-+45 layers of (A) composites	118
4.5.4. Extraordinary cracking pattern in -45layers	120
5. Conclusions	122

Chapter IV. Summary, conclusions and perspectives.....	125
Acknowledgments	129
Appendix A	130
References	132

Chapter I

State of the art

1. Introduction: Fibre reinforced composites

The quest of weight gain using materials with superior specific properties, engages the interest of many researches to explore composite materials. Each year, composites find their way into hundreds of new applications from golf clubs and tennis rackets to jet skis, aircraft, missiles and spacecraft.

Composite materials are widely used in different areas such as aeronautics (helicopter blades, pressure bulkhead, cargo door, etc), maritime transport (boats, etc), automotive industry (car roof, car carline, etc), electronic (insulation, mounting printed circuit, boards, etc), buildings (furniture, roofing, etc), industry (tanks, pipes, wind turbine blades, etc) and even in sports and entertainment (skis, fishing rods, helmets, etc)...

A composite material consists of an assembly of different immiscible materials which complement each other and bring about a material whose physical properties are better than those of the individual constituents working separately.

Polymer composites are formed with reinforcement in the form of particles or fibres embedded in a matrix. The matrix is often a thermoplastic or a thermoset polymer. The matrix preserves the geometric arrangement of fibres, protects them from the environmental attack and damage, to which the sample can be exposed. The fibres can have inorganic or organic nature such as carbon fibres, glass fibres, oxide fibres, silicon

carbide fibres, etc. They can be continuous or discontinuous filaments. The high stiffness and strength of polymer composite materials stems from the high stiffness and strength of fibres. Their geometry allows them to have minimal defects and their composition gives them a high strength. The fibres work as reinforcements since the load is transferred to them from the matrix. The volume fraction of fibres for a structural composite is typically 45%-65%. The maximum theoretical value is 79% for square array and 91% for a hexagonal array [1].

The fibres can be arranged in different ways: homogeneously or uniformly dispersed like in pre-impregnated tape laminates or in form of bundles like in the woven reinforced composites or the non-crimp fabric composites.

The pre-impregnated tape laminate, shown in **Figure I-1 [2]**, is a stack of unidirectional plies in which the layers are perfectly bonded to each other and the mechanical properties depend on their orientations.

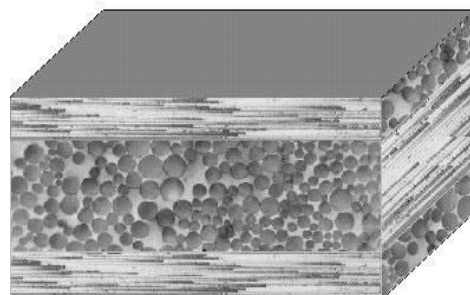


Figure I-1. Internal structure of pre impregnated tape based cross ply laminate [2]

The main advantage of this material is the high fibre volume fraction that can be obtained with well aligned fibres, showing an excellent in-plane stiffness and strength.

The problem with this material is that it is expensive. The high costs combine the high

labour costs and the high storing costs (pre-impregnated tapes require low temperature to prevent curing). Another drawback is the sensitivity to inter-layer delamination cracking under impact loading due to their poor interlaminar fracture toughness [3].

This problem is solved with woven composites shown in **Figure I-2 [4]**, the reinforcing fibres are assembled in bundles in different directions and form a fabric.

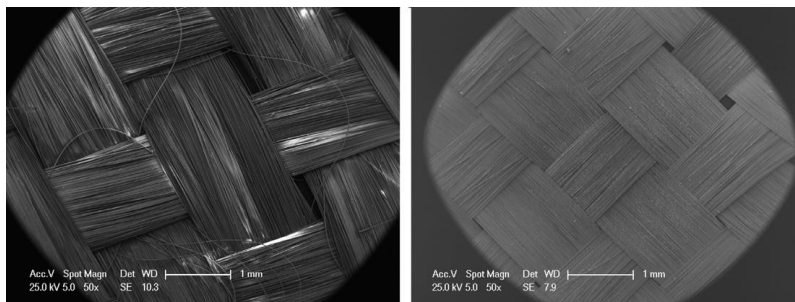


Figure I-2. Images of E-glass (left) and basalt (right) woven fabrics [4]

This composite has two-directional reinforcement and its manufacturing cost is lower than that of the pre-impregnated tape based composite. The woven structure shows high waviness in the out-of-plane direction. This waviness brings advantages to the material by improving its fracture toughness and its mechanical properties in the out-of-plane direction. But, it brings also significant drawbacks to woven composite by reducing the in-plane properties.

Some drawbacks of the pre-impregnated tape based composites and of the woven composites are overcome with new type of textile composite called non-crimp-fabric composites (NCF) presented in **Figure I-3 [5]**.

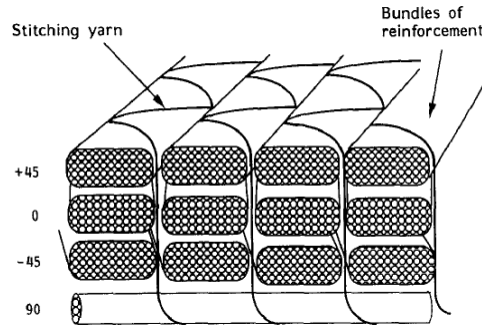


Figure I-3. Schematic diagram showing a multi-axial non-crimp fabric [5]

NCFs are relatively new class of textiles in which a fabric is constructed of layers of fibre bundles aligned in specific directions [6]. The layers of fibres are produced by laying tows next to each other in a specified direction and subsequently employing a secondary fine yarn knitted around the tows to hold the fabric in place. The use of through-thickness stitching allows for improvement in damage tolerance and in the interlaminar fracture toughness. For textile composites (woven and NCF), the manufacturing technique provides a dry preform (fabric) which can be used in complicated shapes before it is consolidated into the final composite by resin transfer moulding with low manufacturing costs comparing to the pre-impregnated tape based composite. NCF composites, ideally, would combine a good in-plane response, like pre-impregnated tape based composites and the good through-thickness stiffness and strength due to the stitching in the thickness direction [7].

With bundle mesostructure, the woven and NCF composites show heterogeneities in the micro- and the meso –scale as shown in **Figure I-4** [8]. The micro-scale heterogeneity can be seen from the microstructure of the fibre-matrix inside the bundles, the meso-scale heterogeneity is due to the structure of layers where the fibre bundles are separated by the matrix.

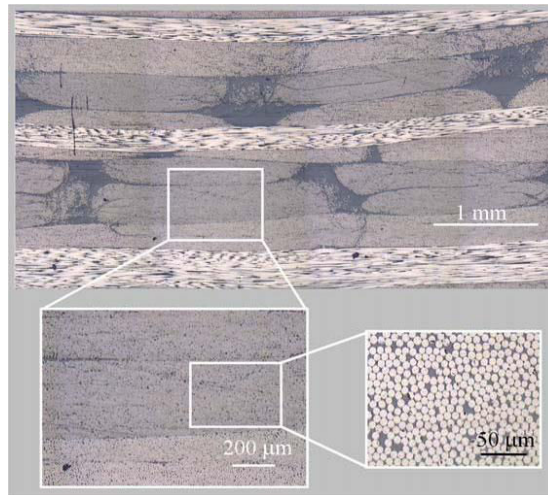


Figure I-4. Hierarchical structure of the NCF composites [8]

As it is shown in **Figure I-4**, the 0° -tows are far from being ideally oriented and present waviness in the out-of-plane direction. The stitching yarn induces waviness which leads to the in-plane stiffness reduction. The waviness occurring in NCF composites are similar to that can be seen in woven reinforced composites with lower amplitudes.

2. Mechanical properties in composites with bundle mesostructure

In order to study the mechanical properties dependence on the architecture parameters, finite element analysis and theoretical analysis methods are more convenient than the experimental techniques because of the complex geometry and the numerous parameter controlling the mechanical behaviour of the textile composites [9-10].

Finite element method (FE) started with Ritz who developed an effective method for an approximate solution of problems in the mechanics of deformable solids [11-12]. FE

is a numerical method for finding approximate solutions to boundary value problems for differential equations. It uses variational methods to minimize an error function and produces a stable solution. The problem is transformed to an equivalent one in terms of properties and geometry and the method is based on the discretization principle which is translated by the choice of a mesh that occurs by dividing the studied area into sub-domains with simple geometry (triangle, quadrilateral, etc) and with finite dimensions, hence the finite element method's name. Results are determined for each element. The accuracy of the results is directly related to the mesh quality realized (number of element, their distribution in the structure, form of element, etc). In FE analysis many errors can be produced, such as wrong interpretations of the physical model, mechanical modelling errors due to many assumptions like geometric simplifications and resolution errors which are due to problems of numerical accuracy. The engineer must be aware of the existence of these errors and must be able to estimate a level of confidence in the results.

Many researches have been conducted for predicting the mechanical properties of textile composites. The basic principle to determine the elastic properties of a textile composite using FE is to divide the structure into unit cells and then mechanical properties are calculated for the unit cell.

Since the textile composites have a complex architecture it is not easy to incorporate all geometrical parameters and simplifications are needed in the FE modelling [13].

Naik et al. [14-16] proposed a 2D crimp model for the elastic analysis of a 2D plain weave. The unit cell in this model was divided into sections and then the series-parallel

models were used to estimate the lower and the upper bounds of the elastic constants.

Ishikawa and Chou developed the “mosaic” model [17], the “fibre undulation” model [18] and further the “bridging” model [19] for analysing the elastic behaviour of woven hybrid composites. In these models a fabric composite was simply regarded as an assembly of blocks of cross-ply laminates neglecting the shear deformation in the thickness direction.

Byström et al. [20] developed a homogenization method for stiffness matrix computation of woven composites; the method was called reiterated homogenization. The authors studied the linear elastic problems with periodic microstructure, which justifies the use of representative volume element which is enough to represent the elastic properties of the whole material.

More recent study was performed by Riccio et al. [21] who developed a representative volume element (RVE) for NCF composites under tension loading taking into account the tow’s waviness and the stitching. The classical micromechanical theory was used together with the stiffness averaging method. It was demonstrated that the exclusion of the tow’s waviness from the model leads to a big error of the stiffness comparing to the experimental data. However, the lack of stitching in the model is less relevant leading to a small error that can be neglected. The stiffness dependence on the tow’s waviness was investigated and it was shown that this stiffness strongly depends on the waviness.

A mesoscopic FE model of the NCF structure was realized by Drapier [22] in order to investigate the interlaminar shear behaviour of non-crimp fabric composites. The

geometrical heterogeneity was taken into account. The tow's crimp was considered large enough for the composite to be regarded between the pre-impregnated tapes and the woven structures. This waviness was assumed as sinusoidal shaped characterized by a wavelength and amplitude. The same assumption was used in [23] by Edgren et al. where the authors used Timoshenko beam theory in addition to FE to calculate the stiffness of a layer in the NCF composite considered like a single curved beam. In addition to this assumption, Mattsson et al. [24] demonstrated that the 90°-layer with bundle mesostructure can be replaced by homogenized 90°-layer without losing accuracy in the NCF laminate stiffness investigation.

One more important geometric parameter that should be taken into consideration while modelling textile composites, is the inter-strand gap between the bundles, it has been demonstrated in [25] that a change in the inter-strand gap width leads to a significant modification of the elastic properties (elastic modulus, shear modulus and Poisson's ratios) because of the change of the fibres volume fraction and the matrix volume fraction inside the layers.

3. The damage features in textile composites

In order to have confidence in the structural integrity of composite components, designers must have a good understanding of the effect of stress concentrations which lead to the damage. Studies of initiation of cracks, their growth characteristics and their effect on the laminate properties belong to an active field of study called damage mechanics, playing a central role in the assessment of durability and damage tolerance of composite structures.

Composite structures can undergo multiple micro-cracks before losing ability to carry the design loads. The damage mechanisms occurring in textile composites are basically the same as in pre-impregnated tape based composites. It mainly consists of matrix cracking, delamination and fibres fracture [26] presented in **Figure I-5**.

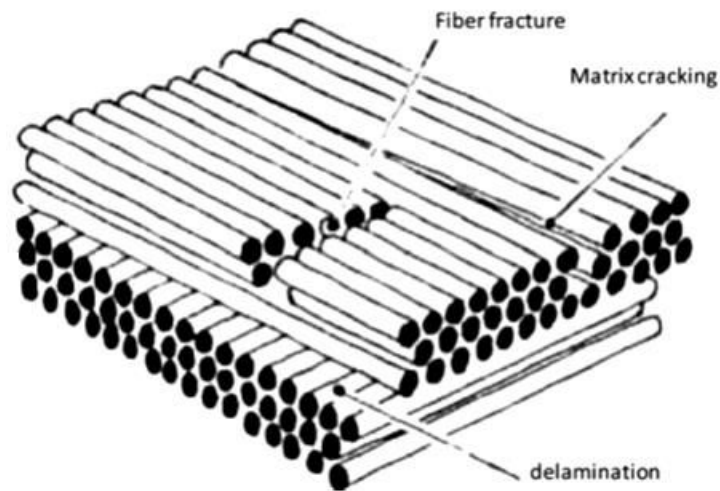


Figure I-5. Damage mechanisms in laminates [27]

3.1. Matrix crack (Intralaminar cracking)

The stiffness and strength of fibre reinforced composites are higher in the longitudinal direction than in the transverse one. In addition, the stiffness of the reinforcing fibres is significantly higher than the matrix material. Thus, stress concentrations occur in the matrix when a ply is loaded in the transverse direction. The stresses at which the failure occurs in off-axis ply are lower than that of plies aligned in the loading direction. In the off-axis plies, the cracks develop and run parallel to the fibres direction. These cracks are usually the first mode of damage in fibre-reinforced composites. Such cracks are caused by tensile loading, fatigue loading, as well as by changes in temperature or by thermal cycling. Matrix cracks do not cause a total failure of the composite, but may

lead to significant degradation of the elastic properties and to appearance of other damage modes. An example of matrix crack is presented in **Figure I-6**.

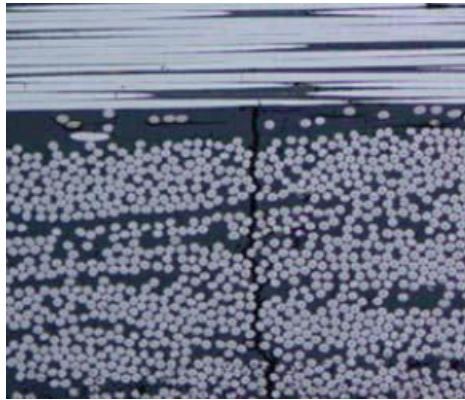


Figure I-6. Matrix crack [28].

3.2. Delamination (Interlaminar cracking)

The delamination is a longitudinal crack in the interface between two adjacent plies. Its propagation leads to the separation of the layers. This mode of damage causes the rapid deterioration of the mechanical properties and the total failure of the composite structure. An example of delamination is presented in **Figure I-7** where it shows how it is starting from the matrix crack tip.

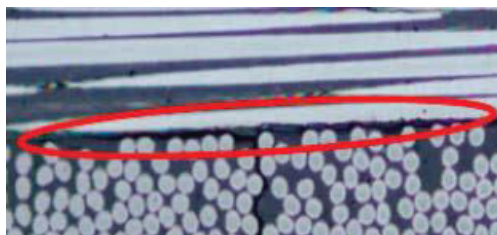


Figure I-7. Delamination starting from a matrix crack tip [28]

3.3. Fibres break

As its name says, it is the breaking of the fibres oriented parallel to the loading direction. In a unidirectional composite loaded in tension along the longitudinal direction, the fibres fail at their weak points and stress redistribution between fibres and matrix occurs, affecting other fibres and breaking more of them. An example of broken fibres is presented in **Figure I-8**.

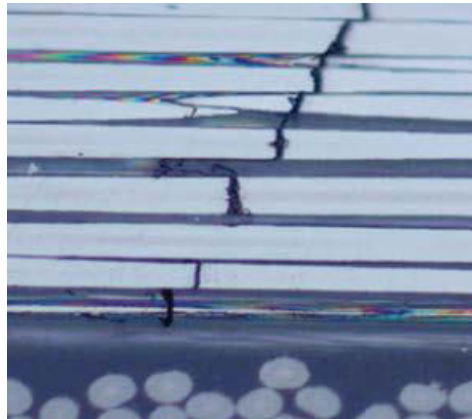


Figure I-8. Broken fibres [28]

3.4. Matrix cracks in bundle structured composites

Damages can occur in the textile composites in different length scale, either on the micro scale or on the meso scale. **Figure I-9** represents the different types of cracks occurring within the fibre bundles introducing after a tensile test.

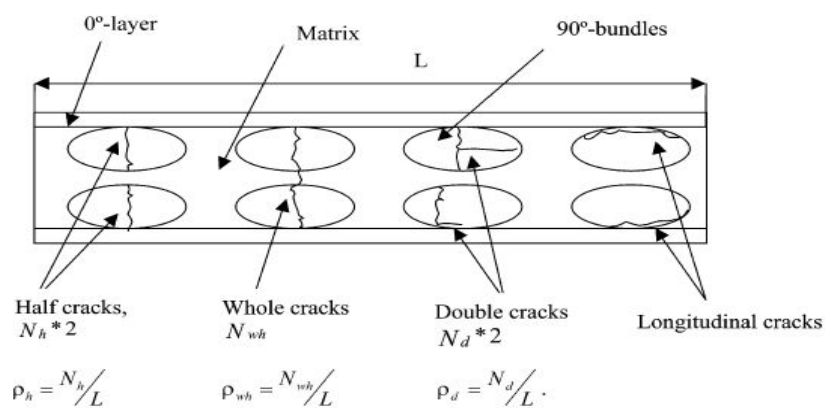


Figure I-9. Schematic showing the four crack types observed in NCF cross-ply laminates ρ_i refers to crack densities of the different type of cracks [29].

The maximum cracks density is inversely proportional to the ply thickness [30].

3.4.1. Longitudinal cracks

Longitudinal cracks are presented in **Figure I-10**. They can appear either within the bundle or at the bundle-matrix interface. They occur on the loading direction and they appear at high strains. This type of cracks never occurs in composites with uniform fibre distribution. They can appear due to fibres tow waviness at strains between 0.39% and 0.66 % [29-30].

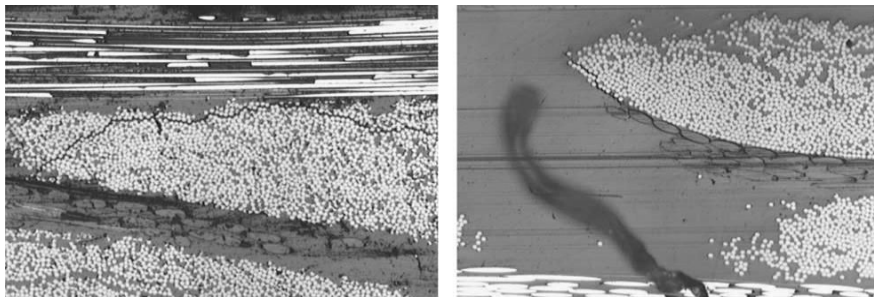


Figure I-10. Micrograph of novel longitudinal cracks occurring in the 90°layer of the NCF cross-ply laminate [29]

3.4.2. Whole cracks (Transverse cracks)

Figure I-11 shows some whole cracks which extend from one 0°layer to another through two neighbouring 90°fibre bundles [29].

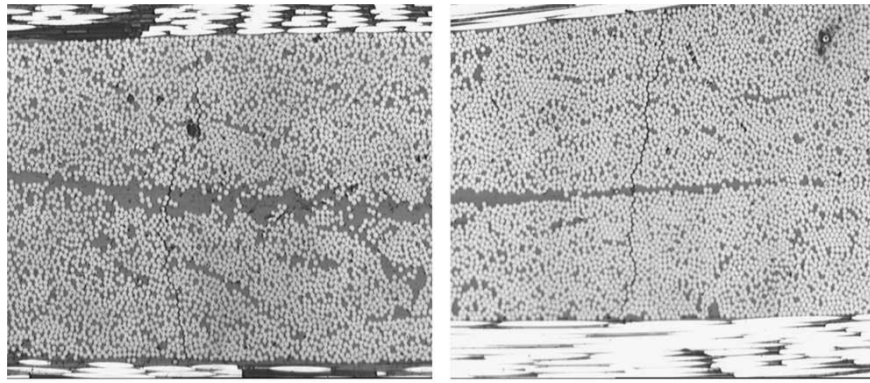


Figure I-11. Examples of whole cracks running through two neighbouring 90° fibre bundles of the cross-ply NCF laminate [29]

3.4.3. Half cracks (Transverse cracks)

Figure I-12 shows the half cracks which are contained in a single 90° fibre bundle without connection with others existing in adjacent fibre bundles. This is the first type of cracks to occur in NCF composites [29].

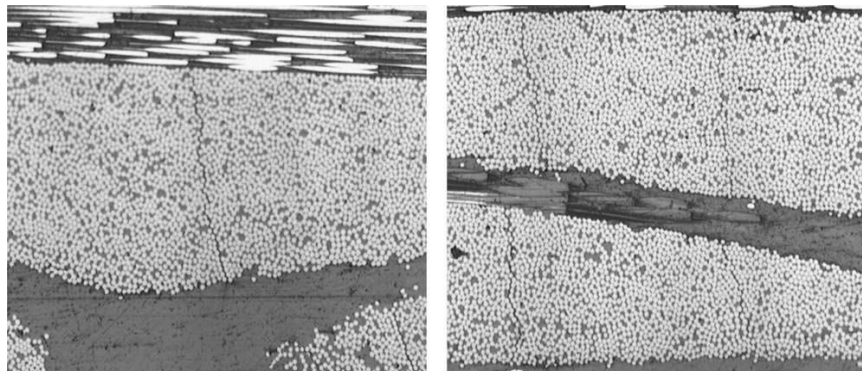


Figure I-12. Examples of half cracks in 90° fibre bundles of the cross-ply NCF laminate [29]

3.4.4. Double cracks

Figure I-13 shows double cracks which are a combination of half crack and longitudinal crack. They occur within a single fibre bundle [29].

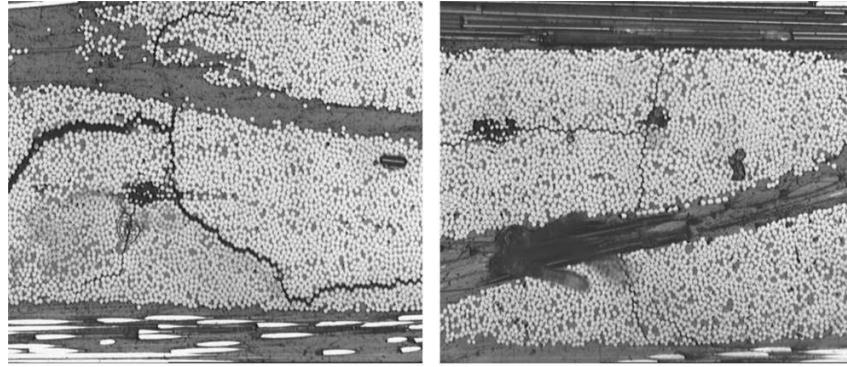


Figure I-13. Examples of double cracks in single 90° fibre bundles of the cross-ply NCF laminate [29].

The same type of cracks were also characterized and studied by John et al. [31] in 3D woven Fabric.

Edgren et al. demonstrated in [29] that the amount of whole cracks found in NCF composites is small and doesn't exceed 0.25cr/mm. The half cracks are more abundant than whole cracks and appear earlier. But their effect on stiffness degradation is moderated in NCFs comparing to the pre-impregnated tape based composites. It was proved that the 90° layer's damage doesn't have an important effect on the Young's modulus which decreases slightly, since the laminate modulus is mainly controlled by the 0° non-damaged laminate. However, it has a strong effect on the degradation of the Poisson's ratio because the transverse cracks increase the strain in the load direction and reduce contraction in the transverse direction. The appearance of the new longitudinal cracks was explained by the stress concentration caused by the forced straightening of the 0° fibre bundles in tension.

3.5. More studies on damage accumulation in textile composites

The complexity in geometry of the damage and its quantification has made the progress in studying the effect of the damage accumulation on the mechanical properties in textile composites slower than in composites with uniform fibres distribution.

Gao et al. [32] have studied the relationship between the mechanical properties and the damage accumulation in woven fabric laminate under quasi-static loading. The shear lag analysis, originally derived for the pre-impregnated tape based laminate, were employed idealized laminate replacing the woven one (**Figure I-14**), since in the studied eight-hardness satin fabric, the inter-crimp distance is quite large. It has been demonstrated that the Young's modulus is affected little with the accumulation of matrix cracks and crimp delaminations until the saturation of the crack density. The Poisson's ratio was much more sensitive to the damage.

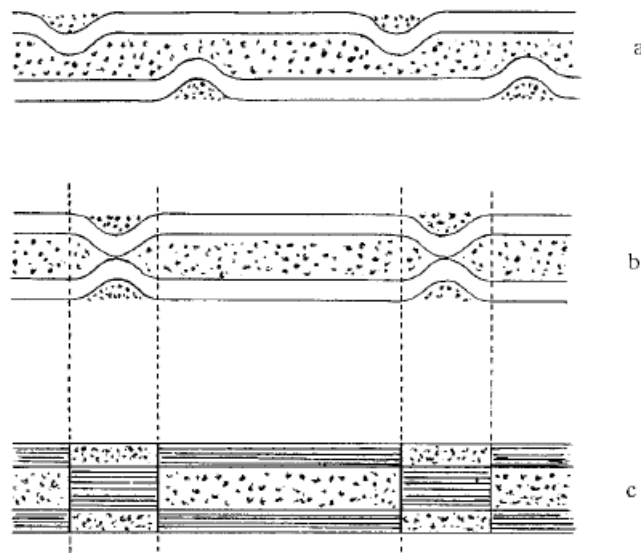


Figure I-14. Idealization of two layer woven fabric laminate [32]

Lomov et al. [33] presented an experimental methodology to study the initiation and development of damage in textile composites in tension test, which was applied to

different textiles: woven and NCFs. This methodology is based on full field strain measurement for studying the strain map, on a X-Ray inspection for studying the cracks placement, orientation and their length distribution, on a C-Scan for the damaged samples in order to study the damage extend and periodicity and finally on SEM for micro-characterization of damage.

The damage pattern in NCF composites was studied in [34], it was demonstrated that the cracking occurs periodically showing that there is a relation between the stitching and the damage pattern.

During the service life, the composite materials are not only exposed to mechanical loading but also to thermal loads. In [35], the effect of accelerated aging condition on woven fabric composite was analysed. A glass fibres eight-hardness satin weave with two different epoxy matrices (120°C and 180°C) was studied. When the fibres are protected with better matrix they are less sensitive to the thermal aging effect and they have better performance under mechanical loading.

Chapter II

Effect of meso-structure defects on elastic properties of textile composites

1. Introduction

Due to high material costs and sensitivity to out-of-plane loads (e.g. impact damage) of pre-impregnated tape based composites, new manufacturing methods and material architectures based on dry preforms have been employed in the last decade producing civil aircraft primary structures. Non-crimp fabric (NCF) reinforced composites are particularly attractive due to their relatively high performance with less drop in the in-plane properties compared to traditional woven architectures, reasonable cost and ease of handling during manufacture. As a result there is a strong interest among aircraft manufacturers and within other sectors such as wind energy and automotive industry, to use NCF based composites in primary structures.

NCF composites are manufactured from layered textile preforms consisting of fibre bundles with a certain orientation assembled by warp-knitted threads [36]. This production technique allows for substantial reductions in production costs compared to pre-impregnated tape based materials. In addition improvements in damage tolerance as well as out-of-plane fracture toughness have been reported [37-39]. During composite manufacture, preforms are stacked in a mould and infiltrated by a thermoset resin to form the composite. Thus an NCF composite is created which is heterogeneous not only on microscale (fibres and resin) as for pre-impregnated based

composites, but also on mesoscale due to the appearance of distinct fibre bundles and resin pockets. Since the bundle scale is much larger than the fibre scale, homogenization over the fibre/matrix scale is possible representing the bundle as transversally isotropic material.

Ideally, NCF composites would consist of perfectly aligned fibre bundles where the size of each bundle is determined by the stitching procedure. However, due to the complex manufacturing technique, NCF composites have both in- and out-of-plane waviness of the bundles which reduces the in-plane stiffness. In [22,40] experimental data regarding the measured out-of-plane waviness are discussed, and the waviness in terms of sinusoidal shape was used in a 2D FE-model of a composite with periodic structure in the thickness direction and a biaxial NCF as a repeating unit cell (RUC) in order to study the effect of the parameters defining the 2D mesoscopic model on the NCF compressive strength. It has been shown that the NCF compressive strength is controlled by the 0° -tow geometrical instability and by the resin shear plastic flow.

In the sense of the out-of-plane waviness the architecture of real NCF composite described above and shown in **Figure II-1a** has similarities to woven fabric composites; see **Figure II-1b**. Therefore, methods and theoretical models for woven fabric composites [41] have been applied also for NCF composites. For woven composites Ishikawa and Chou [17,18] proposed the mosaic and fibre undulation models. In these models, an assumed representative volume element (RVE) is divided into infinitesimal strips and the classical laminate theory (CLT) is used to calculate elastic properties of the strip. The mosaic model disregards the waviness of the bundle whereas the fibre undulation model also includes the waviness. In [42], the 3D RVE consists of flat matrix

pockets as well as in-plane and interlaced bundle regions. The iso-strain assumption was used in the in-plane directions and constant stress assumption in the out-of-plane direction.

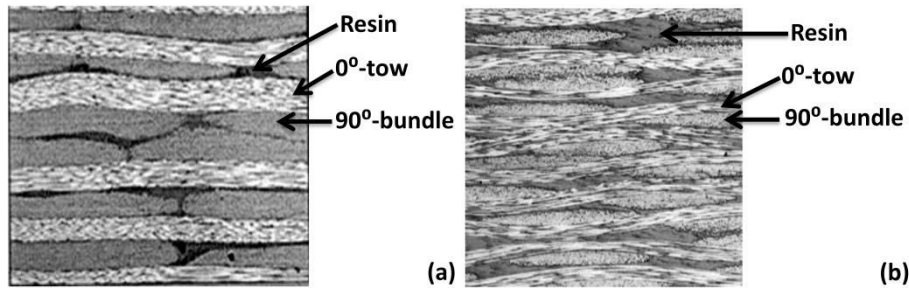


Figure II-1. Edge view of the mesostructure: **(a)** NCF composite **(b)** Woven composite

Similar analytical models have been applied to NCF composites in [43, 44]. In [45] the stitching thread was included in the analysis. Stiffness expressions for NCF composites assembled by a warp knitting procedure were presented in [46] using the manufacturing parameters as input. In [47] the reduced volume fraction of the bundle and matrix due to the distortion created by the stitching yarn was analysed. The reduced volume fraction was then used together with CLT to predict the mechanical properties of the laminate. Super-elements containing all details of the NCF architecture that necessarily requires numerical methods were introduced in [21]. More complex semi-analytical approaches are presented in [20, 24].

A different approach is using the assumption that the NCF composite stiffness problem can be reduced to CLT problem for laminate with “effective” elastic properties of “effective flat” layers. The effective stiffness is calculated considering an isolated curved beam (bundle, layer), replacing its interaction with the rest of the composite with proper boundary conditions. In [23] the effective modulus was calculated using a

Timoshenko model for curved beams with different boundary conditions during axial loading: “free beam” (no restrictions on z-displacement); “simple support” (zero z-displacement in support points); “elastic foundation” represented by one spring leading to very similar result as in case with “simple support”. The reduction of the effective bundle modulus was described by a knock-down factor.

Since the results were very sensitive with respect to the boundary conditions, we conclude that definition of surface conditions applied to curved tows to obtain effective stiffness representative for its behaviour in the NCF composite remains an unresolved problem.

The main objective of the work presented in this chapter is to develop and validate CLT based methodology for axial stiffness calculation of imperfect biaxial NCF composites with fibre tow waviness using layers effective properties of idealized straight laminate (Figure II-2) calculated using 2-dimensional FE modelling.

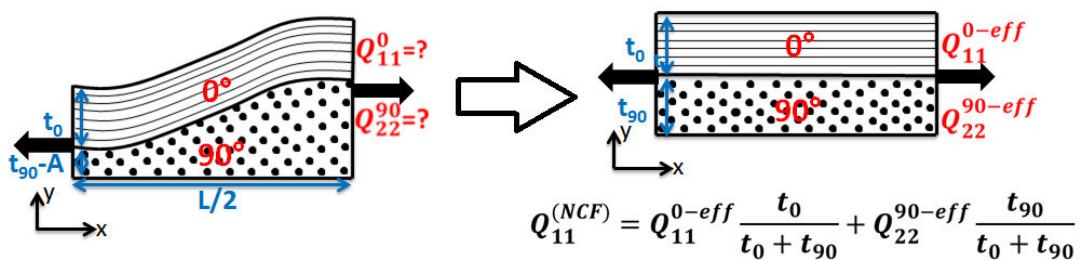


Figure II-2. NCF waved structure replaced by flat layers using effective stiffness while

A is the amplitude and L is the wavelength.

Different approaches are presented in this thesis: Isolated beam with appropriate boundary condition and Master curve approach.

It has to be noted that the observed trends and obtained results in all the following may be of relevance not only for NCF composites with bundle waviness, but also for woven composites.

2. FE modelling procedure (Material, geometry and assumptions)

In the previous study, [23], a two blanket cross-ply NCF's 0° -tow waviness was assumed sinusoidal and two possible geometrical configurations were analysed numerically: the in-phase case, when the waves of the two outer 0° -layers are in phase, and the out-of-phase case, when the waves of the outer 0° -layers are out of phase. Those are the extreme cases and in a real composite the RVE is often much larger than the wave length of the individual bundle in one blanket because the blankets of the fabric are randomly shifted in horizontal directions.

In this study, we analyse the stiffness of a simple $0/90$ unit of the NCF composite. The rest of the composite is roughly replaced with symmetry conditions. Two units are analysed, a unit with a surface 0° -layer, see **Figure II-3a** and **II-3b**, and another with an embedded 0° -layer, see **Figure II-3c**. The units correspond to a particular case of cross-ply NCF composite with zero shifts between blankets.

Bundles in the NCF composite are considered as unidirectional (UD) composites with certain fibre volume fraction and their elastic properties may be calculated using hexagonal unit cell as it was explained in [30] or simple rule of mixture based on iso-strain assumption, Halpin-Tsai expressions etc.

Bundles or layers with out-of-plane waviness are referred to in following as “curved bundles” or “curved layers”. First we assume that the structure of curved bundles in a layer may be replaced by homogenized layer with average fibre volume content, which is kept 0.6. In the bundle case the fibre volume fraction was 0.7. The elastic constants of the layers and the constituents are given in **Table II-1** for glass fibre- and carbon fibre- epoxy composites (GF/EP and CF/EP1). CF/EP2 composite properties were not calculated, they are assumed the same as for CF/EP1 except the longitudinal modulus which is lower (120GPa).

In calculations where the 90°-layer meso-structure with bundles, **Figure II-3a**, was modelled, the shape of the 90°-bundle in **Figure II-3a** was changed in order to keep the same fibre volume fraction $V_f = 0.6$ in the 90°-layer for models with different wave amplitudes and/or wave length.

Table II-1 Elastic constants of constituents and homogenized layers

Constituents	E1 (GPa)	E2 (GPa)	v12	v23	G12 (GPa)	G23 (GPa)
Glass fiber	76.00	76.00	0.20	0.20	31.67	31.67
Carbon fiber	233.00	23.00	0.20	0.20	20.00	9.60
Epoxy resin	3.00	3.00	0.38	0.38	1.09	1.09
Composites	E1 (GPa)	E2 (GPa)	v12	v23	G12 (GPa)	G23 (GPa)
Carbon fiber/Epoxy (CF/EP1)	141.00	8.80	0.26	0.44	3.60	3.10
Glass fiber/Epoxy (GF/EP)	46.80	11.30	0.26	0.45	3.80	4.00
Carbon fiber/Epoxy (CF/EP2)	The same properties as CF/EP1 with lower modulus E1=120 GPa					

The error introduced by replacing the layer with bundles by homogenized layer has been analysed before, for example, in [24] showing that the axial stiffness of a flat 0°-layer does not change significantly if the bundle mesostructure of the 0°-layer is replaced by homogenized layer with elastic properties corresponding to the average volume fraction of fibres in the layer. This result justifies the use of a curved 0°-layer instead of curved 0°-bundles in NCF composite stiffness investigation. The same study

demonstrated that the 90° -layer meso-scale details on the NCF laminate stiffness can be neglected in cross-ply NCF with straight 0° -bundles and constant 90° -layer thickness. The validity of the assumption, that, in NCF composite with curved 0° -layer, the 90° -layer bundle structure can be homogenized (“smeared out”), was checked in the current work comparing axial stiffness of models in **Figure II-3a** and **Figure II-3b** with sinusoidal shape of the waviness.

In calculations both models had the same fibre content. Changing the amplitude A of the waviness the average thickness of the 90° -layer was not changed. The results showed that the stiffness is just marginally affected by the mesostructure of the bundles and the 90° -layer homogenization is justified.

In the next step the CLT approach to NCF composite stiffness calculation is adapted, replacing the curved layer with a straight layer which has the “effective” in-plane stiffness of the curved layer. Thus, the laminate is made of “effective” layers.

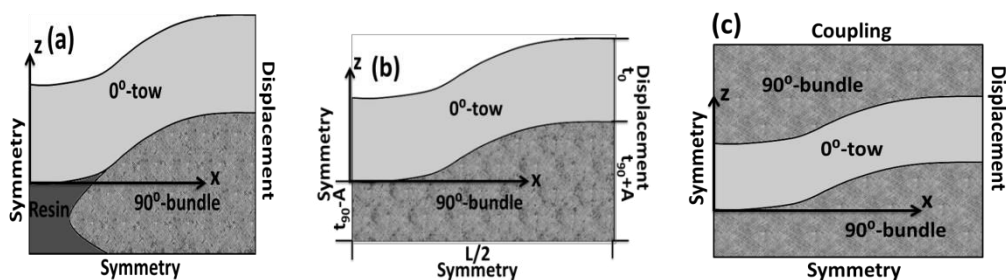


Figure II-3. NCF composites units **(a)** surface 0° -layer with bundle structure **(b)** surface 0° -layer with homogenized 90° -layer **(c)** embedded 0° -layer with homogenized 90° -layers.

The thickness of the 0° -layer is equal to the average thickness of one 90° -layer, $t_0 = t_{90}$. The top surface of the 0° -layer in **Figure II-3b** is traction free and all nodes

belonging to the top surface of the unit in **Figure II-3c** are coupled. The finite element code ANSYS14.0 with PLANE42 elements in plane strain assumption was used. The coordinate system of each element in the 0° -layer follows the sinusoidal shape of the layer. The area of each layer was meshed with quadratic elements with 200 divisions along the model length and 40 divisions along the thickness direction. Symmetry condition was applied along the left vertical boundary and a constant x-displacement was applied along the right vertical boundary leading to average strain in x-direction equal to 1%. Symmetry condition was applied along the bottom boundary.

Forces, for effective stiffness determination, were calculated by summing the reaction forces acting on the nodes along the corresponding edge of the layer. The reaction force on the node shared by both layers is replaced by half of the reaction force of the neighbouring node, by analogy with the reaction force on the upper-right node in the free upper boundary which is also equal to half of the reaction force of its neighbouring node.

3. Effective stiffness determination using isolated beam subjected to appropriate boundary conditions

In this approach the curved tows/layers are replaced by straight ones with effective elastic properties. Isolated curved layers with appropriate boundaries and end conditions are suggested for effective properties determination. To identify what type of surface loads on the isolated curved 0° -layer will represent its behaviour in the NCF composite, FE-analysis of the stress/traction distributions at the 0° -layer/ 90° -layer

interface in the NCF composite are conducted and sinus shaped functions are introduced to represent the surface load distribution. This approximation is then used in further numerical modelling to calculate the effective modulus of the curved 0° -layer. It is demonstrated that a CLT based analytical model, in which the nominal/average thickness of the 90° -layer, the effective stiffness of the curved 0° -layer and the effective stiffness of the 90° -layer with varying thickness are used, renders good accuracy.

The CLT approach for calculating the axial stiffness of the NCF composites is very attractive due to its simplicity in application. For a symmetric and balanced laminate the macroscopic in-plane stress-strain relationship is

$$\sigma_1^{(av)} = Q_{11}^{(LAM)} \varepsilon_1 + Q_{12}^{(LAM)} \varepsilon_2 \quad (\text{II-1})$$

In **(II-1)** direction 1 is the axial (loading) direction. Focusing on the laminate axial stiffness element $Q_{11}^{(LAM)}$ we will perform FE numerical analysis for plane strain case ($\varepsilon_2 = 0$). In this loading case $Q_{11}^{(LAM)}$ is obtained directly dividing the calculated axial average stress by the macroscopic strain applied. The average stress is axial force F_1 divided by nominal (average) thickness of the laminate h . Hence

$$Q_{11}^{(LAM)} = \frac{F_1}{h\varepsilon_1} \quad (\text{II-2})$$

The laminate stiffness elements are related to the A -matrix of the laminate

$$Q_{ij}^{(LAM)} = A_{ij}/h \quad A_{ij} = \sum_{k=1}^N \bar{Q}_{ij}^k t_k \quad (\text{II-3})$$

With \overline{Q}_{ij}^k and t_k being the effective stiffness matrix of the layer in global coordinates and average layer thickness respectively. Using the CLT approach with effective layers in a cross-ply NCF composite we obtain

$$Q_{11}^{(LAM)} = Q_{11}^{0-eff} \frac{t_0}{h} + Q_{22}^{90-eff} \frac{t_{90}}{h} \quad (\text{II-4})$$

Q_{22}^{90-eff} is the effective transverse stiffness of the homogenized 90° -layer with varying thickness (t_{90} is the average thickness), Q_{11}^{0-eff} is the effective axial stiffness of the curved 0° -layer.

The problem now lies in the correct definition and determination of the effective stiffness. Two types of models were analysed.

- a) Individual curved 0° -layer , see **Figure II-4**
- b) NCF composite shown in **Figure II-3a** and waved laminate **Figure II-3b**

The boundary conditions are presented in **Figure II-3** and **Figure II-4**. For all models, symmetry condition is applied along the left vertical boundary and an x-displacement is applied along the right vertical boundary. The average strain in x-direction introduced by the applied displacement is equal to 1%. An additional symmetry condition was applied to the waved laminate along the bottom boundary which is the mid-plane of $[0, 90]_s$ NCF composite or the interface with the rest of the composite in a more general case.

An isolated sinusoidal 0° -layer with constant thickness subjected to load in x-direction at ends and different combinations of loads on curved surfaces was also analysed using FE (only half of the wavelength was considered). The boundary conditions used

analysing isolated curved 0° -layers are shown in **Figure II-4**. In addition, for the “free end” 0° -layer, the displacement in the z-direction for the middle node of the left vertical boundary was set to zero. For the curved 0° -layer with “fixed ends” the same displacement was zeroed for the first and the last nodes along the bottom edge. For the curved 0° -layer on “rigid foundation”, this displacement is zero for all nodes belonging to the bottom boundary. Finally, for the model in **Figure II-4d**, the load was distributed along the bottom surface of the curved 0° -layer following a sinus shape function.

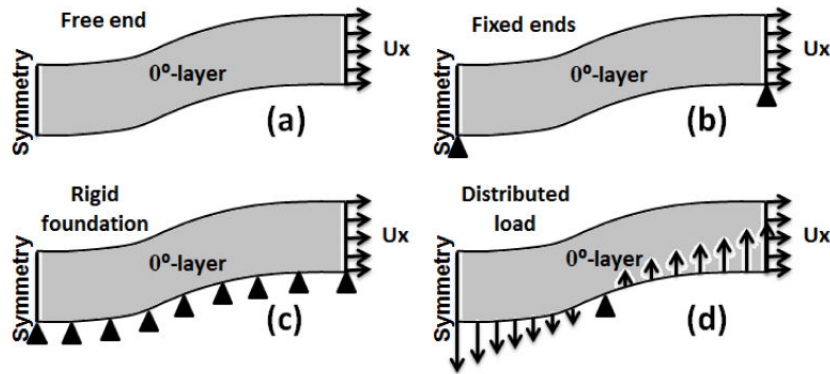


Figure II-4. Curved layer subjected to different boundary conditions

3.1. Meso-scale homogenization

First, we will inspect the validity of the assumption that the bundle structure in the curved 90° -layer can be replaced by a homogenized curved layer, in other words, we will compare the axial stiffness of models in **Figure II-3a** and **Figure II-3b**. In a similar investigation Mattson et al. [24] demonstrated that the mesoscale details on the NCF laminate stiffness can be neglected for the case with straight 0° -bundles, we would like to check it for laminates with curved layers.

In calculations both models (**Figure II-3a** and **Figure II-3b**) have the same fibre content 0.6 in the 90° -layer and $t_0 = t_{90} = 0.3mm$. The change in the amplitude A of

the waviness does not change the average thickness of the 90°-layer. It is equal to the thickness when there is no waviness. The z-coordinates of the points which belong to the interface are related to the x-coordinate as follows:

$$z = A \sin\left(\frac{2\pi}{L}\left(x - \frac{L}{4}\right)\right) = -A \left(\cos\left(\frac{2\pi x}{L}\right)\right) \quad (\text{II-5})$$

The results in **Figure II-5** for different combinations of amplitudes and wavelengths show that the stiffness is just marginally affected by the mesostructure of the bundles and the 90°-layer homogenization is justified. In the following only the model in **Figure II-3b** is analysed.

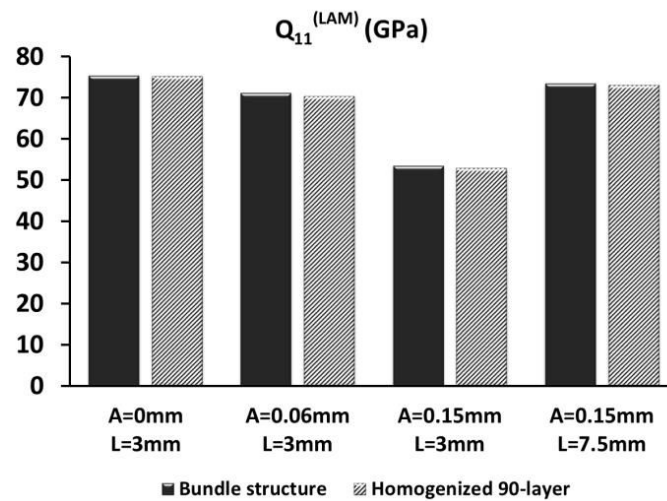


Figure II-5. Axial stiffness comparison between NCF composite with 90°-layers bundles and composite with homogenized 90°-layer.

3.2. Effect of wavelength and amplitude on laminate stiffness

Results for CF/EP1 laminate with elastic properties in **Table 1** are shown in **Figure II-6**. Parameters A , t_0 , L are defined in **Figure II-3b**. In this figure t_0 is the thickness of the

curved 0° -layer, t_{90} is the average thickness of the homogenized 90° -layer, $h = t_0 + t_{90}$. It is clear that $Q_{11}^{(LAM)}$ is significantly reduced with increasing amplitude and decreasing wavelength of the waviness.

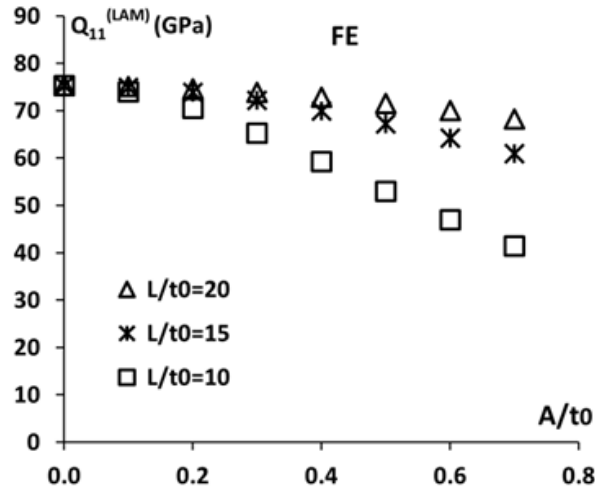


Figure II-6. Effect of the waviness on the CF/EP1 NCF composite axial stiffness ($t_0 = t_{90}^{(av)}$): Using the FE-model in **Figure II-3b**

One can see very large reduction of $Q_{11}^{(LAM)}$ with increasing amplitude and decreasing wavelength of the waviness.

3.3. Predictions based on isolated curved layers with boundary conditions used in previous studies

The three curves in **Figure II-7** showing the laminate stiffness were obtained using **(II-4)**. The effective stiffness of the 0° -layer Q_{11}^{0-eff} was calculated for isolated curved layer shown in **Figure II-4** using FE with boundary conditions **(a)**, **(b)** and **(c)**. The 90° -layer effective stiffness was assumed equal to the 90° -layer material transverse stiffness using data in **Table II-1**. These curves may be compared with direct FE results

(symbols in **Figure II-7**) taken from **Figure II-6**. The comparison demonstrates the failure of these boundary conditions used to give values of 0° -layer effective stiffness relevant for using in **(II-4)**.

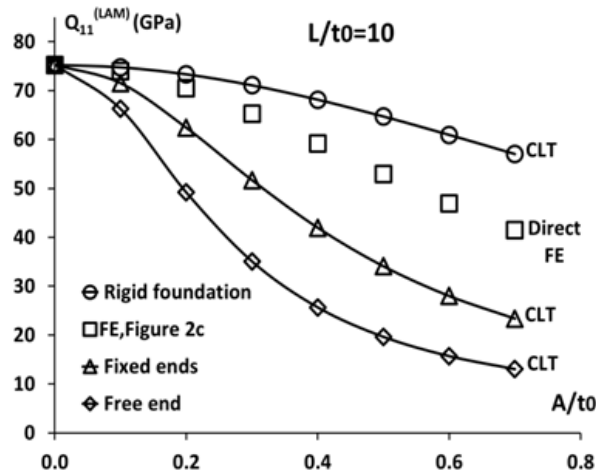


Figure II-7. Effect of the waviness on the CF/EP1 NCF composite axial stiffness ($t_0 = t_{90}^{(av)}$): CLT with effective stiffness of the curved layer according to different boundary conditions

3.4. The layers effective stiffness dependence on A/t_0 and L/t_0

The effective in-plane axial stiffness of the curved layer is lower than the stiffness of a straight layer mainly because the fibres are not oriented in-plane. However, as shown in **[23]**, the effective stiffness strongly depends also on the interaction with the adjacent material (tows of different orientations, resin).

Calculating $Q_{11}^{(LAM)}$ according to **(II-2)** we use the total force F_1 which due to force balance is the same in any cross-section. For example, in **Figure II-3b** $F_1^R = F_1(x = L/2)$ is equal to $F_1^L = F_1(x = 0)$. In other words, using **(II-2)** and FE it is not

important in which cross-section the reaction force is obtained before dividing it with the average composite thickness h .

If instead the CLT based **(II-4)** is used, the effective layer stiffness has to be found first. Similarly as was done for the whole laminate stiffness case, we would for this purpose divide the calculated force acting on some arbitrary cross-section of the layer by its cross-section area and then by the applied strain. However, the force on a cross-section of a layer depends on which cross-section we consider. For example

$$F_1^R(0^\circ) \neq F_1^L(0^\circ) \quad F_1^R(90^\circ) \neq F_1^L(90^\circ) \quad F_1^R(0^\circ) + F_1^R(90^\circ) = F_1 \quad \text{(II-6)}$$

The numbers 0° and 90° in parenthesis indicate the layer under consideration. Because of **Equation (6)** effective layer stiffness calculated on the left and the right edge of the model differ

$$Q_{11}^R(0^\circ) \neq Q_{11}^L(0^\circ) \quad Q_{22}^R(90^\circ) \neq Q_{22}^L(90^\circ) \quad \text{(II-7)}$$

where

$$Q_{11}^R(0^\circ) = \frac{F_1^R(0^\circ)}{\varepsilon_1 t_0}, \quad Q_{11}^L(0^\circ) = \frac{F_1^L(0^\circ)}{\varepsilon_1 t_0}, \quad Q_{22}^R(90^\circ) = \frac{F_1^R(90^\circ)}{\varepsilon_1 t_{90}}, \quad Q_{22}^L(90^\circ) = \frac{F_1^L(90^\circ)}{\varepsilon_1 t_{90}} \quad \text{(II-8)}$$

Due to interaction, layers are not subjected to uniaxial loading and strictly speaking the calculated numbers are not stiffness matrix elements. This explains the two different values. The situation will be similar analysing isolated curved layers with traction boundary conditions. Therefore, it has to be clarified which layer stiffness Q_{11}^{0-eff} and Q_{22}^{90-eff} to be used in the CLT **(II-4)**.

For this purpose we may formally write that the force is distributed between 0° -layer and 90° -layer according to:

$$F_1^R = F_1^R(0^\circ) + F_1^R(90^\circ) \quad (\text{II-9})$$

$$F_1^L = F_1^L(0^\circ) + F_1^L(90^\circ) \quad (\text{II-10})$$

And

$$F_1^R = F_1^L = F_1 \quad (\text{II-11})$$

Averaging gives:

$$F_1 = \frac{F_1^R + F_1^L}{2} = \frac{F_1^R(90^\circ) + F_1^L(90^\circ)}{2} + \frac{F_1^R(0^\circ) + F_1^L(0^\circ)}{2} \quad (\text{II-12})$$

Substituting **(II-12)** in **(II-2)** and using **(II-8)**:

$$Q_{11}^{(LAM)} = \frac{Q_{22}^R(90) \frac{t_{90+A}}{t_{90}} + Q_{22}^L(90) \frac{t_{90-A}}{t_{90}}}{2} \frac{t_{90}}{h} + \frac{Q_{11}^R(0^\circ) + Q_{11}^L(0^\circ)}{2} \frac{t_0}{h} \quad (\text{II-13})$$

Comparing **(II-13)** with the CLT expression in **(II-4)** the correct expressions for effective stiffness of layers considering them as “isolated” is given by:

$$Q_{11}^{0-eff} = \frac{Q_{11}^R(0^\circ) + Q_{11}^L(0^\circ)}{2} \quad (\text{II-14})$$

$$Q_{22}^{90-eff} = \frac{Q_{22}^R(90) \frac{t_{90+A}}{t_{90}} + Q_{22}^L(90) \frac{t_{90-A}}{t_{90}}}{2} \quad (\text{II-15})$$

Forces for using in **(II-8)** were calculated from the model in **Figure II-3b** by summing the reaction forces acting on the nodes along the corresponding edge of the layer. The reaction force on the node shared by both layers is replaced by half of the reaction force of the neighbouring node, by analogy with the reaction force on the upper-right node in the free upper boundary, which is also equal to half of the reaction force of its neighbouring node. **Figure II-8** shows how the effective stiffness of the 0° -layer, Q_{11}^{0-eff} and the effective stiffness of the 90° -layer Q_{22}^{90-eff} decrease due to the

waviness described by A/t_0 for several values of L/t_0 . The difference between $Q_{11}^R(0^\circ)$ and $Q_{11}^L(0^\circ)$ calculated on both edges is rather small. In contrast the transverse effective stiffness parameters of the 90° -layer, $Q_{22}^R(90)$ and $Q_{22}^L(90)$ have very different trends: one (calculated at $x = 0$) is increasing, the other one is decreasing. The combined effective stiffness Q_{22}^{90-eff} calculated according to (II-15) decreases from about 9 GPa to 7 GPa.

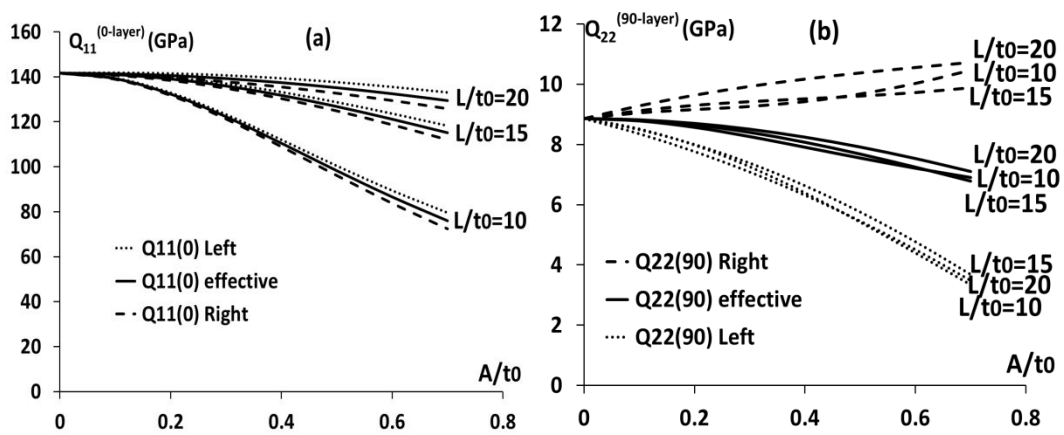


Figure II-8. Axial stiffness for (a) the 0° -layer and (b) the 90° -layer, CF/EP1 composite

We can introduce knock down factors for the laminate and the layers by dividing the effective stiffness with the stiffness corresponding to a reference case having straight tows ($A=0$). **Figure II-9** shows for CF/EP1 that for $L/t_0=10$ the decrease in composite stiffness is nearly the same as for the 0° -layer effective stiffness.

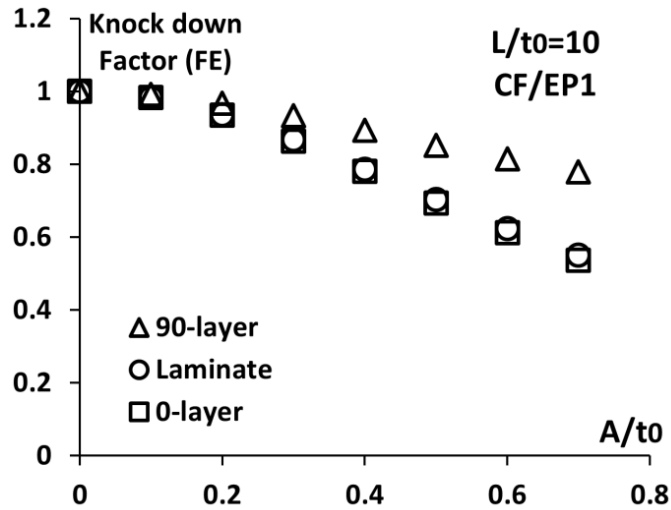


Figure II-9. Comparison between knock down factor of the 0^o-layer, the 90^o-layer and the laminate

Apparently the laminate stiffness reduction is dominated by the reduction of the 0^o-layer stiffness due to waviness. A simplified form of the laminate stiffness expression, **(II-4)**, in which the 90^o-layer effective stiffness is assumed equal to the 90^o-layer material stiffness may be therefore be motivated:

$$Q_{22}^{90-eff} = Q_{22}^{90} \tag{II-16}$$

The accuracy of the simplification in **(II-16)** will be verified in following calculations.

3.5. Approximation of tractions at the 0/90-layer interface

In line with the objectives of this study, the task is to find the effective stiffness of the curved 0^o-layer analysing an isolated curved layer subjected to relevant boundary conditions. These include not only end loads applied to the layer, but also surface loading shown as “distributed load” in **Figure II-4d**. Only in the presence of “distributed load” forces $F_1^R(0^\circ)$ and $F_1^L(0^\circ)$ may differ.

Knowledge regarding the distributed load is conveniently obtained by analysing stresses at the 0°- and the 90°-layer interface using FE. The results and the observed trends used to define shape functions for the interface stresses from fitting a limited number of FE-calculations are presented in this section. The methodology suggested for finding coefficients in these shape functions is described in more detail in **Appendix**. These functions can then be used for curved 0°-layer stiffness analysis with an arbitrary amplitude or wavelength.

Local stress distribution at the 0/90-layers interface has been analysed: The normal stress σ_n and the shear stress σ_{nt} were determined in each node along a path on the interface. In the FE-analysis those stress components are slightly different on both sides of the interface. The value along the path on the interface which is given by the code is the average of the stresses calculated for the closest element to the interface in the 0°-layer and in the 90°-layer. In **Figure II-10**, the normal stress σ_n is plotted as a function of the normalized distance along the x-axis for different A/t_0 and L/t_0 . The curves show large variation of the normal stress along the interface. This stress is equal to zero when there is no waviness. The waviness contributes to the appearance of tensile normal stress in the left part and compressive normal stress in the right part on the interface. The maximum value of the tensile and the compressive normal stress is increasing with decreasing L/t_0 and with increasing A/t_0 . For simplicity, this behaviour was fitted with a sinusoidal function, **(II-17)**, with amplitude depending on the waviness parameters and the elastic properties of the material.

$$\sigma_n = \sigma_{n0} \sin\left(\frac{2\pi}{L}\left(x - \frac{L}{4}\right)\right) = -\sigma_{n0} \left(\cos\left(\frac{2\pi x}{L}\right)\right) \text{ With } \sigma_{n0} = f\left(\frac{A}{t_0}, \frac{L}{t_0}, E_1, \text{etc}\right) \text{ (II-17)}$$

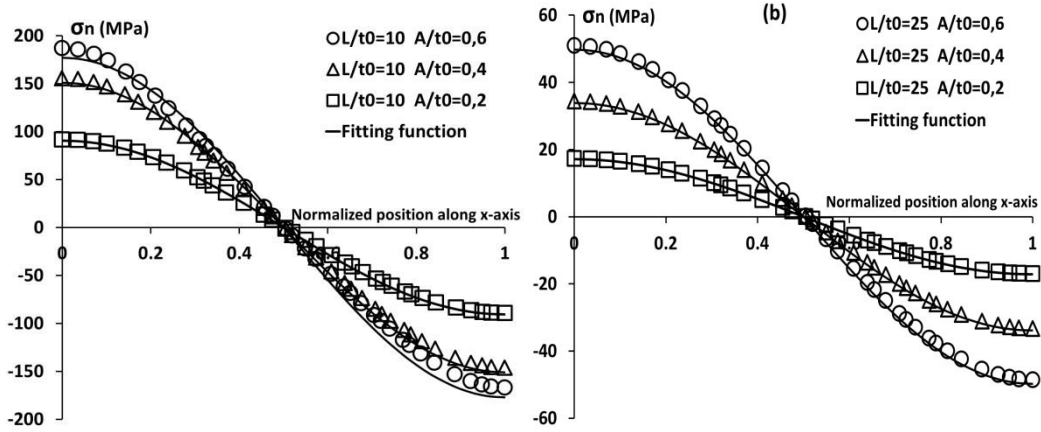


Figure II-10. Normal stresses at layer interface in CF/EP1 composite and fitting (a) for $L/t_0=10$; (b) for $L/t_0=25$, applied strain 1%.

In **Figure II-11**, the shear stress σ_{nt} on the interface is plotted as a function of the normalized position along the x-axis for different A/t_0 and L/t_0 . In a straight layer cross-ply laminate this stress component would be equal to zero. However, the rather complex σ_{nt} behavior becomes significant with increasing 0° -layer amplitude. Calculations on isolated curved layers showed that the significance of the applied shear stress on the boundary is small (most important is the normal stress σ_n), justifying the use of the same rough sinus function approximation to fit the shear stress in the whole parameter region

$$\sigma_{nt} = \sigma_{nt0} \sin\left(\frac{2\pi}{L}\left(x - \frac{L}{4}\right)\right) = -\sigma_{nt0} \left(\cos\left(\frac{2\pi x}{L}\right)\right) \quad (\text{II-18})$$

$$\text{With } \sigma_{nt0} = f\left(\frac{A}{t_0}, \frac{L}{t_0}, E_1, \text{etc}\right)$$

As one can see in **Figure II-11a** the fitting is obviously not good for *small* L/t_0 and sufficient for *larger* L/t_0 (**Figure II-11b**).

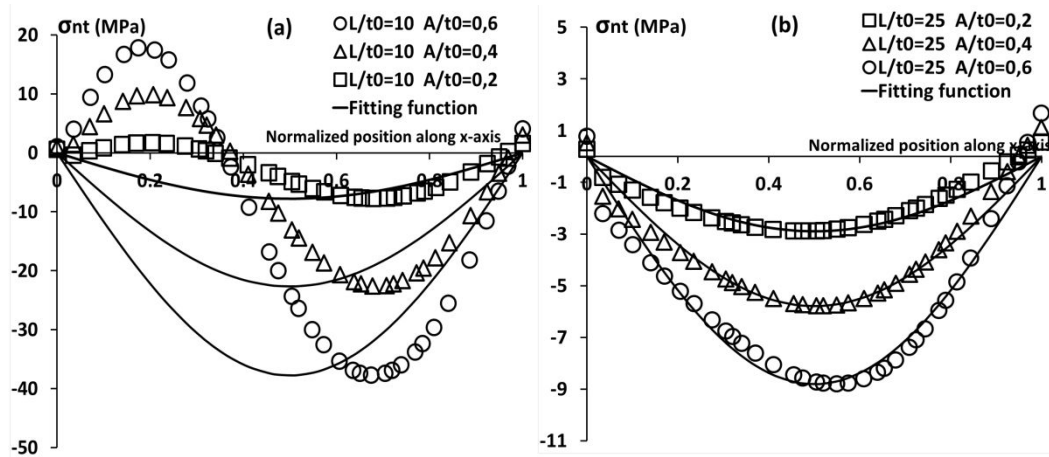


Figure II-11. Shear stresses at layer interface in CF/EP1 composite and fitting **(a)** for $L/t_0=10$; **(b)** for $L/t_0=25$, applied strain 1%.

Thus, performing FE-calculations for a limited number of L/t_0 and A/t_0 cases we can find approximate interface stress expressions for a given material to be used for any practical combination of these geometrical parameters.

The main objective of this part was to find simple expressions for further analytical application. The expressions for σ_{n0} and σ_{nt0} dependence on L/t_0 and A/t_0 are given in **Appendix**.

3.6. Composite stiffness based on effective stiffness of an isolated 0^0 -layer with surface loads

In this subsection we use the calculated and approximated normal and shear stress distributions along the layer interface as surface loads in an isolated curved 0^0 -layer model shown in **Figure II-12**. The approximate expressions for the normal and the shear stresses given in **Appendix** are used. The surface load is obtained by multiplying the stress components by the element length which is assumed equal to the distance

dx between two neighbouring nodes. The calculated load is applied in the local coordinate system related to each element on the bottom surface of the curved layer. This new boundary condition is introduced in addition to the symmetry on the left edge and the displacement applied in the right edge. Since the loading applied to the 0°-layer is not uniaxial the Q_{11}^{0-eff} calculated using (II-14) is, strictly speaking, not the axial stiffness. Nevertheless, it represents the curved 0°-layer mechanical behaviour in the composite.

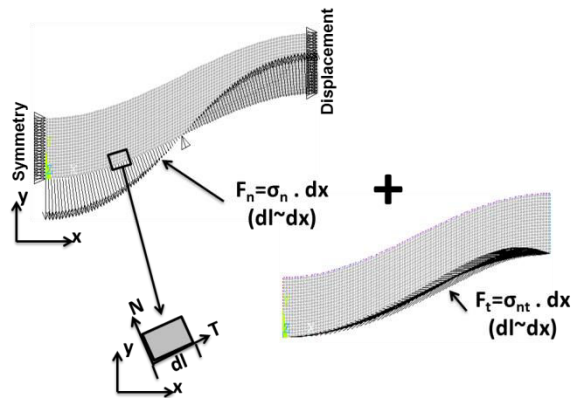


Figure II-12. Application of distributed load on the 0°-layer surface

In **Figure II-13**, where the calculated effective stiffness of an isolated 0°-layer is presented together with the effective stiffness of the 0°-layer determined from the waved cross ply laminate, see **Section 2.4 “The layers effective stiffness dependence on A/t_0 and L/t_0 ”**, good agreement between both solutions is demonstrated. For the sake of comparison, effective 0°-layer stiffness calculated using the rest of boundary conditions in **Figure II-4** is also presented. Effective stiffness in the case of fixed/free ends is unrealistically low, while rigid foundation is too high. The most accurate results are given by the beam with distributed surface load. Thus, the assumption of replacing the interaction between the 0° and the 90°-layers in the laminate by a distributed load

applied to the curved beam is validated. The accuracy can be improved by more accurate fitting of the interface stresses; the simplicity can be improved by more rough approximation that, probably, would not affect the calculated stiffness too much.

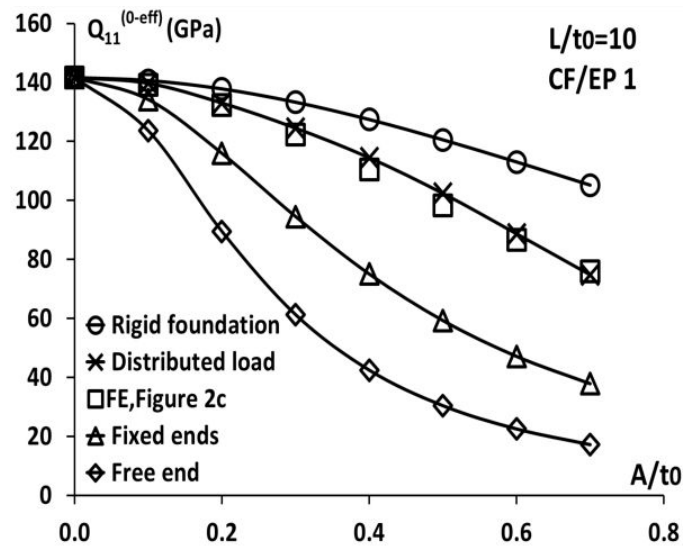


Figure II-13. Effective stiffness of the 0°-layer with different boundary conditions

Finally, CLT, see (II-4), is used to determine the laminate stiffness utilizing the effective stiffness of the curved 0°-layer with distributed load, and the effective stiffness of the 90°-layer. Effective 90°-layer stiffness is used in two approximations: a) With varying thickness with values from **Figure II-8b** (this requires FE calculations of the cross-ply composite); b) using (II-16), i.e. $Q_{22}^{90-eff} = Q_{22}^{90}$ (which is not accurate, but simple for use). In **Figure II-14** to **Figure II-16** the laminate stiffness is presented as a function of A/t_0 for different L/t_0 . In **Figure II-14a**, **II-15a** and **II-16a** the effective stiffness of the 90°-layer is used whereas in **Figures II-14b**, **II-15b** and **II-16b** the 90°-layer with varying thickness is represented by its transverse stiffness Q_{22}^{90} calculated using data in **Table II-1**. These results show good agreement between the analytical CLT approach with the effective stiffness of the 0°-layer and FE calculation of the laminate stiffness.

Very small differences in results are seen when the 90°-layer effective stiffness is represented by its material transverse stiffness, proving that this approximation may be used.

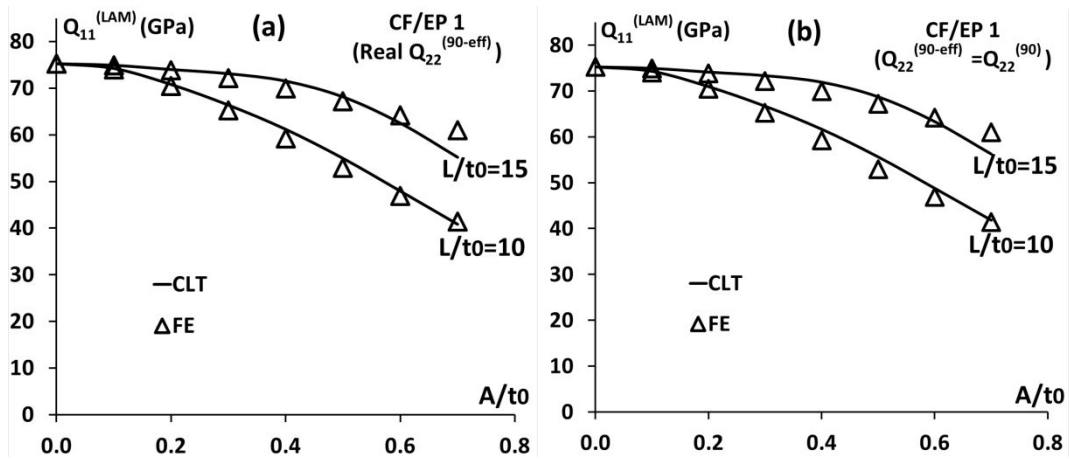


Figure II-14. CLT using effective stiffness compared to FE-analysis for CF/EP1

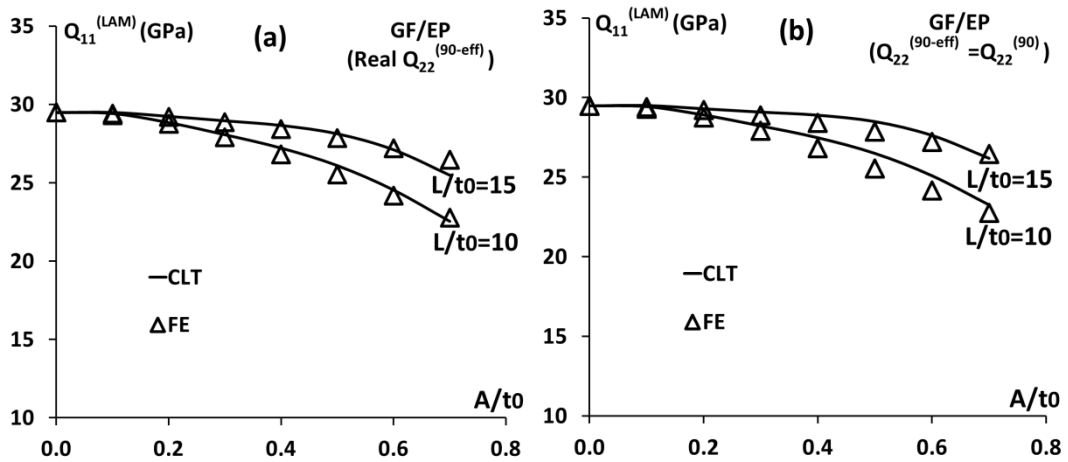


Figure II-15. CLT using effective stiffness compared to FE-analysis for GF/EP

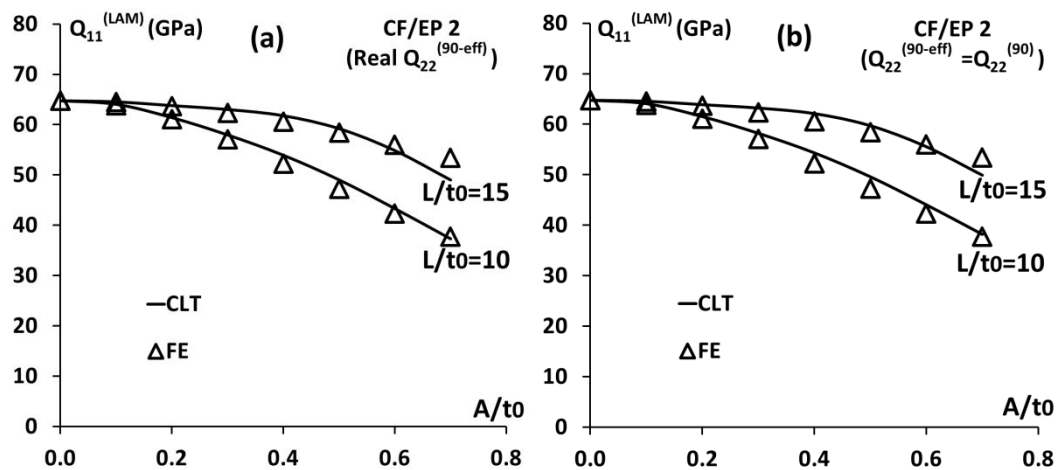


Figure II-16. CLT using effective stiffness compared to FE-analysis for CF/EP2

4. Effective stiffness determination using master curve approach

In this section, it will be demonstrated that the axial stiffness of a biaxial cross-ply NCF composite described by knock-down factor is similar to the knock-down factor for the curved layer stiffness obtained in the same FE calculation. Then a novel “master curve approach” is presented which allows calculating the knock down factor of a curved layer of arbitrary wave amplitude and length. The master curve for the given NCF composite material is obtained fitting FE knock-down factor values for one (preferably relatively short) wavelength and at least two values of amplitude. Only one additional FE calculation is required to cover all possible amplitude cases for a different wavelength. The curved layer knock-down factor is used to calculate the NCF composite knock-down factor. The very high accuracy of this approach is demonstrated in comparison with direct FE calculations.

The CLT approach for calculating the axial stiffness of the NCF composite specimen is the same as in calculations for the laminate with straight layers. The stiffness elements

of a laminate with flat layers (NCF composite with zero waviness) are related to the A-matrix of the laminate

$$Q_{ij}^{LAM} = A_{ij}^{LAM} / h \quad A_{ij}^{LAM} = \sum_{k=1}^N \bar{Q}_{ij}^k t_k \quad (\text{II-19})$$

For the NCF composite represented by laminate with effective layers we have

$$Q_{ij}^{NCF} = A_{ij}^{NCF} / h \quad A_{ij}^{NCF} = \sum_{k=1}^N \bar{Q}_{ij}^{k-eff} t_k \quad (\text{II-20})$$

with \bar{Q}_{ij}^{k-eff} , t_k and h being the effective stiffness matrix of the layer in global coordinates, average layer thickness and average laminate thickness respectively. For the axial stiffness of a cross-ply laminate and the NCF composite analysed in this part the following relations are obtained:

$$Q_{11}^{LAM} = Q_{11}^0 \frac{t_0}{h} + Q_{22}^{90} \frac{t_{90}}{h} \quad (\text{II-21})$$

$$Q_{11}^{NCF} = Q_{11}^{0-eff} \frac{t_0}{h} + Q_{22}^{90-eff} \frac{t_{90}}{h} \quad (\text{II-22})$$

Where Q_{22}^{90-eff} is the effective transverse stiffness of the homogenized 90°-layer with varying thickness (t_{90} is the average thickness) and Q_{11}^{0-eff} is the effective axial stiffness of the curved 0°-layer.

In this section the index “LAM” indicates the NCF with straight layers (A=0), and the index “NCF” refers to NCF composites with waved layers.

The stiffness knock-down factors for the 0°-layer, for the 90°-layer and for the NCF composite (represented by laminate) are introduced as follows

$$k_0 = \frac{Q_{11}^{0-eff}}{Q_{11}^0} \quad k_{90} = \frac{Q_{22}^{90-eff}}{Q_{22}^{90}} \quad k_{NCF} = \frac{Q_{11}^{NCF}}{Q_{11}^{LAM}} \quad (\text{II-23})$$

Combining (II-22) and (II-23) gives

$$Q_{11}^{LAM} k_{NCF} = k_0 Q_{11}^0 \frac{t_0}{h} + k_{90} Q_{22}^{90} \frac{t_{90}}{h} \quad (\text{II-24})$$

Using (II-21) to replace Q_{11}^0 , (II-24) can be rearranged in the form

$$k_{NCF} = k_0 + \Delta k \quad \Delta k = (k_{90} - k_0) \frac{Q_{22}^{90} t_{90}}{Q_{11}^{LAM} h} \quad (\text{II-25})$$

The second term in (II-25) depends on the layer stiffness and thickness ratio and on the difference between the knock-down factors for the 0°- and 90°-layer. It will be shown further that this term can be neglected without introducing any noticeable error. Certainly, to find these knock-down factors, we have to start with proper definition and methodology for determination of the effective stiffness.

The axial stiffness Q_{11}^{NCF} of symmetric and balanced NCF composite can be obtained from the macroscopic in-plane stress-strain relationship

$$\sigma_x^{NCF} = Q_{11}^{NCF} \varepsilon_x + Q_{12}^{NCF} \varepsilon_y \quad (\text{II-26})$$

In (II-26) x-direction is the specimen axial (loading) direction, see **Figure II-3**. The NCF composite axial stiffness element Q_{11}^{NCF} is obtained performing FE-analysis for plane strain case ($\varepsilon_y = 0$). In this loading case Q_{11}^{NCF} is obtained directly dividing the calculated axial average stress by the macroscopic strain applied. The average stress is axial force F_x divided by nominal (average) thickness of the laminate h . Hence

$$Q_{11}^{NCF} = \frac{F_x}{h \varepsilon_x} \quad (\text{II-27})$$

The effective in-plane axial stiffness of the curved 0°-layer is lower than the stiffness of a straight layer mainly because the fibres are not oriented in-plane. However, as shown in [48] and described in details in the previous section, the curved layer in addition to end loading (applied displacement) is subjected to large normal and

tangential tractions at the layer interface. In other words the loading to the curved layer is not uniaxial and as a consequence the force calculated at the right end of the layer (index R) is not equal to the force on the left end (index L) , $F_x^R(0^\circ) \neq F_x^L(0^\circ)$. This makes the determination of the effective stiffness uncertain, because different values are obtained using different cross-sections. The same applies to the 90° -layer with varying thickness $F_x^R(90^\circ) \neq F_x^L(90^\circ)$. The numbers 0° and 90° in parenthesis indicate the layer under consideration. Certainly, on both ends the total force is the same, for example

$$F_x^R(0^\circ) + F_x^R(90^\circ) = F_x \quad \text{(II-28)}$$

Because of the described reason the effective layer “stiffness” calculated on the left and the right edge of the model differs

$$Q_{11}^R(0^\circ) \neq Q_{11}^L(0^\circ) \quad Q_{22}^R(90^\circ) \neq Q_{22}^L(90^\circ) \quad \text{(II-29)}$$

$$Q_{11}^R(0^\circ) = \frac{F_x^R(0^\circ)}{\varepsilon_x t_0} , Q_{11}^L(0^\circ) = \frac{F_x^L(0^\circ)}{\varepsilon_x t_0} , Q_{22}^R(90^\circ) = \frac{F_x^R(90^\circ)}{\varepsilon_x (t_{90}+A)} , Q_{22}^L(90^\circ) = \frac{F_x^L(90^\circ)}{\varepsilon_x (t_{90}-A)} \quad \text{(II-30)}$$

In fact none of these numbers is stiffness, because the loading to the layer is not uniaxial. For the purpose of employing the CLT, the effective layer stiffness Q_{11}^{0-eff} and Q_{22}^{90-eff} have to be defined in a way that using (II-20) gives exactly the same values for NCF composite as direct FE calculation.

In the previous section, it was demonstrated that the following definitions of effective stiffness give this result

$$Q_{11}^{0-eff} = \frac{Q_{11}^R(0^\circ) + Q_{11}^L(0^\circ)}{2} \quad \text{(II-31)}$$

$$Q_{22}^{90-eff} = \frac{Q_{22}^R(90)\frac{t_{90+A}}{t_{90}} + Q_{22}^L(90)\frac{t_{90-A}}{t_{90}}}{2} \quad (\text{II-32})$$

These definitions together with (II-23) will be used in all calculations in this section.

4.1. NCF stiffness knock-down factor

In order to investigate which term (k_0 or Δk) is affecting more the NCF knock down factor in (II-25), calculations are performed for two different ratios of wavelength L and the layer thickness t_0 : $L/t_0=10$ and $L/t_0=15$ and for both CF/EP and GF/EP materials for the unit with surface 0° -layer. Results are presented in Figure II-17. Although the knock down factors in the case of CF/EP are decreasing more than for the case of GF/EP, both figures present similar behaviour of the curves and the same conclusions can be deduced for both materials. The term Δk in (II-25) can be neglected since it is almost equal to zero in the figures. Thus, the NCF composite knock down factor defined by (II-23) can be assumed equal to the 0° -layer knock down factor defined by (II-23) and (II-31), $k_{NCF} \simeq k_0$. In other words, in order to know NCF cross-ply composite knock down factor, it is enough to know the 0° -layer knock down factor.

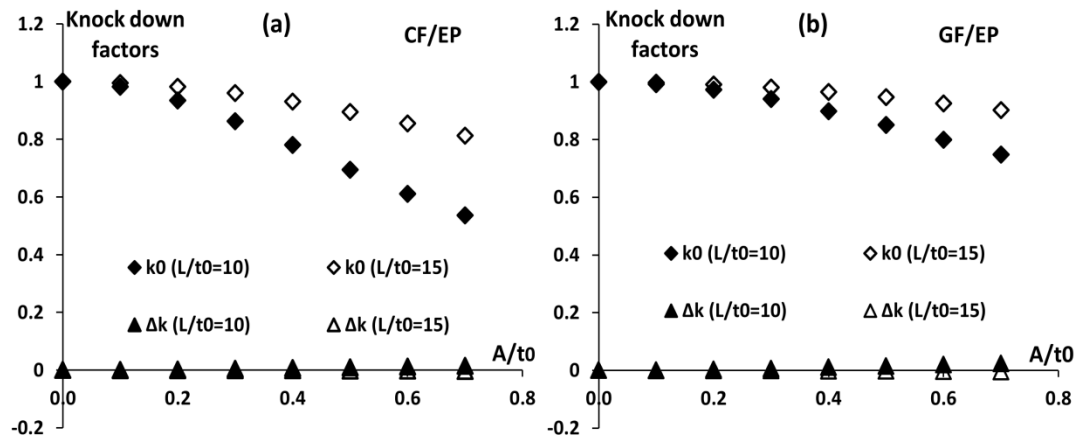


Figure II-17. Comparison of k_0 and Δk in the expression of NCF knock-down factor in **(II-25)** for unit with surface 0° -layer **(a)** CF/EP and **(b)** GF/EP

In the following, the focus will be mostly on the determination of knock down factor of the 0° -layer. An important observation deduced from **Figure II-17** is that the curves of k_0 corresponding to $L/t_0=10$ and $L/t_0=15$ look similar and have similar shape. This leads to assumption that both curves may coincide by performing proper “deformation” of both axis (changing scales). As a consequence the curve corresponding to $L/t_0=15$ could be obtained as a part of the curve corresponding to $L/t_0=10$. In the following discussion it will be shown that the knock-down factor for any L/t_0 ratio as a function of A/t_0 based on known relationship for one given L/t_0 ratio can be considered as a master curve. It is suggested to determine the master curve by performing accurate FE calculations for the case of short wavelength L/t_0 and to fit it with an analytical function.

4.2. Master curve approach

4.2.1. Knock-down factor curve and fitting function

The case of $L/t_0=6$ is considered as extreme case where the same amplitude can lead to a steep angle of the waviness. The 0° -layer knock-down factor is decreasing more than in cases with larger ratios. The knock-down factor dependence on the wave amplitude at $L/t_0=6$ will be considered as master curve for the rest of calculations. The analytical fitting of the case of $L/t_0=6$ will be used to calculate the knock-down factors for the other cases of the higher ratios of L/t_0 . The calculated values and the fitting curves are presented in **Figure II-18** for both materials and for the unit with surface 0° -layer. The same fitting expression in **(II-33)** is found for both materials.

$$k_0 = \frac{1}{1+b(A/t_0)^c}$$

(II-33)

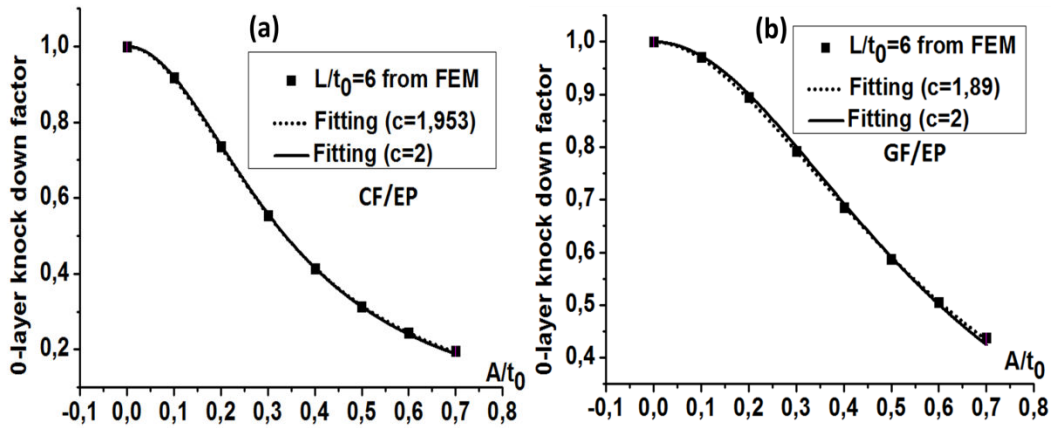


Figure II-18. Fitting function for Master curve ($L/t_0 = 6$) (surface 0^0 -layer) **(a)** CF/EP and **(b)** GF/EP

The fitting constants “ b ” and “ c ” are given in **Table II-2** for both CF/EP and GF/EP materials and for both surface and embedded 0^0 -layer cases.

Table II-2. Fitting constants

	Surface 0^0 -layer		Embedded 0^0 -layer	
	b	c	b	c
CF/EP	8.39	1.95	4.95	1.95
	8.78	2	5.14	2
GF/EP	2.56	1.89	1.51	1.86
	2.77	2	1.64	2

The fitting constant c is weakly dependent on the material system and in following it is considered as a material independent and set equal to 2. The new constant “ b ” is then found according to the new c ($c=2$) in order to get the best possible fitting. This means that only one parameter “ b ” depending on the material properties is remaining in the (II-33). Then, for instance, even one single FE calculation is enough to determine this parameter.

4.2.2. Validation and application of the master curve approach

In this section the aim is to demonstrate and identify the relationship between knock-down factor curves for different combinations of L/t_0 and A/t_0 . It will be explained how the master curve is used to predict the 0^o-layer knock down factor degradation for any case of L/t_0 .

The procedure, as illustrated in **Figure II-19**, is the following: We consider the knock-down factor curves for two different wavelength values L/t_0 . Assuming that one of them is the master curve (in our selection it is the curve for $L/t_0=6$, denoted k_{0M} (Index M is for Master) and the other one corresponds to a different wavelength $L/t_0=n$, denoted k_{0n} . An arbitrary value of the knock-down factor, k_0^* is selected on both curves and corresponding values of the amplitude are denoted $(A/t_0)_M^*$ and $(A/t_0)_n^*$. Therefore,

$$k_{0M}((A/t_0)_M^*) = k_0^* \quad k_{0n}((A/t_0)_n^*) = k_0^* \quad \text{(II-34)}$$

Using data in **Figure II-19** we may produce a new figure where on the horizontal axis:

$$a = \frac{(A/t_0)_M^*}{(A/t_0)_n^*} \cdot (A/t_0)_n \quad \text{(II-35)}$$

In **(II-35)** $(A/t_0)_n$ is the variable value of the amplitude for k_{0n} curve. In the new figure each knock-down factor curve is differently “deformed” in the horizontal direction according to the first term in **(II-35)**. In new coordinates (a, k_0) the two considered points $((A/t_0)_M^*, k_0^*)$ and $((A/t_0)_n^*, k_0^*)$ coincide (the a –coordinate is the same). Generally speaking, there is no reason to expect that other points on these

curves would coincide too. However, the results presented in **Figure II-20** for CF and GF for the case of unit with surface 0^o-layer show that the curves coincide. The extremely high degree of agreement of numerical results for all inspected materials and also embedded layers (**Figure II-3c**) as well, indicates that there may be an exact correlation which we do not know at present. These results imply that knock down factor k_{0n} curves for all possible wavelength $L/t_0 = n$ values coincide when they are plotted against $a = \frac{(A/t_0)_M^*}{(A/t_0)_n^*} \cdot (A/t_0)_n$. Applying **(II-35)** to the master curve we have $a = (A/t_0)_M$. Hence, **(II-35)** can be written as

$$(A/t_0)_M = \frac{(A/t_0)_M^*}{(A/t_0)_n^*} \cdot (A/t_0)_n \quad \text{(II-36)}$$

The numerically established relationship **(II-36)** between both curves allows for a simple recalculation routine: for any selected knock-down factor k_0 and $(A/t_0)_M$ on the master curve the value of amplitude $(A/t_0)_n$ that would give the same knock-down factor for wavelength $L/t_0=n$ is given by

$$(A/t_0)_n = \frac{(A/t_0)_n^*}{(A/t_0)_M^*} \cdot (A/t_0)_M \quad \text{(II-37)}$$

To use **(II-37)** we first have to find $(A/t_0)_n^*$ and $(A/t_0)_M^*$.

An illustration of the procedure is shown in the following figures for CF composite and for the surface 0^o-layer case. The knock-down factor curve for $L/t_0 =6$, shown in **Figure II-18**, is a master curve represented by fitting expression **(II-33)**. It is used to find $k_{0n}(A/t_0)$ for $n=10$.

Performing the FE calculation for $n=10$ waviness with one chosen value of the amplitude $(A/t_0)_{10}^* = 0.7$, the calculated knock-down factor is $k_0^* = 0.536$. From

(II-33)

$$k_0^* = \frac{1}{a+b \cdot (A/t_0)_M^c} \quad \rightarrow \quad (A/t_0)_M^* = 0.312$$

Then a set of values of $(A/t_0)_M$ is chosen, i.e. the first row in **Table II-3**. The corresponding values of k_0 (second row) are calculated from **(II-33)**. Finally **(II-37)** is used to calculate corresponding values of $(A/t_0)_{10}$.

Table 3. Calculation results (For CF/EP) (Unit with surface O^0 -layer)

$(A/t_0)_M$	0	0.05	0.10	0.15	0.20	0.25	0.30	$(A/t_0)_M^* = 0.312$
k_0	1	0.98	0.91	0.83	0.73	0.64	0.56	0.536
$(A/t_0)_{10}$	0	0.11	0.22	0.34	0.45	0.56	0.67	0.70

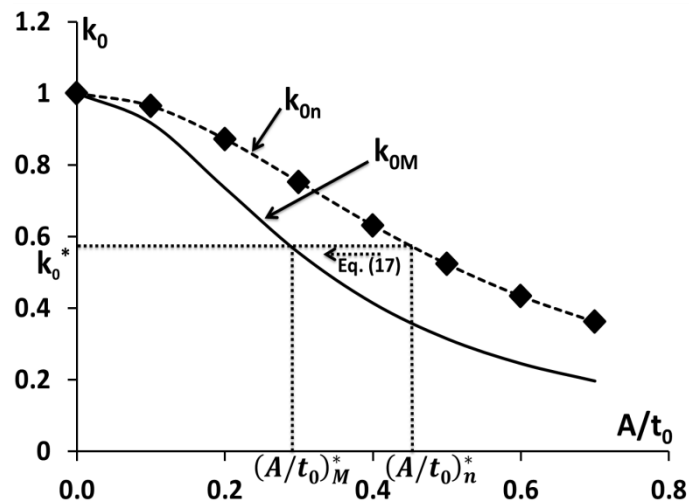


Figure II-19. Master curve approach

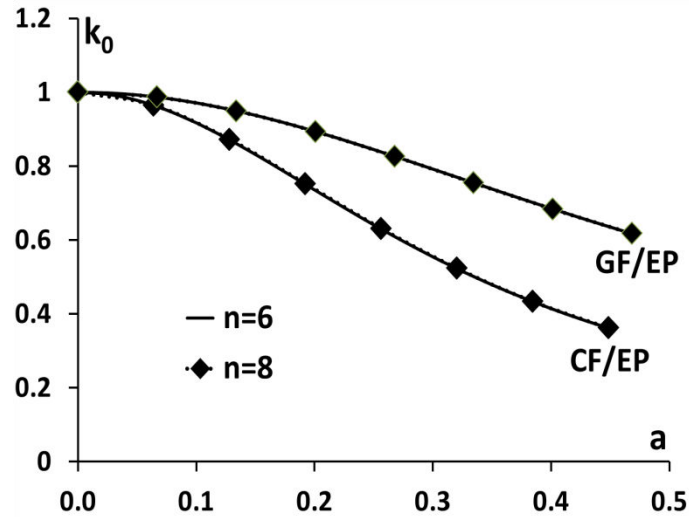


Figure II-20. Figure II-19 after calculation using (II-35) for the case of $LM/t_0=6$ and $Ln/t_0=8$, for CF/EP and GF/EP and for the unit with surface 0^0 -layer.

The 0^0 -layer knock down factors k_0 given in the second row in **Table II-3** are plotted as a function of $(A/t_0)_{10}$ given in the third row of the same table. Thus the 0^0 -layer knock down factor curve is obtained for the case of $L/t_0=10$ using the fitting expression of the master curve and only one FE calculation for amplitude $A/t_0=0.7$ for $L/t_0=10$. The results presented in **Figure II-21a** are for CF/EP material as well as for GF/EP. The fitting constant c in (II-33) is assumed equal to 2 for both materials. The obtained knock-down curve is plotted at the same figure with knock-down factor curve calculated using FE for the same case of $L/t_0=10$. Thus, the master curve approach is thereby shown to give a good agreement within the considered range of amplitude and wavelength.

The same procedure is applied for $L/t_0=15$ composite (see **Figure II-21b**). And the same is done for the unit with embedded 0^0 -layer as well (see **Figure II-22a** and **Figure II-22b**).

The $c=2$ parameter selection is working well for both units and the only remaining unknown constant is “ b ” in the fitting expression. This means that few FE calculated data points may be sufficient to determine the unknown constant “ b ” in the equation of the master curve and only another FE-calculation data point to predict the whole behaviour of the knock down factor at a different wavelength is needed.

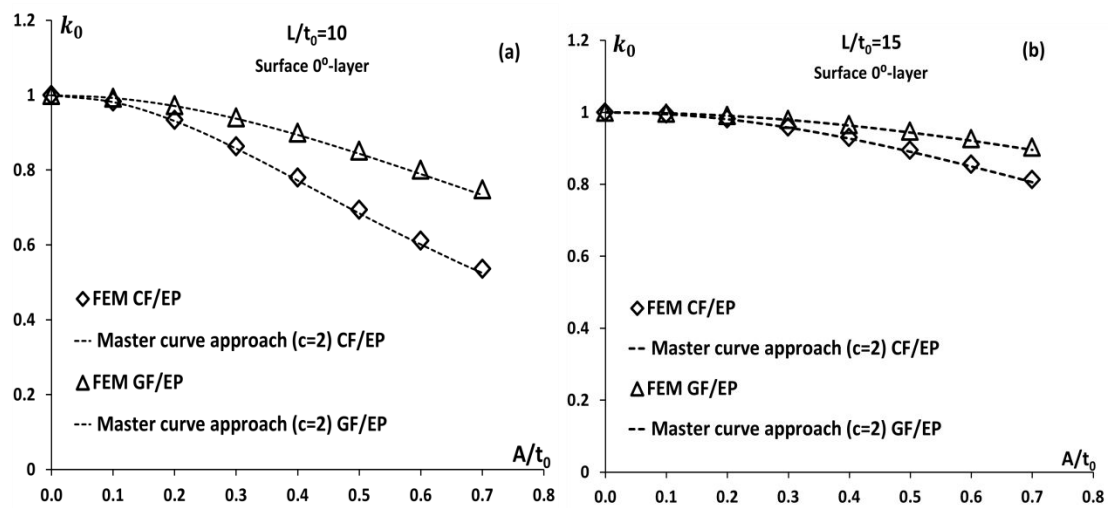


Figure II-21. Comparison of k_0 calculated using FE with k_0 calculated using master curve approach for unit with surface 0^0 -layer **(a)** $L/t_0=10$ and **(b)** $L/t_0=15$.

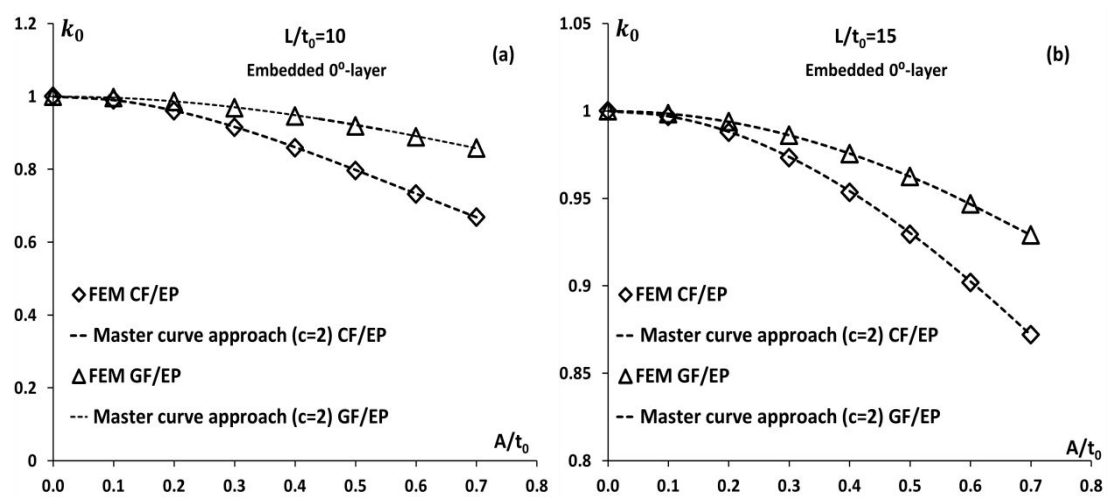


Figure II-22. Comparison of k_0 calculated using FE with k_0 calculated using master curve approach for unit with embedded 0^0 -layer **(a)** $L/t_0=10$ and **(b)** $L/t_0=15$.

Finally k_{NCF} is calculated in **(II-25)** using k_0 determined from the master curve approach together with k_{90} calculated from **(II-23)** and **(II-32)**. The results are presented in **Figures II-23** and **II-24** and are compared to direct FE calculations for NCF knock down factor. If k_{90} is used equal to 1 it means that the effective stiffness of the 90°-layer is considered equal to the transverse stiffness of the UD composite material, and the effect of the waviness and thickness variation on the 90°-layer effective stiffness is neglected. The results corresponding to this case in **Figures II-23** and **II-24** are close to the results using **(II-25)** and k_{90} calculated using **(II-23)** and **(II-32)**. On the other hand, k_0 determined using the master curve approach is rather close to the NCF knock-down factors calculated directly from FE. Since $k_0 < k_{NCF}$, it can be used as a conservative estimation of the NCF composite axial stiffness reduction.

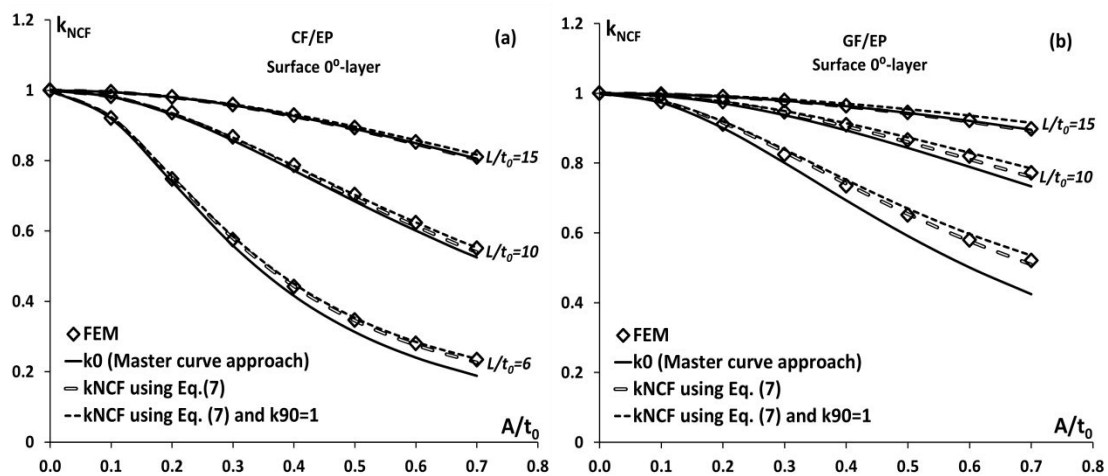


Figure II-23. NCF composite knock down factor with surface 0°-layer **(a)** CF/EP **(b)** GF/EP.

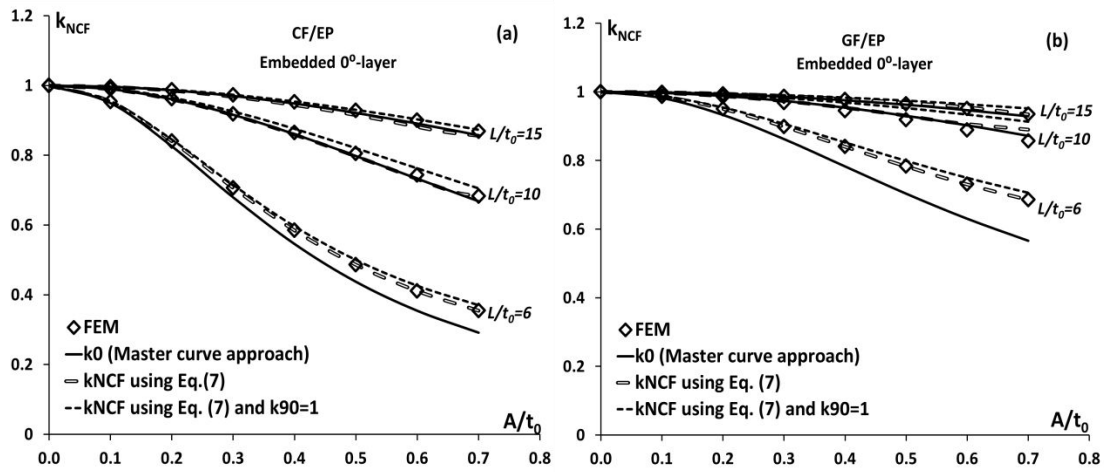


Figure II-24. NCF composite knock down factor with embedded 0° -layer (a) CF/EP (b) GF/EP.

5. Master curve approach for effective stiffness of composite with more complex geometries

5.1. Geometries

Different combinations of the surface and embedded unit cells are realized simulating the stiffness of NCF composite.

First, one unit cell with surface 0° -layer and one unit cell with embedded 0° -layer are combined producing two new meso-cells called: In phase meso-cell (when the waviness of the surface 0° -layer and the waviness of the embedded 0° -layer are in phase), see **Figure II-25a**, and out of phase meso-cell (when the waviness of the surface 0° -layer and the waviness of the embedded 0° -layer are out of phase as in **Figure II-25b**).

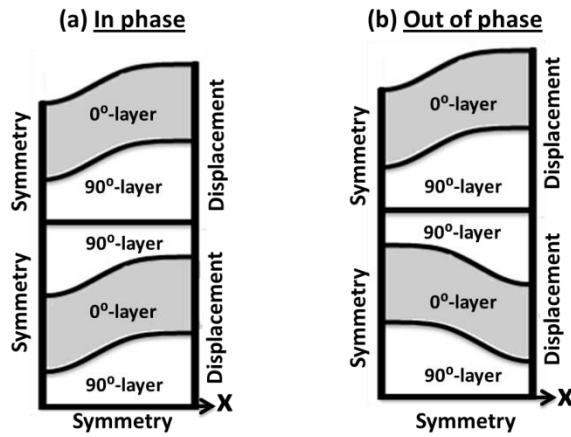


Figure II-25. Meso-cells with in phase and out of phase combinations of surface and embedded unit cells.

Other combinations of meso-cells are realized by placing surface unit cells (**Figure II-26a**) or embedded unit cells (**Figure II-26b**), with different amplitudes and wavelengths of the waviness in series (in chain). Meso-models are used to estimate the effect of interaction between bundles belonging to different units on their effective stiffness.

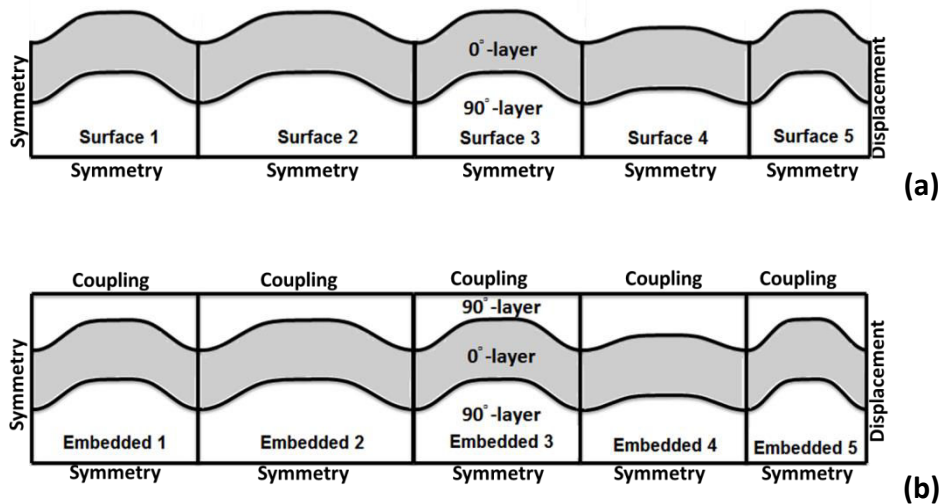


Figure II-26. $0^\circ/90^\circ$ meso-cells with a) surface units b) embedded units

Meso-cells in **Figure II-26a** and **Figure II-26b** are also combined to produce a more complex composite with in phase (**Figure II-27a**) or out of phase (**Figure II-27b**) waviness.

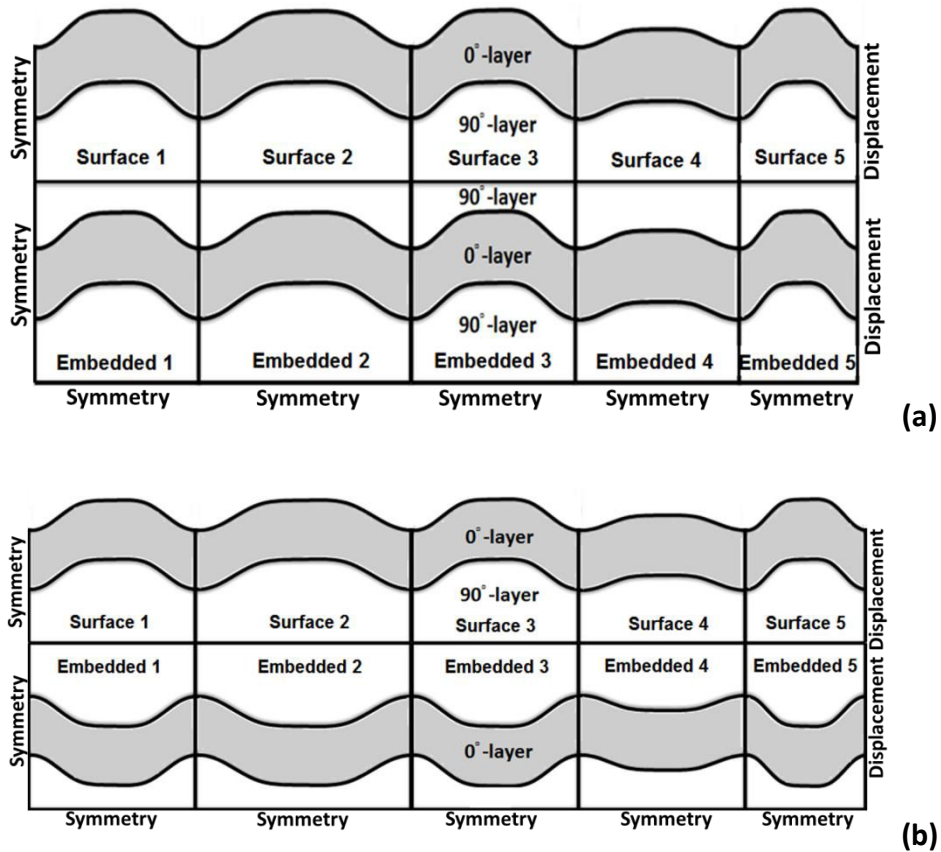


Figure II-27. Laminate made of: **a)** in phase, and **b)** out of phase, meso-cells.

These models will be used in **Section 5.4** and **5.5** to validate the engineering approach developed in **Section 5.3**.

5.2. Development of the master curve approach

In the previous section the master curve approach was developed to calculate knock-down factors for curved 0° -layers. Numerical analysis showed that the 0° -layer knock-down factor versus amplitude curves for any wavelength can be reduced to one master curve by curve shifting. The master curve that shows the knock-down factor

dependence on wave amplitude for a reference wave length is well described by a one-parameter expression with the parameter dependent on the used material

$$k_0 = \frac{1}{1+b(A/t_0)^2} \quad \text{(II-38)}$$

This expression together with the shifting procedure is used to obtain high accuracy analytical predictions for knock down factors for cases with different wavelength and amplitudes. For any new wave length one FE calculations is required. In other words, the fitting parameter “*b*” is not only material dependent but also wavelength dependent. FE parametric analysis was performed to analyse “*b*”, see **Figure II-28**, and a power law is suggested to fit the “*b*” parameter dependence on wavelength.

$$b = c \times (L/t_0)^{-3} \quad \text{(II-39)}$$

The fitting constant “*c*” depends on the used material. Values for the used GF/EP and CF/EP (CF/EP1) are given in **Table II-4**. They are different for surface and for embedded units.

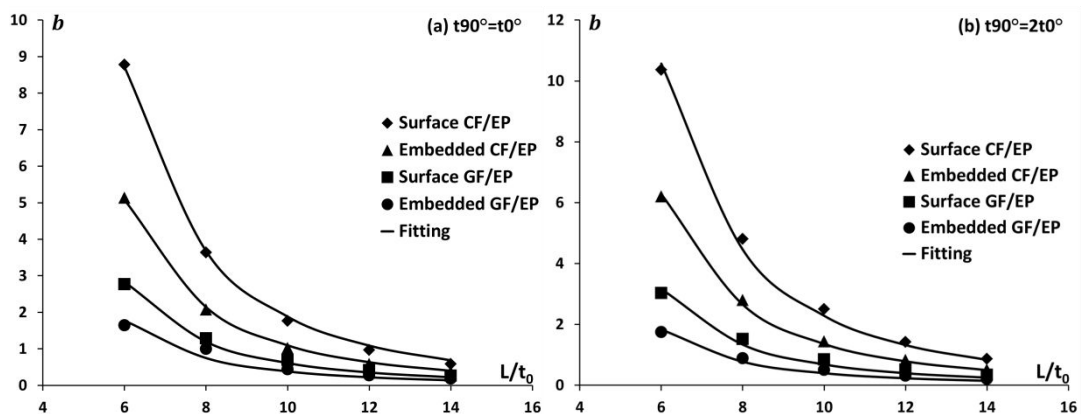


Figure II-28. Fitting of the parameter “*b*”

In **Figure II-28b** and in **Table II-4** a case where the average 90°-layer thickness is doubled ($t_{90}=2t_0$) is also presented. This case will be utilized in **Section 5.5** to

approximately represent the effect of the neighbouring 0°-layer on the knock-down factor.

Table II-4. Fitting constant “c”

C	CF/EP		GF/EP	
	Surface 0°-layer	Embedded 0°-layer	Surface 0°-layer	Embedded 0°-layer
t90°=t0°	1882.680	1097.603	612.168	383.528
t90°=2t0°	2283.176	1357.775	683.734	395.758

Since the c-constant is material dependent, each new material requires one FE calculation. Estimation of data in **Table II-4** leads to conclusion that in all comparable cases this constant is roughly three times larger for CF/EP composite. This value is rather close to the longitudinal modulus ratio of these two materials in **Table II-1** ($141/46.8=3.01$). This may be an indication that the longitudinal modulus of the corresponding UD material is the main parameter defining the c-parameter. It should be reminded that all results in this study are obtained assuming sinusoidal shape of the waviness.

5.3. Engineering approach for the amplitude and wavelength’s of an equivalent cell

We consider surface or embedded unit cells with different amplitudes and different wavelengths combined in chain (See **Figure II-26**) producing a NCF composite made of n unit cells. The approach is to replace these chains by one equivalent cell (correspondingly surface or embedded). The equivalent cell has to have an amplitude and wavelength that lead to the same stiffness as the initial chain of unit cells has. The objective is to find the equivalent amplitude and wavelength. This analysis has practical significance because this is the way how experimental (for example, optical)

observations can be implemented in a model. The question is: what is the proper averaging procedure for observation data? The simplest and commonly used method is to calculate the average of the amplitude and of the wavelength by simple summation of the local amplitudes and wavelengths **(II-40)** taking into account the volume fraction V_i **(II-41)** of each unit which leads to rule of mixtures

$$(A/t_0)_{av} = \sum_{i=1}^n V_i (A/t_0)_i \quad \text{And} \quad (L/t_0)_{av} = \sum_{i=1}^n V_i (L/t_0)_i \quad \text{(Method1)} \quad \text{(II-40)}$$

n - is the number of unit cells in the chain, V_i is the volume fraction of the i -th unit cell in the chain

$$V_i = \frac{V_i^{Unit\ cell}}{V_{Total}^{NCF}} \quad \text{(II-41)}$$

FEM results in **Figure II-29** discussed in detail later show that this simple way of averaging significantly overestimates the stiffness.

A more accurate and mechanics based procedure is based on summation rule for stiffness of cells combined in chain. For the equivalent cell

$$\frac{1}{Q_{11}^{eq}} = \sum_{i=1}^n \frac{V_i}{Q_{11}^i} \quad \text{(II-42)}$$

which using **(II-24)** can be written as

$$\frac{1}{k_0^{eq} Q_{11}^0 + k_{90} \frac{t_{90}}{t_0} Q_{22}^{90}} = \sum_{i=1}^n \frac{V_i}{k_0^i Q_{11}^i + k_{90} \frac{t_{90}}{t_0} Q_{22}^{90}} \quad \text{(II-43)}$$

Introducing notation

$$R = k_{90} \frac{t_{90}}{t_0} \frac{Q_{22}^{90}}{Q_{11}^0} \quad \text{(II-44)}$$

we can rewrite **(II-43)** as

$$\frac{1}{k_0^{eq} + R} = \sum_{i=1}^n \frac{V_i}{k_0^i + R} \quad \text{(II-45)}$$

Using the knock-down factor of the equivalent cell

$$k_0^{eq} = \frac{1}{1+b_{eq}(A/t_0)_{eq}^2} \quad (\text{II-46})$$

equation (45) can be rearranged in form

$$(A/t_0)_{eq} = \sqrt{\frac{1}{b_{eq}} \frac{(1+R) \sum_{i=1}^n \frac{V_i}{k_0^i + R} - 1}{1-R \sum_{i=1}^n \frac{V_i}{k_0^i + R}}} \quad (\text{II-47})$$

In the above form the amplitude of the equivalent cell cannot be determined because b_{eq} depends on the length of the equivalent cell (equations (38), (39)) which is not known yet. However, (47) can be simplified: it was demonstrated that $k_{NCF} \approx k_0$, which means that one can assume $k_{g0} \approx 1$. Similar derivation as show above leads to

$$(A/t_0)_{eq} = \sqrt{\frac{1}{b_{eq}} \sum_{i=1}^n V_i b_i (A/t_0)_i^2} \quad (\text{Method 2}) \quad (\text{II-48})$$

The same expression is obtained when $R \rightarrow 0$, which is the case when the contribution of the 90°-layer can be ignored.

Method 2 includes b_i and also b_{eq} which are LTi dependent and therefore b_{eq} for the equivalent cell can not be determined at the current stage.

The wavelength of the equivalent unit is determined through the average waviness angle.

$$\tan(\alpha_{av}) = \sum_{i=1}^n \frac{4(A/t_0)_i}{L_i} \quad (\text{II-49})$$

$$\frac{(L/t_0)_{eq}}{4} = (A/t_0)_{eq} / \tan(\alpha_{eq}) = (A/t_0)_{eq} / \sum_{i=1}^n \frac{4A_i}{L_i} \quad (\text{II-50})$$

In **Method 2** $(L/t_0)_{eq}$ depends via $(A/t_0)_{eq}$, see (II-48), on b_{eq} whereas b_{eq} for the equivalent cell depends on $(L/t_0)_{eq}$. In other words both parameters are coupled and

an iterative solution is one of the options: in first iteration we assume that b_i and b_{eq} can be neglected in (II-47) leading to

$$(A/t_0)_{eq} = \sqrt{\sum_{i=1}^n V_i (A/t_0)_i^2} \quad \text{(Method 3)} \quad \text{(II-51)}$$

This value of $(A/t_0)_{eq}$ is used in (II-50) to find the wave length $(L/t_0)_{eq}$ and then b_{eq} is found using (II-39). After that (II-48) can be used to refine the value of $(A/t_0)_{eq}$ etc. Obviously, **Method 3** is the first iteration in a more complex routine for **Method 2**.

5.4. Stiffness of chain of cells

Axial stiffness of the meso-scale composite consisting of a chain of $n=5$ unit cells, see **Figure II-26**, was calculated analysing separately chain of surface cells, **Figure II-26a**, and embedded cells, **Figure II-26b**. The waviness parameters for cells used in calculations are given in **Table II-5**. The waviness parameters for the equivalent cell used in engineering calculations were calculated according the three methods described in **Section 5.3**. The results are given in **Table II-6**.

Table II-5. Used amplitudes and wavelengths

5 cells	i	1	2	3	4	5
	$(A/t_0)_i$	0.12	0.06	0.15	0.18	0.09
$(L/t_0)_i$	10	8	14	6	12	

Table II-6. Average amplitude and wavelength of the equivalent cell

	CF/EP				GF/EP			
	Surface		Embedded		Surface		Embedded	
	$(A/t_0)_{eq}$	$(L/t_0)_{eq}$	$(A/t_0)_{eq}$	$(L/t_0)_{eq}$	$(A/t_0)_{eq}$	$(L/t_0)_{eq}$	$(A/t_0)_{eq}$	$(L/t_0)_{eq}$
Method 1 $(A/t_0)_{eq}$ (Eq.(17)) $(L/t_0)_{eq}$ (Eq.(17))	0.404	10.81	0.404	10.81	0.404	10.81	0.404	10.81
Method 2 $(A/t_0)_{eq}$ (Eq.(25)) $(L/t_0)_{eq}$ (Eq.(27))	0.421	9.334	0.423	9.368	0.418	9.257	0.407	9.020
Method 3 $(A/t_0)_{eq}$ (Eq.(28)) $(L/t_0)_{eq}$ (Eq.(27))	0.423	9.370	0.423	9.317	0.423	9.370	0.423	9.370

FE models containing these 5 cells were created and the calculated Q_{11}^{NCF} for GF/EP and CF/EP composites is presented in **Figure II-29**. Stiffness of a laminate with $(A/t_0) = 0$ is presented for comparison. The stiffness of the embedded laminate with $(A/t_0) = 0$ is lower than for the laminate consisting of surface units because the fraction of the 0° -layer is smaller in this model (1/3).

Stiffness of the same chain of cells was also calculated analytically using “constant force” model

$$\frac{1}{Q_{11}^{NCF}} = \sum_{i=1}^n \frac{V_i}{Q_{11}^i} \quad \text{(II-52)}$$

Here stiffness of each cell Q_{11}^i was calculated using the master curve: applying **(II-24)** where the knock down factor was found with **(II-38)**, **(II-39)**. The excellent agreement with FEM for all analysed cases confirms the applicability of **(II-52)**.

Next the concept of the equivalent unit cell representing the composite chain was investigated. The stiffness of the defined equivalent cell was calculated a) using FEM; b) using the master curve approach. The results of a) and b) calculations are almost coinciding. The procedure in the master curve approach is as before: the constant b_{eq} is calculated for the equivalent wavelength using expression **(II-39)**, and then introduced in expression **(II-38)** together with the equivalent amplitude to calculate the knock down factor of the 0° -layer in the equivalent unit cell. The knock-down factor is used in the CLT expression **(II-24)**, to calculate the axial stiffness of the equivalent unit.

Among the three methods defining parameters of the equivalent cell **Method 1** based on simple averaging of amplitude and wavelength is the less accurate: for both materials and for surface as well as embedded composites chains it significantly

overestimates the composite stiffness. The results in **Figure II-29** show that the axial stiffness of the equivalent cell with average amplitude and wavelength calculated using **Method 2** and **Method 3** are in rather good agreement to the axial stiffness of NCF composite. **Method 3** gives almost the same results as **Method 2**, which means, that ignoring the variation of the parameter bi does not lead to any considerable error in calculation of the average amplitude.

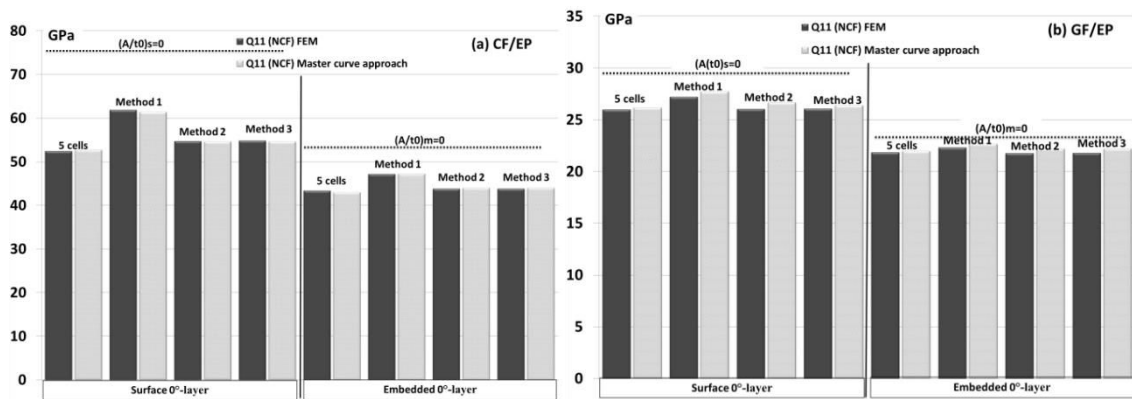


Figure II-29. Axial stiffness of a combination of 5 cells of surface and embedded unit cells calculated using FEM for the whole chain as well as for the three methods based on the concept of “equivalent unit cell”: **a)** CF/EP **b)** GF/EP. Calculations according to the master curve approach are also presented for all four cases.

5.5. Interaction effects of curved bundles in cells connected “in parallel”

The idealized meso-geometry of the NCF composite containing two symmetric layers (chains of units) is not typical in practice. It was shown previously that surface tractions due to interaction with the surrounding material strongly affect the knock-down factor of the 0°-layer. This means that in a multi-layer NCF composite with many embedded and surface unit cells the waviness parameters of 0°-layer in one cell can significantly

affect the knock-down factor of the 0° -layer in a cell located on the top or below this cell.

The interaction effect on knock-down factor was investigated applying FEM on the models shown in **Figure II-25**. The objective was to find simplified geometry (representative cell) that would give a satisfactory description for the large variety of the parameters in two unit cells connected in parallel.

Since one of the possible simplifications is replacing the neighbouring cell with a 90° -layer of the same thickness (for 0° -layer $E_3 = E_T$), we start the analysis with the effect of the thickness of the 90° -layer on the knock down factor of the 0° -layer. In FEM, both models (with surface 0° -layer and embedded 0° -layer) presented in **Figure II-3b** and **Figure II-3c** are considered changing the thickness ratio between the layers as following: $t_{90}/t_0 = 1, 2, 3, 4$. The knock down of the 0° -layer is presented as a function of the amplitude in **Figure II-30a** and **Figure II-30b**. Calculation were performed for wavelength $(L/t_0)=6$.

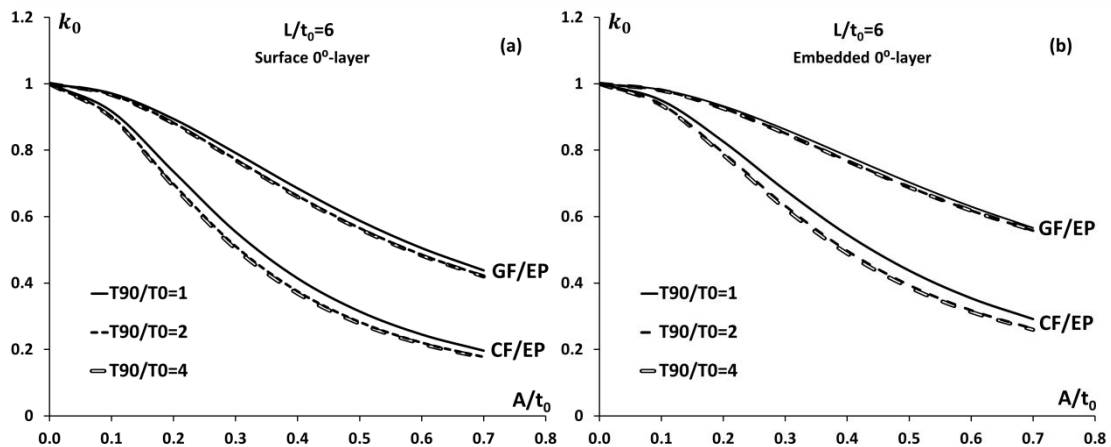


Figure II-30. Effect of layers' thickness ratios on 0° -layer's knock down factor for the unit cell with: **a)** Surface 0° -layer **b)** Embedded 0° -layer.

The effect of the thickness of the 90°-layer on the knock-down factor reduction of the 0°-layer in **Figure II-30** is not significant, the reduction being larger with increasing t_{90}/t_0 . The largest change is between $t_{90}/t_0=1$ and $t_{90}/t_0=2$. For the thickness ratios higher than 2 the knock down factor is almost the same as for the case $t_{90}/t_0 = 2$.

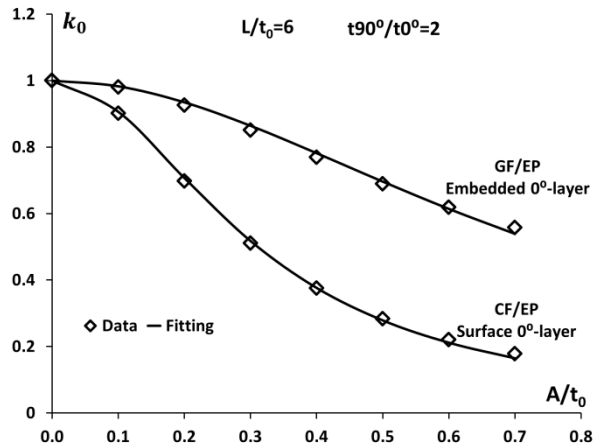


Figure II-31. Master curve Fitting

The knock-down factor data from FEM were fitted using the master curve expression **(II-38)**. Good fitting was obtained (see **Figure II-31**) and the fitting parameter “b” for the analysed cases is given in **Table II-7**.

Next, we analyse meso-cells, shown in **Figure II-25**, by changing the amplitude of the 0°-layer in one unit and calculating the knock-down factor of the 0°-layer in the other unit. Changing the waviness in one 0°-layer, the interface tractions between units are changed (boundary conditions for the unit cell are not symmetry conditions as it was in **Figure II-3**) as well as the knock-down factors.

Table II-7. Fitting constant “b”

t_{90°/t_{0°	CF/EP		GF/EP	
	Surface	Embedded	Surface	Embedded
1	8.781	5.136	2.766	1.646
2	10.360	6.201	3.031	1.746
4	10.657	6.392	3.067	1.750

Focusing on the 0° -layer in the surface unit cell, the amplitude of the surface 0° -layer $(A/t_0)_s$ is fixed, changing the amplitude of the 0° -layer $(A/t_0)_m$ in the embedded and determining the knock down factor of the 0° -layer in the surface unit. The percentage of change is calculated with respect to the knock down factor in the surface unit when $(A/t_0)_m = 0$ (flat layer). The same was done also for the 0° -layer in the embedded unit by fixing $(A/t_0)_m$ and changing $(A/t_0)_s$ and calculating the knock down factor of the 0° -layer in the embedded cell. Results for the most extreme effect of the neighbouring layer are presented in **Table II-8** and **Table II-9** were also values corresponding to unit cells with symmetry boundary conditions are presented for comparison.

Table II-8. Knock down factor of 0° -layer in the surface unit with $(A/t_0)_s = 0.7$ and $(L/t_0) = 6$.

$(A/t_0)_m$	CF				GF			
	In phase		Out of phase		In phase		Out of phase	
	ko°	%	ko°	%	ko°	%	ko°	%
0	0.178		0.178		0.424		0.424	
0.7	0.165	-7.30	0.194	+8.98	0.417	-1.65	0.431	+1.65
<i>Fig 1a</i> $t_{90^\circ}/t_{0^\circ}=2$			0.177				0.421	
<i>Fig 1a</i> $t_{90^\circ}/t_{0^\circ}=1$			0.196				0.438	

Table II-9. Knock down factor of 0° -layer in the embedded unit with $(A/t_0)_m = 0.7$ and $(L/t_0) = 6$.

$(A/t_0)_s$	CF				GF			
	In phase		Out of phase		In phase		Out of phase	
	ko°	%	ko°	%	ko°	%	ko°	%
0	0.276		0.276		0.563		0.563	
0.7	0.261	-5.43	0.294	+6.52	0.549	-2.48	0.572	+1.59
<i>Fig 1b</i> $t_{90^\circ}/t_{0^\circ}=2$			0.262				0.557	
<i>Fig 1b</i> $t_{90^\circ}/t_{0^\circ}=1$			0.291				0.566	

Increasing the wave amplitude of the neighbouring 0° -layer, the knock-down factor of the 0° -layer in concern increases in the out of phase case and decreases in the in phase case. The thickness of the 90° -layer in between two 0° -layers is the same and constant ($t_{90^\circ}=2t_{0^\circ}$) in average. The symmetric shape of the out of phase model compensates the bending of the unit and makes the 0° -layer stiffer (the result is similar as using symmetry condition at the unit interface). The change (%) with respect to the knock-down factor value when the neighbouring layer is straight also shown in **Tables II-8, II-9** is very small for GF/EP composite (about 2%) but larger for CF/EP (10% for surface units and 6% for embedded units). We conclude that the effect of 0° -layer waviness on the knock-down factor of the neighbouring one is rather small and, therefore, it could be accounted for using simple approximations.

To identify this simple approximation, we compare the knock down factor of the 0° -layer in the meso-cell to the factor in the unit cell with $t_{90^\circ}=2t_{0^\circ}$ (as demonstrated above cells with $t_{90^\circ}>2t_{0^\circ}$ render the same result). For all the cases of out of phase meso-cells, the approximation of replacing the neighbouring waved 0° -layer by a 90° -layer with $t_{90^\circ}=2t_{0^\circ}$ would lead to under-estimation of the knock-down factor by 2-10%. For the in phase meso-cell the same operation would lead to over-estimation of the knock down of the 0° -layer in concern by about 0.3-7%. In a real NCF composite, the unit cells are randomly shifted and, therefore, the in-phase and out-of-phase

meso-cells represent extreme cases. Since the suggested approximation underestimates the factor for in-phase units and overestimates it for out-of-phase units, it may lead to satisfactory stiffness reduction predictions in NCF composites containing all these meso-cells. Certainly, more detailed and more accurate approximations are possible, for example applying different approximations for in-phase and out-of-phase meso-cells.

Finally, the approximation for knock-down factors suggested above was used for symmetric NCF composite consisting of 5 meso-cells with different amplitudes and same wavelength (L/t_0) = 10 (**Figure II-27**).

The stiffness of the two NCF composites shown in **Figure II-27**, calculated using FEM, is labelled in **Figure II-32** as “FEM F27a” and “FEM F27b” respectively. The composites in **Figure II-27** were treated also analytically using the engineering approach based on the master curve. First the knock-down factors of all units were determined accounting for the 0°-layer interaction in the approximate way described above (using $t_{90} = 2t_0$ in the unit cell). In this routine the value of "c" in **(II-39)** is taken from **Table II-4** for case $t_{90} = 2t_0$ and the calculated "b" is substituted in **(II-38)** to calculate the knock-down factor. After that the stiffness of the unit cell is calculated using **(II-24)** with the real thickness of the 90°-layer in the cell, $t_{90} = t_0$. Then the stiffness of the chain of unit cells (surface chain is treated separately from the embedded chain) is calculated using

$$\frac{1}{Q_{11}^{NCF(surface)}} = \sum_{i=1}^n \frac{V_{i(surface)}}{Q_{11}^{i(surface)}} \quad \frac{1}{Q_{11}^{NCF(embed)}} = \sum_{i=1}^n \frac{V_{i(embed)}}{Q_{11}^{i(embed)}} \quad \text{(II-53)}$$

The volume fractions of unit cells are calculated as follows

$$V_{i(surface)} = \frac{vol_{i\ surface}}{vol_{Total}^{surface}} \quad \text{(II-54)}$$

$$V_{i(emb)} = \frac{vol_{i^{embedded}}}{vol_{Total}} \quad (\text{II-55})$$

The stiffness of both chains is used to calculate the stiffness of the NCF composite shown in **Figure II-27**.

$$Q_{11}^{NCF} = V_{surf} Q_{11}^{NCF(surf)} + V_{emb} Q_{11}^{NCF(emb)} \quad (\text{II-56})$$

In **(55)** V_{surf} and V_{emb} are volume fractions of the surface chain and embedded chain respectively.

The NCF stiffness calculated using this technique is denoted in **Figure II-32** as “master”. The values are between the FEM values for in-phase (**Figure II-27a**) and out-of-phase (**Figure II-27b**) composites. In the used approximation this technique does not distinguish between in-phase and out-of-phase composites. This is because calculating the effect of the neighbouring 0°-layer on the knock-down factor the 0°-layer is replaced by 90°-layer which does not have any in-phase or out-of-phase waviness.

An alternative for FEM as well as for analytical calculations is replacing the composite in **Figure II-27** by an equivalent meso-cell consisting of two equivalent unit cells connected in parallel. The potential of this approach is analysed next. The equivalent amplitude of 0°-layer in each equivalent unit cell is calculated separately using **Method3 (II-51)** with V_i being either $V_{i(surf)}$ or $V_{i(emb)}$. The equivalent wavelength is calculated according to **(50)** which in the used calculation case (units of equal length) is equal to the length of the unit cell.

The equivalent meso-cell with two unit cells in parallel was analysed using a) FEM; b) analytically. The equivalent meso-cell is different for the in- and out-of-phase cases in

Figure II-27. This is reflected in two different FEM values “FEM F27a-eq” and “FEM F27b-eq” in **Figure II-32**.

The analytical solution for the equivalent meso-cell is based on the master curve expressions: a) the knock down factor of 0⁰-layer in each of the two equivalent cells is calculated using expressions **(II-38)**,**(II-39)** (using "c" in **(39)** from **Table II-4** for case $t_{90} = 2t_0$ to find parameter “b”). The effective stiffness of the equivalent unit is then calculated using expression **(II-24)** which is based on CLT in equation **(II-24)**. Finally stiffness of both equivalent units is used to calculate the NCF composite stiffness using

$$Q_{11}^{NCF} = V_{eq(surf)}Q_{11}^{eq(surf)} + V_{eq(emb)}Q_{11}^{eq(emb)} \quad \text{(II-57)}$$

The results are shown in **Figure II-32** as “Master-eq”. Results using the equivalent meso-cell are very similar as obtained using the detailed meso-structure in **Figure II-27**. It proves that the geometrical meso-structure in **Figure II-27** is well represented by one equivalent meso-cell with equivalent amplitude and wavelength obtained using **Method 3**.

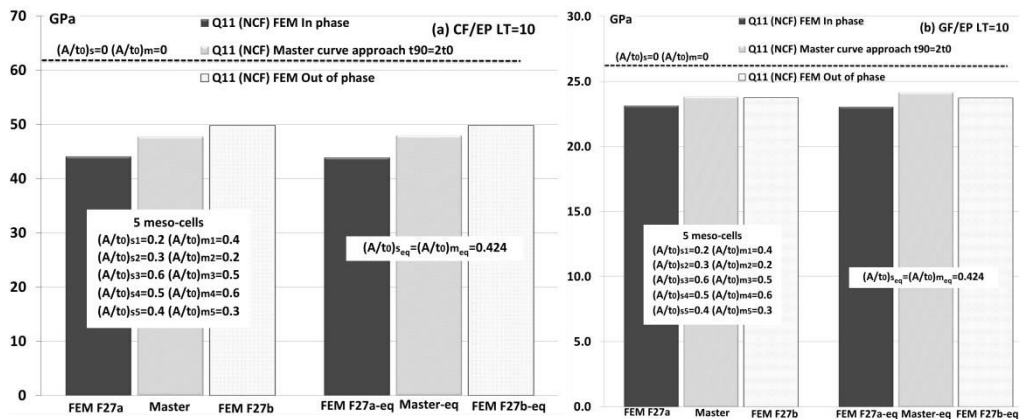


Figure II-32. Axial stiffness of in phase and out of phase combinations of surface and embedded unit cells: **a) CF/EP b) GF/EP**.

6. Conclusions

The effect of the 0° -bundle waviness on stiffness of cross-ply NCF composites was modelled. Multiscale approach was used by first calculating the homogenized bundle material properties from its constituents by using an assumed hexagonal fibre packing. The bundle structure of the curved 0° -layer and the bundle structure of the 90° -layer with varying thickness are then replaced with homogenized materials. Finally, the curved 0° -layer and the 90° -layer with varying thickness were replaced by flat layers with effective stiffness and classical laminate theory was used to calculate the macroscopic stiffness. The presented study focused on the axial macroscopic stiffness.

The macroscopic axial stiffness was expressed through the effective stiffness of the curved 0° -layer and the effective stiffness of the 90° -layer with varying thickness. It was shown that the effective stiffness of a layer in the composite can be calculated averaging the apparent stiffness, which are on the right and the left edges of the layer. These two forces to layer are different due to varying layer thickness and due to the interaction between layers resulting in normal and shear stresses at the $0^\circ/90^\circ$ -layer interface.

Using this approach the effective 0° -layer stiffness was calculated analysing isolated curved 0° -layer subjected not only to end loading, but also to surface loading. To identify the surface loads to be applied, a detailed FE-analysis of the interface stresses was performed. It is concluded that these stresses can be approximated by a sinus shaped function with amplitude dependent on the wave length and amplitude of the curve normalized with respect to the layer nominal thickness. Fitting expressions for

the stress amplitude dependence on these layer waviness parameters were obtained, and are given in Appendix.

The described sinus shaped surface loads were applied to isolated curved 0° -layer FE-model together with end loading showing that the calculated effective stiffness of the layer is in good agreement with the effective stiffness of the 0° -layer extracted from the cross-ply composite analysis. This proves that further efforts are meaningful to develop analytical approximate models for curved beams with sinusoidal surface tractions.

Finally, the calculated effective 0° -layer stiffness was successfully used to calculate the macroscopic stiffness of three different composites proving validity of the used multiscale approach. It was also shown that without losing accuracy the effective stiffness of the 90° -layer (which generally speaking should be calculated numerically considering 90° -layer with varying thickness and applied surface and end loads) can be replaced by the transverse stiffness of the homogenized 90° -layer material.

In another approach, numerical parametric FE-analysis showed that the axial stiffness reduction (knock-down factor) of a cross-ply type NCF composite made of carbon fibre (CF) or glass fibre (GF) bundles with out-of-plane waviness of a surface 0° -layer or embedded 0° -layer is almost the same as the effective stiffness reduction of the curved 0° -layer. This conclusion holds for a large variety of wavelength and wave amplitudes of imperfections.

Analysing the calculated 0° -layer knock-down factor versus the wave amplitude curves for NCF composites with different wavelength we observed that these curves for

different wavelength can be reduced to one master curve by changing the scale of the wave amplitude axis.

It was found analysing results for CF and GF cases that the numerical data building the master curve can be fitted by a very simple one-parameter function. Thus, for a given material only a few FE calculations for a selected wavelength and amplitude are needed to construct the master curve. More calculations would serve the validation purpose.

To construct the 0° -layer knock-down factor versus wave amplitude curve for a different wavelength only one FE calculation is required for arbitrary selected amplitude. Predictions performed for CF and GF NCF composites show a very good agreement with direct FE calculations.

Axial stiffness of a symmetric NCF composite, consisting of many $0^\circ/90^\circ$ unit cells with different amplitudes and wavelength of the 0° -layer, is calculated using FEM and also using analytical models with knock-down factors for curved 0° -layers.

Analytical expression for knock-down factor of the 0° -layer in the unit cell is presented. It is simple but very accurate fitting expression based on extensive FEM parametric analysis and reflects the effect of the local amplitude and wavelength of the 0° -layer on the effective stiffness of the layer in the unit cell. There is only one parameter in these expressions which depends on the used material (values of this parameter are presented for typical GF/EP and CF/EP materials), which means that for a new material one FEM calculation for simple unit cell with fixed amplitude and wavelength is enough to obtain knock-down factors for any combination of amplitude and wavelength. It was found that the value of the knock down factor is affected by the

presence and waviness of the 0° -layer in the neighbouring unit cell. In the current routine this effect is accounted for in a very simple way: assuming that the effect is the same as increasing the thickness of the 90° -layer. In the next step of simulations rule of mixtures and constant force assumptions are used when appropriate. Analytical modelling gives results in a good agreement with FEM.

An alternative approach, attractive for experimental characterization, is to use the information regarding the variation of local waviness to create an equivalent meso-cell for the NCF composite. Three different methods to identify parameters of the equivalent meso-cell are discussed and good agreement with FEM is demonstrated.

Finally, Axial stiffness of a symmetric NCF composite, consisting of many $0^\circ/90^\circ$ unit cells with different amplitudes and wavelength of the 0° -layer, is calculated using FEM and also using analytical models with knock-down factors for curved 0° -layers (Master curve expression) which is simple but very accurate fitting expression based on extensive FEM parametric analysis and reflects the effect of the local amplitude and wavelength of the 0° -layer on the effective stiffness of the layer in the unit cell. There is only one parameter in these expressions which depends on the used material (values of this parameter are presented for typical GF/EP and CF/EP materials), which means that for a new material one FEM calculation for simple unit cell with fixed amplitude and wavelength is enough to obtain knock-down factors for any combination of amplitude and wavelength. It was found that the value of the knock down factor is affected by the presence and waviness of the 0° -layer in the neighbouring unit cell. In the current routine this effect is accounted for in a very simple way: assuming that the effect is the same as increasing the thickness of the 90° -

layer. In the next step of simulations rule of mixtures and constant force assumptions are used when appropriate. Analytical modelling gives results in a good agreement with FEM.

An alternative approach, attractive for experimental characterization, is to use the information regarding the variation of local waviness to create an equivalent meso-cell for the NCF composite. Three different methods to identify parameters of the equivalent meso-cell are discussed and good agreement with FEM is demonstrated.

Chapter III

Damage in Carbon fibre/polyimide laminates

1. Introduction

An increasing interest of aerospace industry in composite materials for applications in harsh environments has been driving improvement and development of new composites. In addition to good mechanical performance some components require materials suitable for the environment in which it would be functioning. For example, the composites designated for aero-engine applications considered in this chapter need to perform good at high temperatures. Thermal cycling (fatigue) and long exposure to elevated temperatures (aging) can cause changes in the morphology, strength and stiffness [49-51]. Therefore understanding the behaviour of a composite material under this type of environmental exposure is of great importance.

Many researches are dedicated to study the thermal stability of the composite by quantifying the effect of thermal fatigue and aging on the mechanical properties and the damage development [52-54]. The effect of thermal cycling (-100°C,100°C) and thermal aging (250h, 400h at 110°C) on mechanical performance of carbon fibre/RTM6 resin and carbon fibre/BMI resin cross-ply laminates was studied in [55] showing that the intralaminar crack density is a clear function of aging time, indicating the matrix and interface degradation. The elevated temperature level during thermal cycling with a fixed lowest level has significant effect on the damage level [56-57]. At the highest temperature in the cycle the composite laminate is close to the stress-free state and, therefore, thermo-elastic analysis cannot explain the role of the highest temperature

in the damage development. Using Paris law with energy release rate (ERR) change during the cycle to explain fatigue crack propagation, the highest temperature is of importance because the ERR change is larger. Nevertheless, it is only one of the possible reasons: during exposure to high temperature irreversible phenomena take place and when the lowest temperature in the cycle (with high stresses) is reached micro-damage evolves. Possible causes for degradation are the disintegration of the molecular network leading to degradation of the resin properties. In [51] authors demonstrated that this effect can be intensified and accelerated if an elevated pressure is added.

The degradation may be quantified by the weight loss measurement either after thermal cycling or after isothermal aging [58-59]. It has been demonstrated that the isothermally aged woven composite made of carbon fibre/epoxy loses more weight than the thermally-cycled specimens throughout the entire range of the equivalent aging time at 170°C. This was explained by the volumetric relaxation of the polymer matrix after each cycle and by the diffusion rate of oxygen through the epoxy matrix during thermal cycling, which is considerably lower than the diffusion rate at isothermal condition. Another study [60] showed that the aging time of carbon fibre/epoxy (IMS/977-2) composite (at 217°C) has an effect on its viscoelastic properties. This effect is linked to the effect on the glass transition temperature. The chemical and physical changes occurring during aging are accompanied by a variation in molecular mobility, the glass transition temperature increases at the beginning of aging followed by a decrease.

It is clear that the matrix dictates the material's response at high temperature. The degradation of neat polyimide resin and CF/polyimide composite at (320°C, 360°C) was

studied in [61]. The authors have proved that the composite weight loss comes only from the matrix degradation indicating that the carbon fibres in the composite have good thermal oxidation resistance. The choice of the appropriate resin is the most complicated issue for the high temperature composites. Development of high temperature polymeric resins was reported in [62] replacing a commonly used epoxy, with the limit of service temperature above 135°C, by polyimide resin in composites for service temperatures between 250°C and 350°C.

2. Objectives

The objective of this chapter is to study the thermal fatigue resistance and the thermal stability of quasi-isotropic CF/polyimide woven composite by analysing the initiation and evolution of micro-cracking due to thermal cyclic loading or after isothermal aging at 288°C and afterwards, to study the multiple intralaminar cracking and delamination growth during tensile loading of the same material. The experimental findings in different layers are explained analysing the micro-cracking initiation and growth using stochastic initiation strength distribution approach and fracture mechanics, focussing on

- Differences in crack density growth in different layers
- Comparing composites with two modifications of the polyimide
- Analysing the effect of high temperature aging on intralaminar cracking

3. Experiments

3.1. Materials description

The composite material studied in this chapter is designed for severe operating temperatures with a potential for aero-engine applications. Quasi-isotropic $[(+45/-45)/(90/0)]_2s$ "laminates" were prepared using 8-harness satin weave based on Cytec T650 carbon fibres and thermosetting polyimide resin denoted NEXIMID® MHT-R (MHT-R). This resin is provided by Nexam Chemical AB; it is a low molecular weight phenylethynyl terminated polyimide that contains a combination of 4-(Phenylethynyl)Phthalic Anhydride (4-PEPA), end-group cross-linker and ethynyl bis-phthalic anhydride (EBPA) main chain cross-linker. The use of optimized combinations of the 4-PEPA and EBPA (both Nexamide™ type) enables ultimate Tg of around 370°C.

Specimens were cut from 2 different plates labelled 432, 433. These plates were manufactured at Swerea SICOMP, Sweden, using resin transfer moulding (RTM) in stainless steel tool using a flow and pressure controlled injection piston. The material was initially cured at 340°C for 30min followed by 2.5h post cure at 370°C using 12 bar pressure. In the 433 plate, the MHT-R resin was mixed with 4% of an additive A57, which is a reactive diluent acting to lower the viscosity during processing. Both plates were cooled down during 12 hours and demoulded at 70°C then cooled down to 0°C for 2 hours.

The volume fraction of fibres is around 60%; the Tg is around 370°C; the uncured resin melts between 200°C and 250°C and the initiation of cross-linking happens above 320°C. Some mechanical properties of the T650/MHT-R quasi-isotropic laminate [63] are given bellow:

$E_{\text{Tensile}} \approx 48\text{GPa} / E_{\text{Compression}} \approx 45\text{GPa}$.

Tensile strength $\approx 471\text{ MPa} /$ Compressive strength $\approx 371\text{ MPa}$.

Strain to failure \approx 1.05% (in tension) 0.86% (in compression).

Fibre failure strain \approx 1.7%.

The matrix material is extremely expensive and the amount of material for testing was very limited. The composite exists only as a quasi-isotropic woven laminate and therefore properties of unidirectional composite that would be useful for modelling are not available.

The 8-harness satin meso-architecture allows approximating in theoretical analysis the composite as a laminate with “layers” of certain bundle orientation. The thickness of the laminate is 2.9mm which means that average thickness of one “layer” (bundle) is approximately 0.18 mm. The bundle width is about 1.5mm.

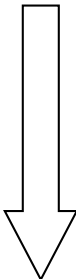
3.2. Experimental procedures

Two groups of specimens were cut from each plate (see **Table III-1**). The first group (75mmx8mm) was divided into two subgroups and subjected to two different thermal cycling loading sequences. The first subgroup was subjected to ramp (R1) between -60°C and room temperature (RT) whereas the second subgroup to ramp (R2) between -60°C and 288°C. The specimens were exposed to each temperature for 10 minutes and were subjected to up to 150 cycles. The fatigue behaviour was characterised by determining the micro-crack density in a layer by means of optical microscopy.

The specimens (150mmx12mm) of the second part of the plate with letter “A” in the label were subjected to isothermal loading at 288°C for up to 960 hours (40 days) in air environment and cooled down to RT for inspection. Then, tensile tests with displacement rate 2mm/min were performed at room temperature (RT). Strains were

measured using extensometer with gauge length 50mm. After reaching pre-described strain the specimen was removed from the machine and inspected using optical microscope.

Table III-1. Specimens' labels and loading conditions

		432			433		
		Fatigue		Aging (288°)	Fatigue		Aging (288°)
		R1 (-60°-RT)	R2 (-60°-288°)		R1 (-60°-RT)	R2 (-60°-288°)	
	Edge of the plate	432-1 (0 cycles)	432-10 (0 cycles)	A-432-1 (0h,25h,7d, 14d,21d,40d)	433-9 (150 cycles)	433-18 (150 cycles)	A-433-1 (0h,25h,7d, 14d,21d,40d)
		432-2 (1 cycles)	432-11 (1 cycles)	A-432-2 (0h,25h,7d, 14d,21d,40d)	433-8 (100 cycles)	433-17 (100 cycles)	A-433-2 (0h,25h,7d, 14d,21d,40d)
		432-3 (3 cycles)	432-12 (3 cycles)	A-432-3 (0h)	433-7 (50 cycles)	433-16 (50 cycles)	A-433-3 (0h)
		432-4 (5 cycles)	432-13 (5 cycles)	A-432-4 (0h,25h,7d, 14d,21d,40d)	433-6 (20 cycles)	433-15 (20 cycles)	A-433-4 (0h,25h,7d, 14d,21d,40d)
		432-5 (10 cycles)	432-14 (10 cycles)	A-432-5 (0h)	433-5 (10 cycles)	433-14 (10 cycles)	A-433-5 (0h)
		432-6 (20 cycles)	432-15 (20 cycles)	A-432-6 (0h,25h,7d, 14d,21d,40d)	433-4 (5 cycles)	433-13 (5 cycles)	A-433-6 (0h,25h,7d, 14d,21d,40d)
		432-7 (50 cycles)	432-16 (50 cycles)	A-432-7 (0h,25h, +10min at -60°)	433-3 (3 cycles)	433-12 (3 cycles)	A-433-7 (0h,25h, +10min at -60°)
		432-8 (100 cycles)	432-17 (100 cycles)	A-432-8 (0h,25h, +10min at -60°)	433-2 (1 cycles)	433-11 (1 cycles)	A-433-8 (0h,25h, +10min at -60°)
		432-9 (150 cycles)	432-18 (150 cycles)		433-1 (0 cycles)	433-10 (0 cycles)	
	Middle of the plate						

Fine polishing was performed after cutting using the following sequence of sand papers (P240, P600, P1200, P2500, P4000) followed by polishing using liquid diamond slurry (from 9 micron to 0.25 micron). After certain number of cycles (number in parenthesis in **Table III-1**) or certain number of aging hours (for specimens with label "A" in **Table III-1**), or after certain applied strain level for not aged ("NA") and aged ("A") specimens, the respective number of cracks N_i over distance L (53mm) on the specimen's edge was counted at room temperature in each layer separately. The crack density in each layer was calculated as

$$\rho_i = \frac{N_i}{L \sin \theta} \quad \text{(III-1)}$$

where θ is the fiber orientation angle in the layer.

The mesostructure and the damage state of all the specimens were analysed under microscope before any treatment. Some examples are presented in **Figure III-1**. The main difference between both plates is in void content. The void content was measured using image analysis software (NIS-elements BR) together with optical microscope. The void content was defined as the area fraction of voids from the observed surface.

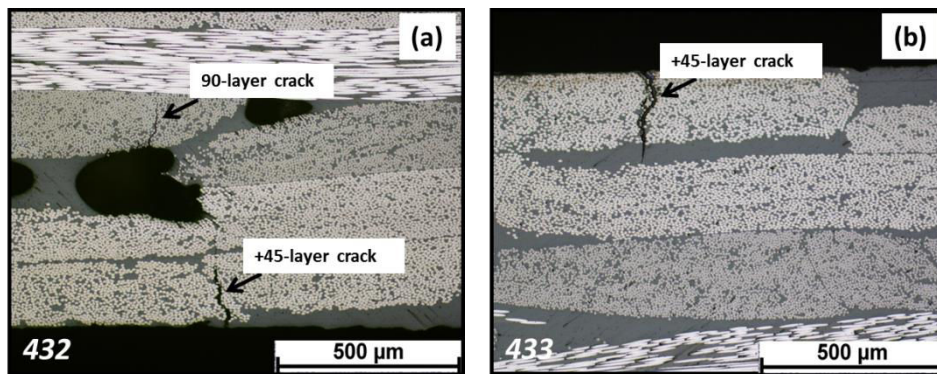


Figure III-1. Cracks caused by the residual stresses: a) plate 432; b) plate 433

4. Results and discussions

4.1. Void content and initial damage state

Due to unknown chemical shrinkage stresses and thermal residual stresses arising when cooling down the composite after manufacturing, cracks, with different densities, appear in bundles, see **Figures III-1 and III-2**. The highest initial thermal stresses are obtained when the plates were gently cooled down to 0°C directly after manufacturing. We assume that the temperature difference causing the damage state after manufacturing is approximately $0-340 = -340^{\circ}\text{C}$. The stress state in the bulk part of the composite plate can be calculated using the Classical Laminate Theory (CLT). According to CLT, in a quasi-isotropic laminate the thermal transverse stresses in all

layers are equal and the in-plane shear stress is zero. Since these two stress components are responsible for intralaminar cracking, we can say that conditions for initiation of intralaminar cracks in all layers are the same. Due to statistical distribution of failure properties in a layer the number of initiated cracks is limited but statistically it should be the same in all layers.

Cutting specimens from the plate was performed at room temperature (RT) which is about 22°C higher than the lowest temperature during the manufacturing cycle. This means that at RT the thermal stresses in the plate were lower by about 6-7 %. New cracks were not introduced during the cutting, especially because after cutting, about 1 mm from each edge was removed by polishing. Still, the first observation from **Figure III-2** is that the crack density in different layers is quite different. The surface +45-layers have much higher crack density than the rest of layers; in the 90-layers the crack density is larger than in the ±45-layers, where it is practically negligible.

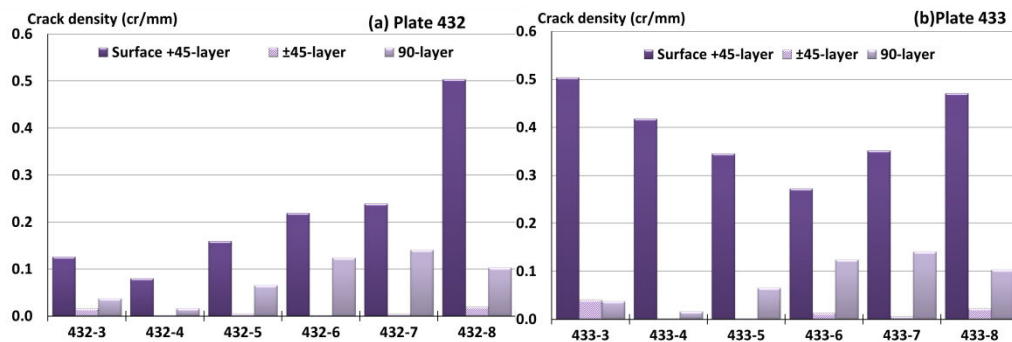


Figure III-2. Crack density on the edge of “untreated” specimens: **a)** plate 432; **b)** plate 433. Direction from left to right is towards the middle of the plate

To explain these observations, 3-D Finite Element (FE) thermal stress analysis was performed to study edge effects in a specimen with finite width. The upper part of the laminate with $[(+45/-45)/(90/0)]_{2s}$ configuration was modelled assuming that the

bundle meso-structure can be homogenized in this evaluation which is more of a qualitative nature than a quantitative characterization of stresses. The assumed thermo-elastic constants of the UD composite are: $E_1=141.025\text{GPa}$, $E_2=8.821\text{GPa}$, $\nu_{12}=0.265$, $\nu_{23}=0.442$, $G_{12}=3.62\text{GPa}$, $G_{23}=3.11\text{GPa}$, $\alpha_L=0$, $\alpha_T=25e^{-6}\text{ }^\circ\text{C}^{-1}$.

The total number of SOLID186-type of brick elements was 33600. The simulated specimen was long in x-direction (for all edge effects from $x=0$, $x=L$ to decay in the middle of the specimen) whereas the specimen width was 4mm and thickness 3mm. These dimensions were selected to have even more interacting edge stresses than in the experimental cases where the specimen width was 7 mm for thermal cycling and 12 mm for aging.

The in-plane stress distributions normalized with the CLT transverse stress value σ_{T0} are presented in **Figure III-3**. Even for this small width specimen, the transverse stress in the middle $y = W/2$ is close to the CLT value, which means that the same plateau region will be also in the experimental specimens which are wider. It also means that the magnitude of edge effects is not disturbed by overlapping the stress perturbations from both edges. The shear stress in layers, in **Figure III-3b**, is not negligible but still significantly lower than the transverse stress. In **Figure III-3a** we observe clear differences in the edge region between transverse stresses in ± 45 -layers and in 90-layers. In 90-layers the transverse stress is magnified by approximately 20% whereas in all 45-layers it is about 30% of the CLT stress. This means that after cutting the thermal stress state in the specimen is different than in the initial plate. For 90-layers the transverse stress is about 20% higher which is much larger change than the thermal stress reduction by 6-7% when the plate was brought from 0°C to RT. This means that additional cracks were initiated in the edge regions of 90-layers. Most probably they

did not grow inside the specimen because the stress conditions there did not change after cutting. This hypothesis was not possible to check experimentally because the matrix limited amount of material available for testing. On the other hand, the transverse stress in the edge region of 45-layers is much lower than in the middle part which means that new cracks were not introduced in these layers by making specimens. The above analysis explains the difference between crack densities in 90- and 45-layers shown in **Figure III-2**. However, it does not explain the much higher crack density in the surface 45-layer which will be discussed later.

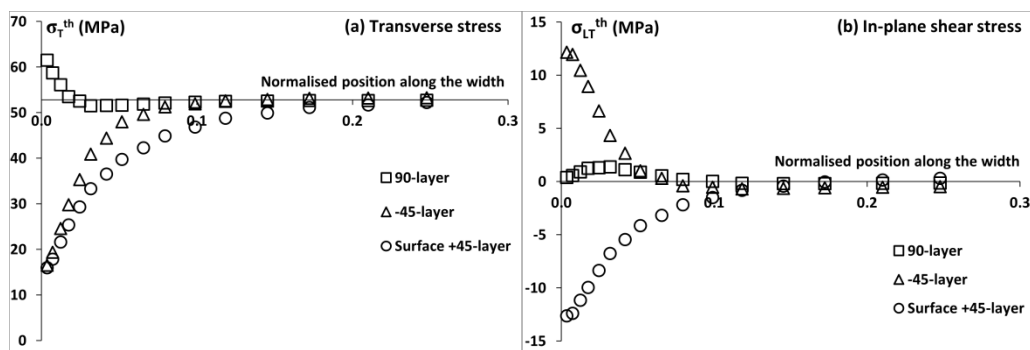


Figure III-3 Normalized thermal stress distributions in $[(+45/-45)/(90/0)]_{2s}$ laminates of finite width $W=4$ mm: **a)** transverse stress σ_T^{th} ; **b)** in-plane shear stress σ_{LT}^{th} .

Most of the 90-layer cracks in plate 432 originate from interbundle voids (see **Figure III-1a**). The average void content was measured over the area of about 100mm^2 . From one specimen to another, the average void content varied from 0.3% to 2.4% in 432. The measured void content is not too high; however, the voids were not uniformly distributed in the material. When measured in a smaller window of 1.15mm^2 ($0.93\text{mm} \times 1.24\text{mm}$), the void content varied from 0% to 13% in the plate 432. The void content in the plate 433, where diluent was used to reduce the viscosity, was almost zero.

General for both plates, it is very high variability between specimens. Therefore, at this stage solid conclusions regarding the relationship between performance and manufacturing routines cannot be drawn and all observed trends should be treated with caution. The void content in the middle of the 432-plate, see **Figure III-4**, is much higher than at the edge. It correlates with higher crack density in specimens from the middle of this plate; see **Figure III-2a** from left to right, especially in the surface layer. In fact, the role of voids is dual: they act as stress concentrators and first cracks appear at lower thermal load, but also they lead to larger stress relaxation after the crack is created, that may delay the appearance of new cracks and arrest the growth of the existing cracks. This phenomenon was described in [64-65] showing that in mechanical fatigue the cracking starts first in layers with voids but with increasing number of cycles the difference in crack density disappears. In the 433-plate diluent was used to reduce the viscosity, the void content is very low and the micro-damage state is uniform over the plate; see **Figure III-2b**.

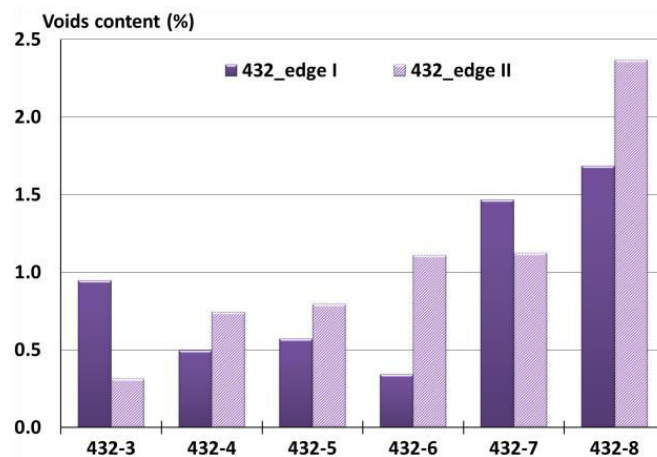


Figure III-4. Void content measured on the specimen edges.

To explain the higher crack density in the surface layers we have to distinguish two steps in crack evolution: initiation and propagation along fibres. The growth of a crack

may be described by Linear Elastic fracture mechanics (LEFM) which states that the crack will propagate when the energy release rate (ERR) G which is quadratic function of the stress reaches or exceeds the critical value (material fracture toughness G_c which in composites may be different for different growth directions and depends on the fracture mode mixity).

Intralaminar cracks initiate in stress concentration regions (voids, edges) and in weakest positions where the local fibre concentration is high and/or the fibre/matrix interface or the matrix is “imperfect” (for example, defects due to impregnation problems in high fibre content regions) characterized by certain defect state. The crack initiation process is stochastic and characterized by coalescence of fibre/matrix debonds leading to growth in the ply thickness direction. Most probably the thickness direction growth during initiation is the ply-scale thermal stress state governed, which is according to CLT is the same for all layers. However, at given thermal stress σ_{T0} the ERR for defect growth in ply thickness direction is much higher for defects of the same size at the surface than in internal layers. This fact is well known for infinite or semi-infinite plates with cracks [66]. The relationship between ERR for surface and internal crack growth in thickness direction for the same stress are given in [67]

$$\frac{G_{surface}}{G_{internal}} = (1.12 \sqrt{2})^2 \quad \text{(III-2)}$$

Thus many more cracks are initiated in the surface layer of the quasi-isotropic laminate under thermal loading. When the crack becomes sufficiently large in the ply thickness direction, propagation of the initiated crack along the fibre direction in the layer becomes energetically possible. The crack initiated at certain stress may propagate or not, dependent on the available energy for propagation at this stress level. The energy approach for crack propagation along fibres is described in [68-70]. The Mode I ERR for

the steady-state crack growth along fibres can be written in terms of crack opening displacements $u_{2an}^{(k)}$ [69-71]

$$G_I = [\sigma_{T0}]^2 \frac{t_k}{E_T} \cdot u_{2an}^{(k)} \quad \text{(III-3)}$$

In (III-3) t_k is the thickness of the damaged layer which in our case is the same for all layers, E_T is transverse modulus of the layer. The average normalized crack opening displacement $u_{2an}^{(k)}$ is different in surface and in internal layers. Expression (III-3) is valid for low crack densities when stress perturbations from cracks are not interacting which is also the case in this study. The following approximate functions for $u_{2an}^{(k)}$ were presented in [20] obtained using FE parametric analysis

$$u_{2an}^{(k)} = A + B \left(\frac{E_T}{E_x^S} \right)^n \quad \text{(III-4)}$$

For cracks in surface layer

$$n = -0.52292 \left(\frac{t_k}{t_s} \right)^2 + 0.8874 \frac{t_k}{t_s} + 0.2576 \quad \text{(III-5)}$$

$$A = 1.2 \quad B = 0.5942 + 0.1901 \left(2 \frac{t_k}{t_s} - 1 \right) \quad \text{(III-6)}$$

For cracks in internal layer

$$A = 0.52 \quad B = 0.3075 + 0.1652 \left(\frac{t_k}{2t_s} - 1 \right) \quad \text{(III-7)}$$

$$n = 0.030667 \left(\frac{t_k}{2t_s} \right)^2 - 0.0626 \frac{t_k}{2t_s} + 0.7037 \quad \text{(III-8)}$$

In (III-4)-(III-8) t_s is thickness of the adjacent layer (in our case all layers have the same thickness, $t_s = t_k$) and $E_x^S = E_L$ is the modulus of the adjacent layer in the T-direction of the cracked layer. Using the same elastic constants for CF UD composite as in FE modelling we obtain

$$\frac{u_{2an}^{surface}}{u_{2an}^{internal}} = 2.42 \quad \text{(III-9)}$$

According to **(III-3)** the energy release rate (ERR) is 2.42 times larger in the surface layer and according to the ERR based crack propagation criterion the propagation of initiated crack in the surface layer would start at much lower thermal stresses. Summarizing the above discussion we can state that in thermal loading: a) the number of initiated cracks in surface layer is much higher; b) the number of propagating cracks in the surface layer is much higher.

4.2. Damage state at RT in thermally cycled composites

After certain number of cycles of thermal loading, one specimen was saved and the number of cracks in this specimen was counted along 53mm on both edges. Each data point for crack density in **Figure III-5** is the average on two edges of one specimen. First, the damage state resulting from two different thermal loading ramps can be compared. For all layer orientations the R2 (-60°C to 288°C) ramp induced more damage than R1 (-60°C to RT). One can think that the upper temperature in R2 (288°C) is close to the stress free temperature, so less damage could be expected. However, data reveal that the interval between the minimum and maximum temperature, $\Delta T = T_{min} - T_{max}$ at fixed T_{min} has important effect on the cracking in thermal fatigue. It is consistent with the Paris law for growth of individual crack in cyclic loading, stating that the crack growth rate is a power function of the ERR difference

$$\frac{da}{dN} = A\Delta G^\beta \quad \Delta G = G(T_{min}) - G(T_{max}) \quad \text{(III-10)}$$

This relationship for intralaminar cracks was validated in **[72]** studying individual crack propagation in cross-ply tubes during mixed axial and torsional fatigue loading.

Parameters A and β in **(III-10)** are expected to be material system dependent and, hence, different for plates 432 and 433. This is clearly seen in **Figure III-5** comparing

data in different layers for plate 432 and 433 in R2 ramp. ΔG is larger for R2 ramp than for R1 ramp (larger range of stress change between max and min temperature). Even if there is not enough data for quantitative parameter determination it is obvious that for plate 432 parameter β is larger: larger difference between crack density development in R2 and in R1.

According to (III-10) in each ramp the average crack length which is proportional to the observed crack density grows linearly with the number of cycles. This trend can be seen in Figure III-5 for cracks in internal layers but the relationship seems to be different for cracking in the surface +45-layer. The crack density is also much higher in surface layers.

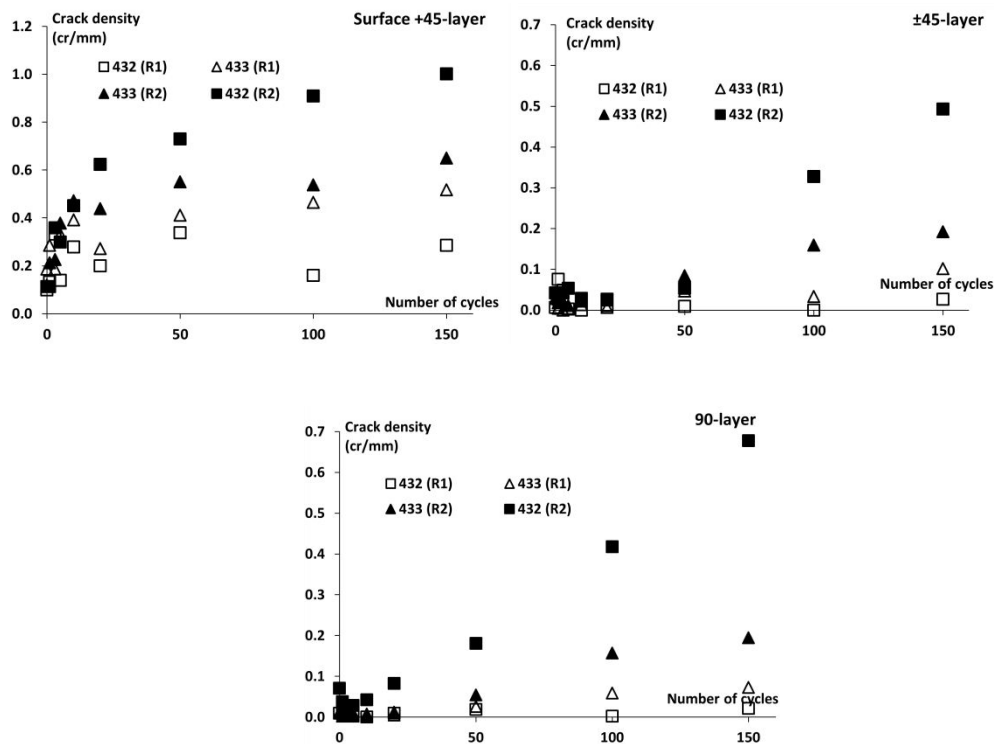


Figure III-5. Edge crack density growth in two thermal fatigue ramps (R1 (-60; RT)°C; R2 (-60;+288)°C for plate 432 and plate 433

Much larger crack density in surface layers was observed also in [73] where thermal cycling at cryogenic temperatures was performed. In [73] the crack density determined on the edge of 90-layer was also higher than in internal 45-layers.

To explain these two features we have to recall that even in fatigue there is an initiation phase and propagation phase. Certain number of cycles N_{init} is required to initiate crack and a different number of cycles N_{prop} is required for its propagation along fibres to cover the whole width of the specimen. If $N_{prop} \gg N_{init}$ the “fatigue life” (number of cycles for full development of the crack) is propagation governed, in contrary, if $N_{init} \gg N_{prop}$ the cracking in fatigue is initiation governed. In surface layer, the ERR for crack growth along fibres is much higher than in internal layers and crack propagation is almost instant (initiated cracks instantly grow through the specimen). The initiation is a stochastic process with a certain probability. In [72,74] modification of the Weibull model was suggested and supported by experiments for density of initiated cracks in mechanical tensile cyclic loading. After adjustment of notation to our aims it is as follows

$$\frac{\rho_k(\sigma_T, N)}{\rho_{k,max}} = 1 - \exp \left[-kN^\alpha \left(\frac{\sigma_T}{\sigma_{ino}} \right)^m \right] \quad \text{(III-11)}$$

The number of initiated cracks depends on parameter k which due to higher significance of surface defects is larger for surface layers. The shape of the dependence on the number of cycles in (III-11) is similar to the stress dependence of probability of failure in the Weibull distribution: S-shape with three regions. At certain stress, in the Region 1 of the cyclic loading (small N) cracks are initiated only in a few weakest positions. Later on with increasing N (Region 2) the crack density is increasing faster because many positions have similar resistance to crack initiation. When the cyclic

loading is continued a fewer number of new cracks are initiated because there are not so many positions in the layer left with high fatigue resistance (Region 3). In result the crack density growth rate slows down. In the performed thermal cycling test thermal stresses are high and rather high crack density formed in the surface 45-layer already in the last stage of the manufacturing. This means that for this layer the fatigue cracking starts in Region 2 and slows down when it reaches Region 3.

Comparing both plates, see **Figure III-5**, in the R2 ramp the plate 433 is thermally more resistant. During ramp R1 the damage development in both plates is rather similar; the number of cracks is much smaller. However, ranking regarding the fatigue resistance is not possible due to the large scatter. The internal +45- and -45-layers show the same cracking behaviour, thus, they are considered together and the average crack density of all 45-layers is given in **Figure III-5b** (counting cracks on both edges of the specimen). Validity of this procedure is demonstrated in **Figure III-6** which shows crack density in all layers on the edge of one 432 specimen after 150 cycles in ramp R2. It appears that internal 45-layers have slightly lower amount of cracks than in 90-layers after 150 cycles. In [73] the thermal fatigue caused crack density, determined on the edge, was also higher in 90-layer than in internal 45-layers.

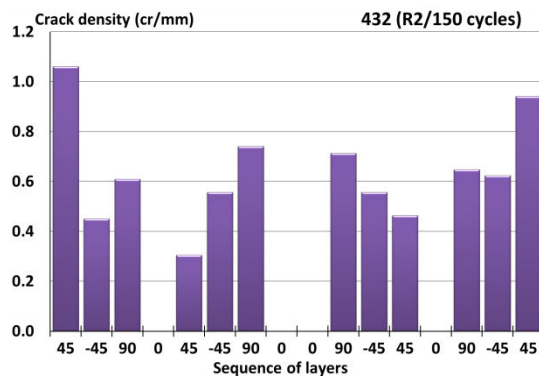


Figure III-6. Crack density distribution in the layers along thickness on the edge of specimen 432-18. (Cracks in 0_layers were not counted).

Since the crack counting was on specimen edge the result is consistent with the transverse stress distribution in **Figure III-3**: in 45-layers stress in the edge region is lower and in 90-layers higher than in the bulk of the specimen. In 45-layer case, not all cracks reached the edge and in 90-layer case some edge cracks did not propagate inside the layer.

To investigate whether the edge cracks propagate inside the specimen and vice versa the edge of specimen 432-18 subjected to 150 cycles with R2 was polished to quantify the damage state at distance d from the specimen edge ($d=0.9\text{mm}$ and then $d=2.4\text{mm}$). The results presented in (**Figure III-7**) confirm expectations: a) the crack density inside the specimen is approximately the same in the 90- and internal 45-layers; b) the crack density inside the internal 45-layers is higher than at edges; c) the crack density on the edge of surface 45-layer is similar as inside which proves that in the surface layer there is an excess of ERR for propagation in fibre direction and therefore, in contrast to internal 45-layers, almost all cracks reach the edge. We do not see any reason for lower crack density on the edge of the 90-layer and we believe that the variation shown for this layer in **Figure III-7** is a measure of scatter.

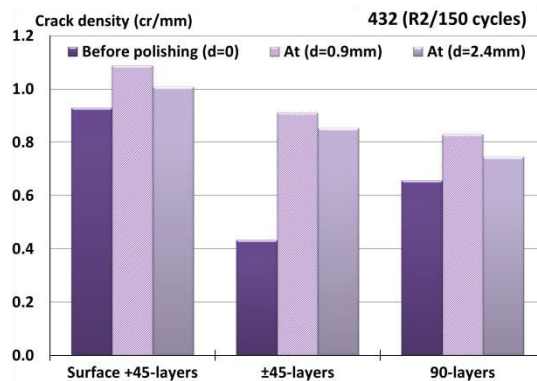


Figure III-7. Cracks density dependence on the edge distance for thermally cycled specimen after 150 cycles in R2

The analysis given in this section is based on LEFM. In fact, it is not certain that in ramps with high upper temperature parameters A and n remain constant. More irreversible effects including aging can be expected at +288C which may lead to accelerated crack propagation when the lowest temperature is reached in the next cycle. Temperature gradients during the cooling down part of the cycle can lead to additional damage in surface layers.

4.3. Damage state at RT in aged composites

Specimens were exposed to 288°C in ambient air environment for certain amount of hours and cooled down to RT to count cracks on specimen edges. If the time at high temperature would affect the composite transverse failure properties (aging), thermal stresses at RT would introduce additional cracks. The crack density versus the number of aging hours is presented in (**Figure III-8**), two specimens from each plate were tested.

The counting was performed 24 hours after removing specimens from the oven. The crack density was not high enough to have significant effects of crack interaction on evolution. In a not aged specimen the surface +45-layers have the highest initial crack density (**Figure III-2**) which increases linearly with the aging time reaching at the end of the test approximately 1cr/mm. The crack density on the edge of the 90-layer is increasing with a higher rate comparing to the surface +45-layer reaching about 1.7cr/mm at the end of the test. The crack density in the internal ± 45 -layers starts to increase later, after around 400 hours of aging time and the cracking process is

accelerating. Comparing the aging effect on crack development in both materials (plate 432 and plate 433) we cannot observe any clear difference in the behaviour.

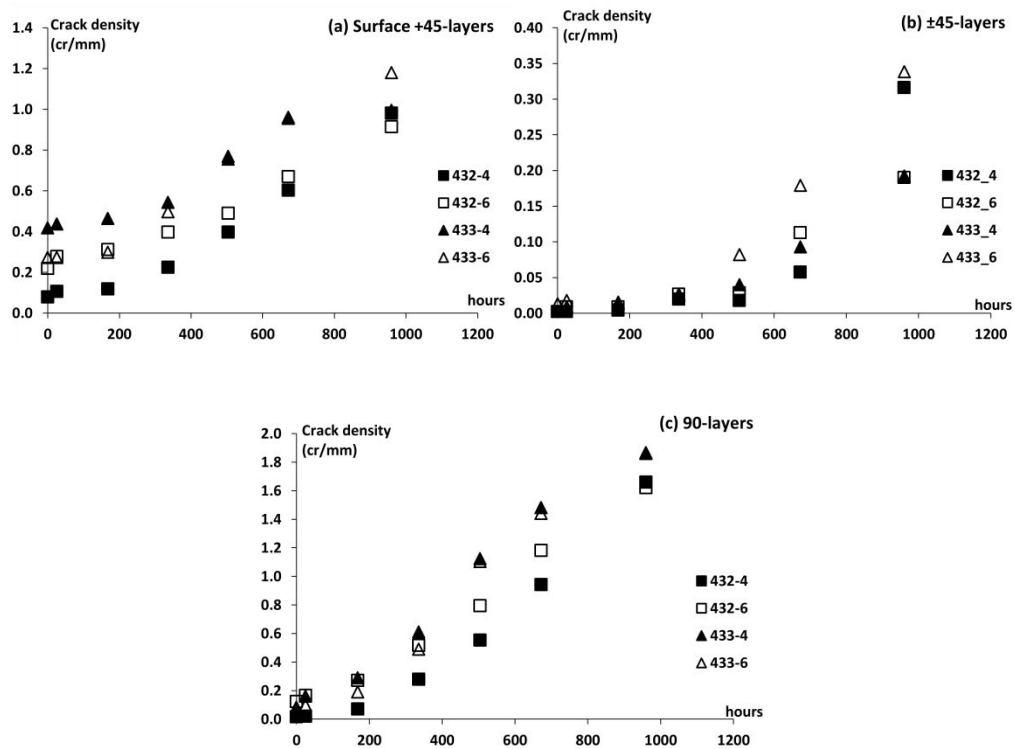


Figure III-8. Crack density on the specimen edge versus aging time: **a)** surface 45-layers; **b)** internal 45-layers; **c)** 90-layers

To establish whether the edge data are representative for the bulk of the composite, edge polishing of one 40 days aged specimen (433_2) was performed similarly as it was done for a thermally cycled specimen (see **Figure III-9**). The results show that the damage state is very different than on the edge: in the 90-layer cracks are abundant only on the edge. The amount of cracks in the 90-layer away from edges is very similar to the number of cracks found on the edge of the same specimen before aging (originating from residual thermal stresses after manufacturing). It indicates that in the bulk of the 90-layer the material aging due to high temperature exposure for 40 days is

rather small: most of the cracks initiated on the aged edge do not propagate inside the layer.

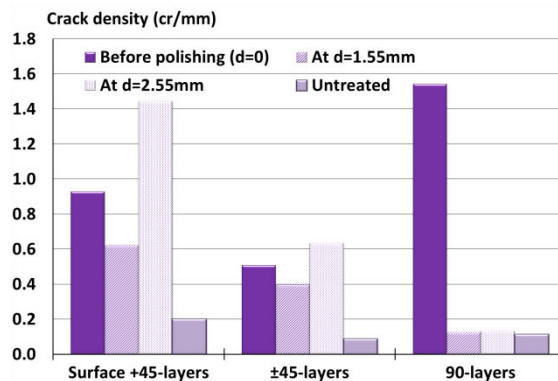


Figure III-9. Crack density inside a 40days aged specimen (A-433-2).

The crack density in the internal 45-layers on the aged edge is much lower than in the 90-layers on edge. This has a simple explanation based on the stress distributions in **Figure III-3**: even if the material on the specimen edge is significantly degraded, transverse stress in the 45-layers in this region is much lower than in 90-layers. The lower stress at the edge means that the middle part of the layer is still responsible for crack propagation and, since the aging has not affected this part significantly, the crack density does not change with the distance from the edge.

During the aging test the surface 45-layers are subjected to contact with the high temperature environment not only in the edge region but also over the whole surface. Therefore more uniform material degradation can be expected in the layer leading to overall decrease in resistance to crack initiation and propagation. The stresses at the edge of surface layers after aging are as low as the stresses on the edge of the internal 45-layers but the available energy conditions are more favourable for a crack to reach the edge. Since the crack density on the edge of the surface layer is result of

propagation from the inside of the layer, the crack density is lower than at the edge of 90-layers where the stress is magnified and where the initiation takes place.

The phenomenon of the aged zone propagating from the specimen surface explains also the peculiar data in **Figure III-9** with the crack density in internal 45-layers apart from edges being in average several times higher than in 90-layers (the propagation conditions are similar for both types of layers). More detailed analysis reveals that the crack density in internal 45-layer is a function of the distance of this layer from the laminate surface. The crack density in the layer next to surface layer is much higher than in 45-layers close to the symmetry plane of the laminate where the crack density is very similar as in 90-layers. This means that not only the surface layer but also the next layer has aged, which is expected because the thickness of one layer (0.18mm) is much smaller than the size of the observed aged zone at the edge (about 1 mm), even if the oxygen diffusion rate could be higher in fibre direction.

The long exposure to high temperature in a direct contact with oxidative atmosphere generally leads to weight loss. An average of weight loss taken over 4 specimens from each plate is plotted versus the aging hours in **Figure III-10**. The weight loss did not exceed 1.4% after 40 days of aging at 288°C.

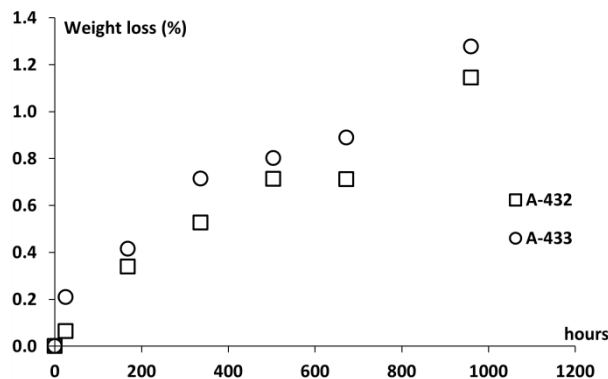


Figure III-10. Weight loss due to aging at 288°C

The degrading effect of the contact with high temperature air is illustrated in **Figure III-11** where the same position on the specimen edge is shown at RT before and after aging for 40 days. The colour of the surface has changed and the surface is rough (reminds calk) as if part of the resin material has fallen out especially from places with resin pockets or pre-existing cracks. Some additional cracks seen on the right are result of cooling down the specimen to RT after the aging test.

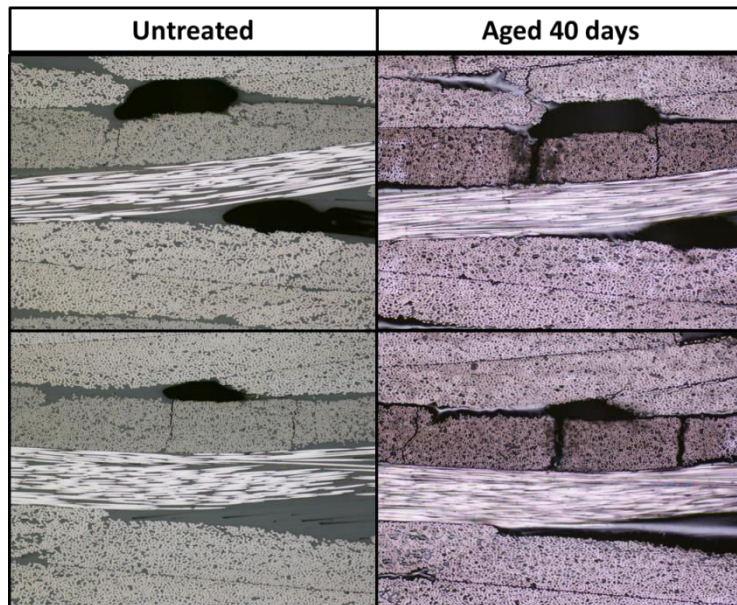


Figure III-11. Edge view of 432-6 specimen before and after 40 days of aging

However, after edge polishing during the procedure to get data for **Figure III-9**, the surface looks like the edge of an untreated specimen. It appears that only about 1mm thick boundary layer at the edge of the specimen was oxidised and much longer time is needed to degrade the whole specimen (It was decided to remove this aged layer by polishing before tensile testing was performed to inspect for possible degradation in the bulk of the composite). These results are consistent with the after aging cracking data presented in this section. The results provide evidence that this composite may

be a good candidate for high temperature applications provided that the free surfaces are not in a direct contact with the air.

Now when the thermal aging effect on cracking is described we have to address again the thermal fatigue results for ramp R2. During the thermal cycling test specimens were subjected for in total about 25h at 288°C (10 minutes in each cycle and for 150 cycles). Hence in the thermal cyclic loading, two effects could contribute to the damage development in the composite: the effect of possible fatigue during cycling and the effect of thermal aging due to the 25h at high temperature. To investigate the effect of aging two specimens were kept at 288°C during 25h. It was found (**Figure III-12**) that the specimens aged for 25h after cooling down to -60°C have fewer cracks than the specimens subjected to R2 cyclic loading, which confirms that only a part of the cracking in the thermal cycling test is due to aging.

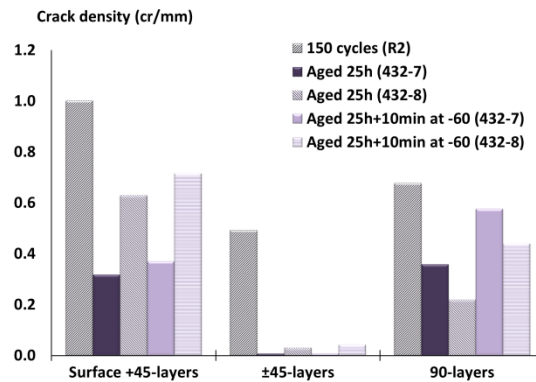


Figure III-12. Aging and thermal cycling effects on edge crack density

4.4. Damage state in mechanically loaded composites

As mentioned in the previous section the edge zone of aged specimens was severally damaged and it was removed by polishing before the stepwise mechanical testing started. The effect of aging on cracking resistance was still expected to be different in

surface and in internal layers. Mechanical loading introduced more cracks and also delaminations between layers. Due to limited amount of specimens, sectioning of the specimen before the final test step (the highest strain level) was not possible, and the multiple cracking results presented in following sections are based on edge observations only.

From other side, cracks approaching the edge from the inside can be stopped due to the lower stress in the edge region, thus, not reaching the edge. Even for undamaged laminate the stress state at the edge is 3-D and the features of stress concentrations are different in different layers. The edge effects in thermal and uniaxial mechanical loading are different and the summary effect is a linear superposition of the two, where the thermal part remains unchanged whereas the mechanical part grows linearly with the applied strain. The possible problems with edge observations and also the possible effects of edge stresses on damage initiation were estimated analysing stress distributions and also comparing the damage states experimentally.

The simulated specimen was long in x-direction to have a region with x-independent stress state. The specimen width was varied between 4mm and 30 mm whereas the laminate thickness was 3mm. These dimensions were selected to have isolated effects from both edges as well as interactive ones.

According to CLT transverse thermal stress, σ_T^{th} for the assumed properties and $\Delta T = 288 - 25 = 263$ is 53 MPa. The CLT σ_T^{th} is the same for all layers in a quasi-isotropic laminate and the CLT thermal shear stress $\sigma_{LT}^{th} = 0$. The in-plane thermal stress distributions at the edge are presented in **Figure III-3**.

Whereas thermal stresses are not changing during the tensile test, the mechanical stress is proportional to the applied strain. In **Figure III-13** the mechanical transverse, σ_T^m and in-plane shear stress σ_{LT}^m distributions in layers are shown for applied strain $\varepsilon = 1\%$.

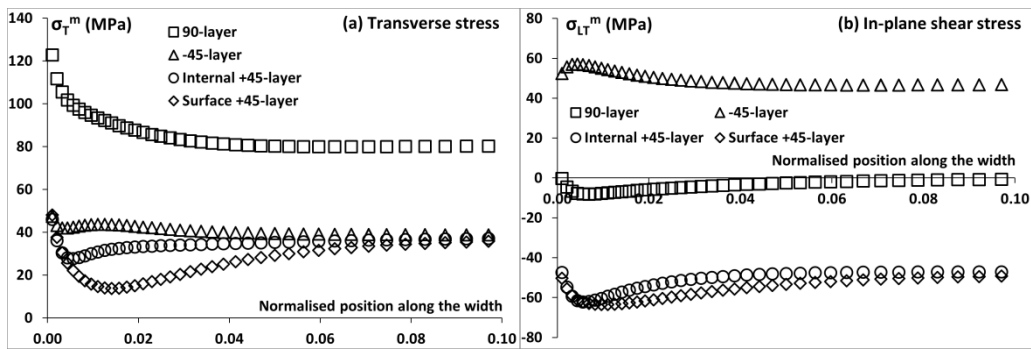


Figure III-13 Mechanical stress distributions in $[(+45/-45)/(90/0)]_{2s}$ laminates of finite width $W=30\text{mm}$: **a)** transverse stress σ_T^m ; **b)** in-plane shear stress σ_{LT}^m .

At 1% strain the total transverse stress in the 45-layer is $\sigma_T^{45} > 53 + 40 = 93 \text{ MPa}$ whereas the shear stress $\sigma_{LT}^{45} \approx 0 + 40 = 40 \text{ MPa}$, ($\frac{40}{93} \approx 45\%$). At lower loads the fraction of the shear stress is even lower. For this reason, analysing failure in follows we will neglect the shear stress contribution assuming that crack initiation is by transverse stresses. Comparing predictions with data we will show the applicability of this assumption.

The mechanical transverse stress σ_T^m at the edge has the following features:

- In 90-layers it is magnified by 50% comparing to the CLT value. However the stress concentration zone is very small (1mm).
- In the internal +45-layers it is by 30% lower than in the CLT zone. In the surface layer the reduction is 60%

- In the -45-layers there is a magnification about 10%.

The in-plane shear stress σ_{LT}^m in all 45-layers is magnified in the edge region by 20 to 40%. Superposing the mechanical and thermal edge effects we can conclude that there is transverse stress magnification in 90-layer but not in 45-layers. The shear stress is magnified at the edge of 45-layers which may “compensate” for the lower transverse stress in this region leading to rather uniform conditions for damage initiation in these layers. In terms of crack density there is a risk that in 90-layers more cracks are in the edge zone because of higher transverse stress making edge observations unreliable. In 45-layers the crack density on the edge may be more representative. However, edge delaminations linking cracks are increasing the significance of each crack in stress reduction and lowering the probability of new cracks initiating between two existing cracks, thus, working against the edge effect in stress distribution in 90-layers.

These questions were resolved experimentally comparing damage statistics on the edge with the damage state quantified (after polishing) at several distances from the edge. In this inspection one NA specimen after loading to 1% strain and one aged (A) specimen after loading to 0.7% strain were used. **Figure III-14** shows crack density in different layers as a function on the distance from edge. There is no statistically confirmed trend with more cracks on the edge of the specimen. This conclusion holds for NA as well as for A specimens.

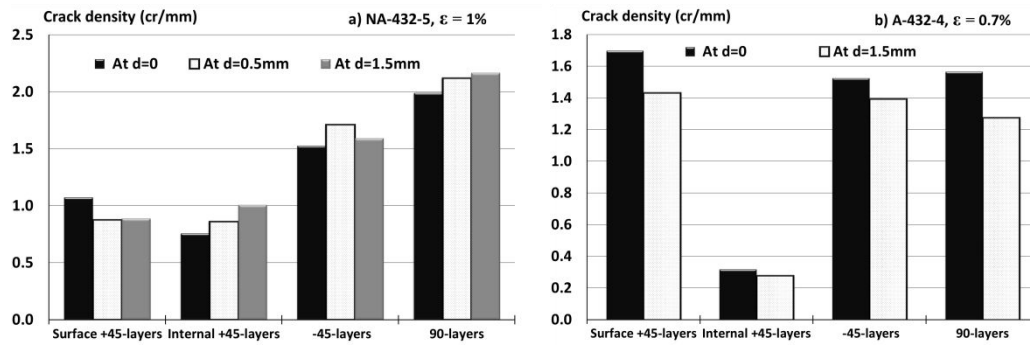


Figure III-14 Crack density versus distance d from edge: **a)** NA-432, $\varepsilon=1\%$, **b)** A-432, $\varepsilon=0.7\%$.

The delamination length normalized with the interface length is shown in **Table III-2** for each interface in a NA specimen after loading to 1% strain. At the edge the normalized delaminations are larger (more than 20%) at interfaces closer to the laminate surface. However, already at $d = 0.5mm$ from the edge the delaminations are much smaller and they practically disappear at $d = 1.5mm$.

Table III-2 Normalized delamination length

		Normalized delamination length (%)		
		Before polishing	Polishing $d=0.5mm$	Polishing $d=1.5mm$
	Interface			
Top	I: surface+45/-45	27.4	0.0	0.0
	I: -45/90	21.3	5.4	0.0
	I: 90/0	13.3	1.2	0.0
	I: 0/+45	0.5	0.0	0.0
	I: +45/-45	15.3	1.5	0.0
	I: -45/90	9.0	1.3	1.0
	I: 90/0	1.6	0.5	0.0
	I: 0/90	2.1	1.5	0.5
	I:90/-45	5.0	4.3	0.4
	I: -45/+45	13.3	5.0	0.0
	I:+45/0	0.0	1.0	1.2
	I: 0/90	9.3	9.5	0.0
	I: 90/-45	24.7	12.4	0.5
Bottom	I:-45/surface +45	14.8	14.8	1.0

The uniform crack density in **Figure III-14** means that most of the initiated cracks had enough of ERR to propagate along the fibre direction. The hypothesis is that the 45-cracks initiated in the bulk part could reach the edge and the 90-cracks initiated at the edge could propagate through the bulk of the layer. However, at the edge of the 90-layer we have stress concentrations but also edge delaminations relaxing stresses. Based on the data presented in this section we cannot resolve whether they are self-compensating or not and whether the edge is or is not the initiation region for most of the cracks in the 90-layer. Further information on this subject will be given later where Weibull analysis will be applied to 90-cracks and the results used to predict multiple cracking in 45-layers.

Nevertheless, the presented results give sufficient confidence in ability of edge observations to represent the damage state and in the analysis presented in next section.

4.5. Damage accumulation analysis

Measurements show that the growth of crack density is different in different layers. We will first analyse the damage evolution in 90- and +45-layers comparing both composites before and after aging. Then we will analyse the behaviour of -45-layers which is rather different than the behaviour of +45 layers. But, we will start by presenting the theories that will be used in the analysis.

4.5.1. Theoretical background

Analysing multiple intralaminar cracking in laminates we have to distinguish two steps in evolution of each individual crack: initiation (growth mostly in ply thickness

direction) and propagation along fibres in the layer. Some of the equations mentioned in **section 4.1** are reused in this section in addition to others to explain the damage accumulation. The concept will be re-explained from the beginning to make a complete story. Utilizing Linear Elastic Fracture Mechanics (LEFM) concept, the crack will grow when the energy release rate (ERR) G which is a quadratic function of stress, reaches or exceeds the critical value called fracture toughness G_C . In composites the fracture toughness is different for different growth directions and depends on the fracture Mode mix. Since mechanisms in shear and transverse tensile failure are similar, we may expect that in a layer with θ -orientation shear stress, σ_{LT}^θ will facilitate cracking caused by transverse stress σ_T^θ ; however, the role of tensile σ_T^θ is dominant. The stress state is a superposition of thermal stresses (zero shear stress in quasi-isotropic laminates) and mechanical stresses. Unfortunately reliable mixed mode criteria are not available and are difficult to establish experimentally. Therefore, in cases when the shear stress is several times smaller than the transverse stress, as it is in this paper, only Mode I is often considered, keeping in mind that adding Mode II would increase the number of cracks.

According to LEFM growth conditions for a crack (notch) with a length a are entirely different for a crack in the middle of an infinite plate and at the edge of a semi-infinite plate [66]: the critical stress level for growth is much lower for edge crack. The relationship between ERR for edge crack and internal crack growth at given stress is

$$\frac{G_{surface}}{G_{internal}} = (1.12 \sqrt{2})^2 \quad \text{(III-12)}$$

In internal layer of a laminate the surface defect growth is suppressed by constraint from the adjacent layers and most probably defects from the middle of the layer will

develop a crack. Therefore, for defect of a given size and at given stress σ_T^θ the ERR for its growth in ply thickness direction is higher for defect on the free surface of the surface layer than for the defect in internal layers. After reaching certain size the crack growth becomes unstable and then slows down close to the interface with the next layer finally being arrested there [75-76]. In [67] relationship (III-12) was used for analysis of cracking in surface and internal layers of laminates resulting in the follows relationship between crack initiation stress in internal and surface layers of the same orientation

$$\sigma_{Tinit}^{internal} = k\sigma_{Tinit}^{surface} \quad \text{(III-13)}$$

where

$$k = 1.12\sqrt{2} \quad \text{(III-14)}$$

Intralaminar cracks initiate in stress concentration regions (local fibre clustering, voids, edges) and in weakest positions where the fibre/matrix interface or the matrix is “imperfect” (for example, defects due to impregnation problems in high fibre content regions). The crack initiation process is characterized by coalescence of fibre/matrix debonds leading to formation of a crack which grows in the ply thickness direction. It would be convenient to express the thickness direction growth criterion during initiation in terms of ply- scale stress state calculated using Classical Laminate theory (CLT) and the factor k to reflect the difference between surface and internal layers.

The initiation of a crack is a stochastic process with certain probability and with random position if the stress distribution is uniform along the layer. This is because the weakest position for the crack to come is related to local inhomogeneity with random location. The local fibre clusters of size of 3-5 fibre diameters ($l_0 \approx 0.05mm$) define

the critical size when the coalescence of defects may be considered as an unstable crack. In simulations of crack initiation we assume that any layer in its transverse direction can be considered as consisting of a chain of elements of this size. The elements all-together follow the two-parameter Weibull strength distribution,

$$P_f = 1 - \exp \left[- \left(\frac{k\sigma_T}{\sigma_{in0}} \right)^m \right] \quad \text{(III-15)}$$

but the location of an element with certain strength is random. According to (III-13) a larger amount of cracks is initiated in the surface layer of the quasi-isotropic laminate than in internal layer of the same orientation. Parameter k is introduced in (III-15) to reflect the favourable situation for crack initiation in the surface layer of the laminate.

Performing Monte-Carlo simulation we randomly select, for example, $N = 2000$ elements from a virtually infinite pool of elements to create a specimen of length $L_0 = N \cdot l_0 = 100mm$. This selection does not exactly represent the initial Weibull distribution which means that each selection is a new specimen of the same material. The selected specimen has certain transverse strength distribution along the transverse direction of the layer. The first crack will appear in the element with the lowest strength. After that, for any fixed damage state with given spatial distribution of cracks, the stress distribution is calculated using some model (shear lag, Hashin's etc) and failure index (stress versus strength) is calculated in each element to find the position of the next crack. This procedure seems rather complex but in this way the interaction between cracks which weakens the stress field and delays cracking is accounted for.

If the crack density in an i^{th} layer is low enough to allow for large plateau regions in stress distribution between cracks, the probability of failure as a function of transverse stress can be estimated using expression

$$P_f = \frac{\rho_i(\sigma_T)}{\rho_{i,max}} \quad \text{(III-16)}$$

In **(16)** $\rho_{i,max}$ is the maximum possible crack density in a layer corresponding to the so called “characteristic damage state”. Based on experimental observations $\rho_{i,max} \approx 1/t_i$ where t_i is the thickness of the layer. Using the experimental crack density dependence on transverse stress to calculate P_f , we plot the $\log(-\log(1 - P_f))$ versus $\log \sigma_T$ and use the standard procedure to estimate Weibull parameters. The result is rather sensitive to the used data points on both extremes: data points at high crack density are affected by crack interaction whereas the stress at first crack varies a lot from specimen to specimen, requiring large amount of specimens to be reliable. The so obtained estimates of Weibull parameters can be used in Monte-Carlo simulations over the whole crack density region and adjusted to increase the accuracy.

When the crack becomes sufficiently large in the ply thickness direction, propagation of this crack along the fibre direction in the layer may become energetically possible. The crack initiated at certain stress may propagate or not, dependent on the available energy for propagation (ERR) at this stress level. The energy approach for crack propagation along fibres is described in **[20-22]**. The Mode I ERR for the steady-state crack growth along fibres in a layer can be written in terms of crack opening displacements $u_{2an}^{(k)}$ **[21-23]**

$$G_I = [\sigma_{T0}]^2 \frac{t_i}{E_T} \cdot u_{2an}^{(i)} \quad \text{(III-17)}$$

In **(III-17)** t_i is the thickness of the damaged layer, E_T is transverse modulus of the layer. The average normalized crack opening displacement $u_{2an}^{(k)}$ is different in surface and in internal layers. Approximate expressions for $u_{2an}^{(k)}$ were presented in **[20]** based on results of FE parametric analysis. Using the same elastic constants for CF UD composite as in FE modelling in **section 4.1** we obtain

$$\frac{u_{2an}^{surface}}{u_{2an}^{internal}} \approx 2.42 \quad \text{(III-18)}$$

Hence, according to LEFM the propagation of initiated crack in the surface layer requires much lower stresses than in internal layer of the same orientation. Results show that cracks in our composite have propagated across the specimen width, which means that an initiated crack is propagating at the same stress.

Summarizing the above discussion we can expect that a) the number of initiated cracks in surface layer is much higher; b) in our composite all cracks propagate as soon as they are initiated. Therefore, focus in this analysis will be on crack initiation which we will describe by the Weibull analysis discussed above.

4.5.2. Multiple cracking in 90- and +45-layers of not aged (NA) composites

Analysing cracking in the 90-layers of the 432 NA laminate, first, the crack density dependence on transverse stress was obtained from the applied strain (using CLT) and the estimated thermal stresses. Using **(III-16)** the experimental crack density data for 90-layers was transformed to probability of failure and **(III-15)** was used to estimate Weibull parameters. The values for these parameters for both composites (aged as well as not aged) are given in **Table III-3**. The log-log relationship is shown in **Figure**

III-15a. The first point on the left corresponds to crack density due to thermal stresses with rather uncertain stress value. The last three points deviate from linearity which is a sign of crack interaction. According to **Figure III-15b**, where the test data and the simulation using **(III-16)** (solid line labelled P_f and referred as P_f -approach) are shown, deviation starts at $\rho_{90} \approx 1.6 \text{ cr/mm}$. In **Figure III-15b** Monte-Carlo simulations with the same parameters are also shown (different symbols for shear lag and Hashin's model) demonstrating noticeable deviation between the P_f -approach which ignores crack interaction and Monte-Carlo simulations accounting for it, starting at $\rho_{90} \approx 0.5 \text{ cr/mm}$ which is much lower than $\rho_{90} \approx 1.6 \text{ cr/mm}$ estimated from deviation between the P_f approach and experimental data. Of course, the result of the Monte-Carlo simulation depends on the used stress model and it is well known that Hashin's model overestimates the interaction of stress perturbations, whereas in the shear lag model case the result depends on the used modification (we used shear lag model which assumes existence of a resin rich region of thickness $d_0 = 0.02 \text{ mm}$ between layers). Nevertheless, **Figure III-15b** confirms the conclusions from [77] obtained from probabilistic consideration: a) crack interaction starts to affect results at rather low crack density; b) for non-uniformly distributed cracks interaction effects are noticeable at lower crack densities than for uniformly distributed cracks.

Returning to results of Monte-Carlo simulations in **Figure III-15** we have to conclude that the Weibull parameters obtained using **(III-16)** (P_f - approach) are rather inaccurate: the parameters in **Table III-3** give good fit to used data but they are not the real Weibull parameters.

Since the “real” parameters determined from Monte-Carlo simulations are always related to some specific approximate stress model, and the goal of this paper is rather a qualitative explanation of observed phenomena than a “quantitative perfection”, we will use, when comparing damage development in different layers, different composites as well as the effect of thermal aging, the P_f -approach because of its simplicity.

The Weibull parameters from **Table III-3** were used to predict crack density in internal +45-layers and in the surface +45-layer of the NA-432 laminate. All internal +45-layers behave in a very similar way. The data and simulations using the P_f -approach are presented in **Figure III-16** which shows good agreement proving that a) cracking in +45-layers has the same transverse stress dependence as in 90-layers, indicating that the edge effects in 90-layers discussed previously are not significant; b) at least for low loads the effect of shear stresses in cracking simulation can be neglected. At low strains the predicted crack density in +45-layers is slightly higher than the experimental which can be attributed to the “imperfect” parameter determination in 90-layer and to the discussed edge effect in 90-layer.

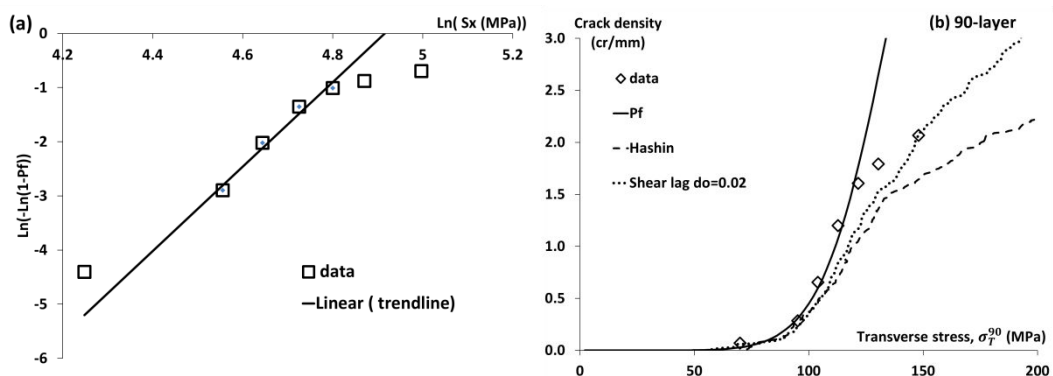


Figure III-15 Cracking in 90-layers (NA-432): **a)** Weibull plot of test data; **b)** crack density versus transverse stress σ_T^{90} , P_f -approach **(4)**; Monte-Carlo simulation using shear lag and Hashin's models

Table III-3 Weibull parameters from 90-layer cracking

Composite	m	S0 (MPa)
432-NA	7.84	135.2
433-NA	8.33	138.8
432-A	6.88	134.0
433-A	7.3	144.2

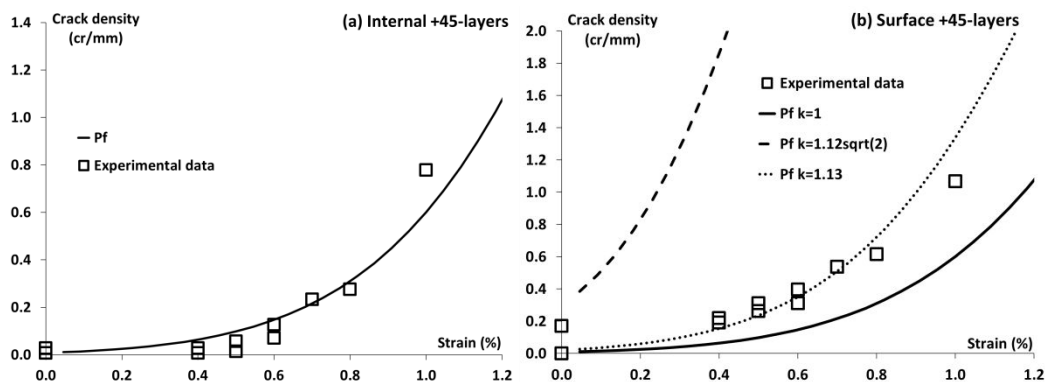


Figure III-16 Crack density growth with strain in +45-layers of NA-432 (data and predictions using Pf approach)

The crack density in the surface +45- layer, shown in **Figure III-16b** is significantly higher with many cracks existing before mechanical loading. The Pf –approach with $k = 1$ gives the same prediction as for internal +45-layers. An attempt to use in simulations equation **(III-15)** with $k = 1.12\sqrt{2}$ also failed – far too high crack density was predicted, see **Figure III-16b**. As a good fitting value $k = 1.13$ was found, but this

values is missing any fracture mechanics meaning and as shown in following it does not work for other cases.

These results show that the discussion regarding the role of the free surface on defect growth has been oversimplified. In fact, the $k = 1.12\sqrt{2}$ effect has been proven by computation micromechanics simulations for the first crack only [78]. It is incorrect to assume that in the surface layer of the laminate all cracks will initiate at the free surface: even assuming that the defect state is uniform across the layer (it is just an assumption- in reality there could be resin rich region at the surface changing the statistics) only the first cracks will originate from the largest defects close to the surface, but after that the largest remaining defects are not on the surface of the layer and sooner or later it will be their turn to grow. Thus, the multiple crack initiation in the surface layer should be a mix of cracks coming from the surface and from the interior of the layer. May be the first group of cracks could be characterized by $k = 1.12\sqrt{2}$ in (III-15) whereas the second group by $k = 1$. An indecisive support to this is given by **Figures III-16b and III-17b** where the first cracks in the surface layer are close to predictions using $k = 1.12\sqrt{2}$ whereas later it becomes closer to the $k = 1$ curve. If so, these two predictions could be used as an upper and lower bounds to the cracks density. Unfortunately, cracks interaction would have a similar effect: at high crack density cracks in surface layers are interacting much more than in internal layers.

The crack density growth with strain in 90-layers of the NA-433 plate which has slightly modified composition is shown in **Figure III-17a**. This relationship was used to estimate Weibull parameters, see **Table III-3**, using (III-15) and (III-16) as described

above for NA-432 plate. These parameters were used in the P_f -approach to predict cracking in +45-layers. The predictions, shown with solid line in **Figure III-17a**, are in a good agreement with cracking evolution in this layer.

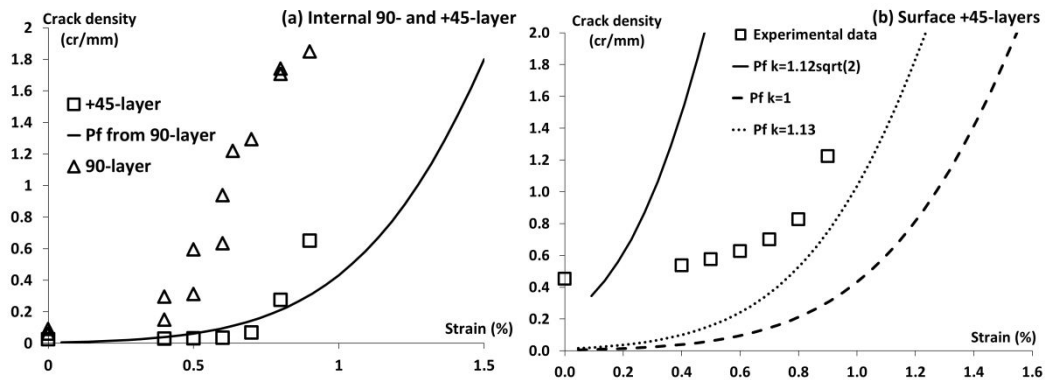


Figure III-17 Microcracking development in NA-433

Similarly as for the 432 composite, cracking in the surface +45-layer does not follow any of the discussed rules regarding. The rather trivial conclusions are: a) fitting with $k = 1.13$ is not good for this composite; b) the crack density is indeed between the bounds defined by $k = 1.12\sqrt{2}$ and $k = 1$ being closer to the former at lower crack density and tending to the latter with increasing crack density.

Comparing results for NA-432 (with voids) and NA-433 (no voids) presented in this section we do not see large differences. Even the Weibull parameters are very similar and the differences most probably are due to scatter and a different number of available data points. A real difference is in surface layers, where 433 laminate, without voids, has more cracks before mechanical loading and also during increasing mechanical loading. Indeed, the role of voids may be dual: they act as stress concentrators and first cracks appear at lower stress, but they also lead to larger stress relaxation after the crack is created and linked to the void (especially in a surface layer

where one surface is free). That may delay appearance of new cracks. This phenomenon was described in [64-65] showing that in mechanical fatigue the cracking starts first in layers with voids but with increasing number of cycles the difference in crack density diminishes.

4.5.3. Multiple cracking in 90- and +45-layers of aged (A) composites

The crack density in aged composites was analysed as described in **section 4.5.2**. First, the Weibull parameters, see **Table III-3**, were obtained from 90-layers cracking data. These parameters were used in the P_f -approach to predict crack density growth in 45-layers, see **Figure III-18** for A-432 and **Figure III-19** for A-433. For internal +45-layers in both aged laminates predictions are in good agreement with test data.

Similarly as for NA specimens, the crack density in the surface layers could not be predicted: it is even outside the previously defined bounds. The latter means that the surface layer has different failure properties than the internal layers: it has aged and therefore ρ is much higher than in NA case. It seems that the surface layer of the A-432 composite has aged more than that of the A-433 composite: the crack density at zero loads is higher and it is growing faster in A-432 composite. Partially it could be explained by voids in the 432 providing pathways for oxygen during the aging test.

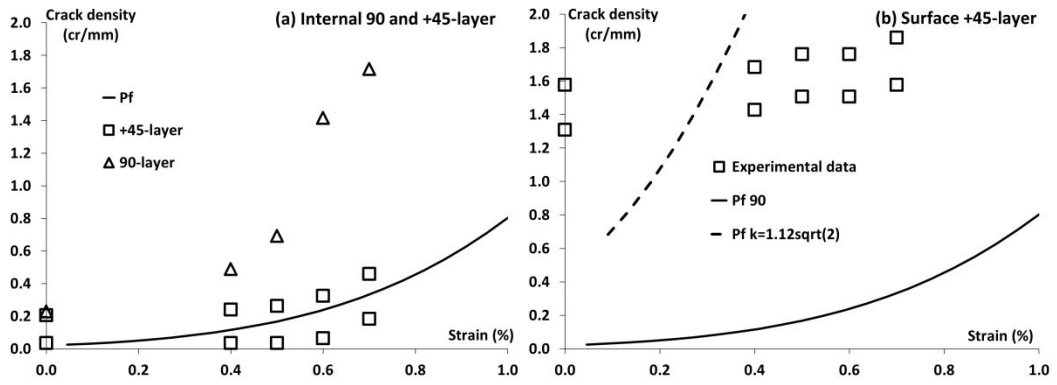


Figure III-18 Microcracking in A-432 composite

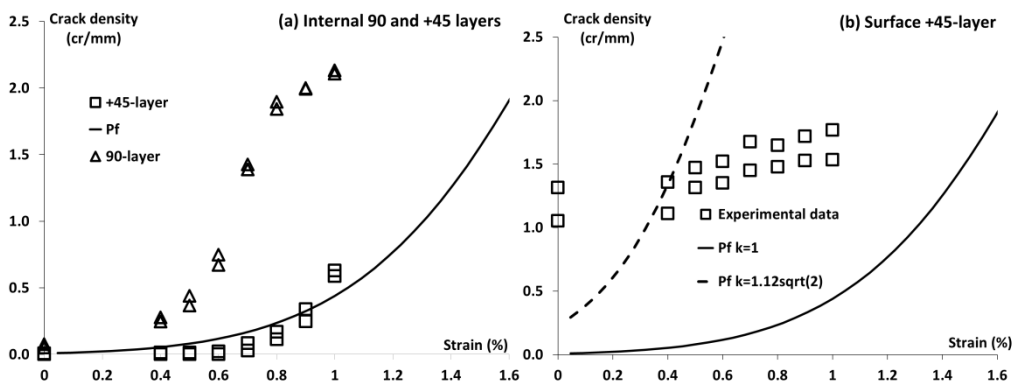


Figure III-19 Microcracking in A-433 composite

The probability of transverse failure in 90-layers of both composites, not aged (NA) and aged (A), can be compared from plots in **Figure III-20**. The behaviour is very similar. Aging has not affected the damage behaviour of 90-layers.

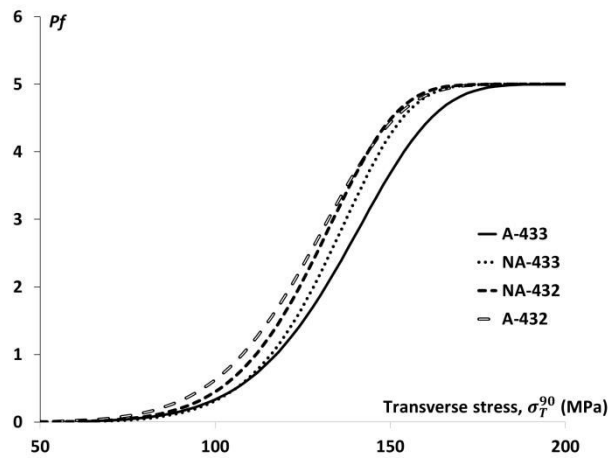


Figure III-20 Probability of transverse failure curves for 90-layers of 432 and 433 composites: not aged (NA) and aged (A)

4.5.4. Extraordinary cracking pattern in -45-layers

In a not damaged quasi-isotropic $[(+45/-45)/(90/0)]_{2s}$ laminate the CLT stresses in +45 and -45-layers are exactly the same and, therefore, the same development of multiple cracking could be expected in both types of layers. Nevertheless, data presented in **Figure III-21a** and **Figure III-22a** show many more cracks in -45 layers than in internal +45-layers.

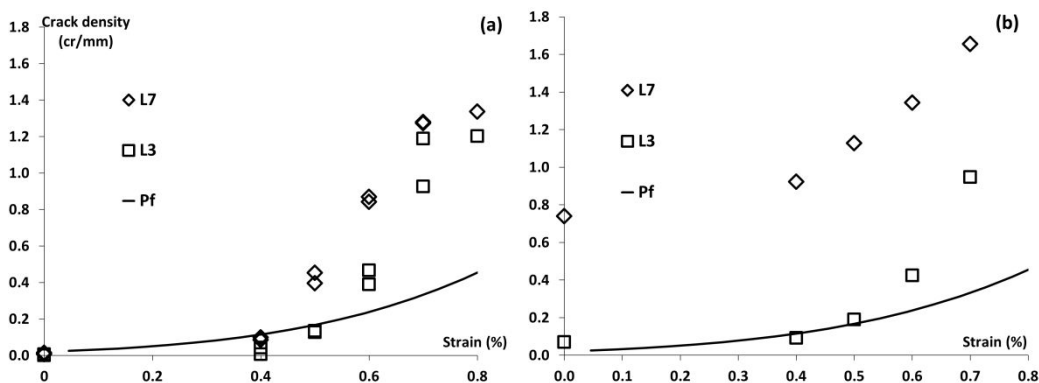


Figure III-21. Cracking in -45-layers of the 432 quasi-isotropic laminate (layers are numbered L3, L7 regarding their position with respect to mid-plane): **a)** NA; **b)** A.

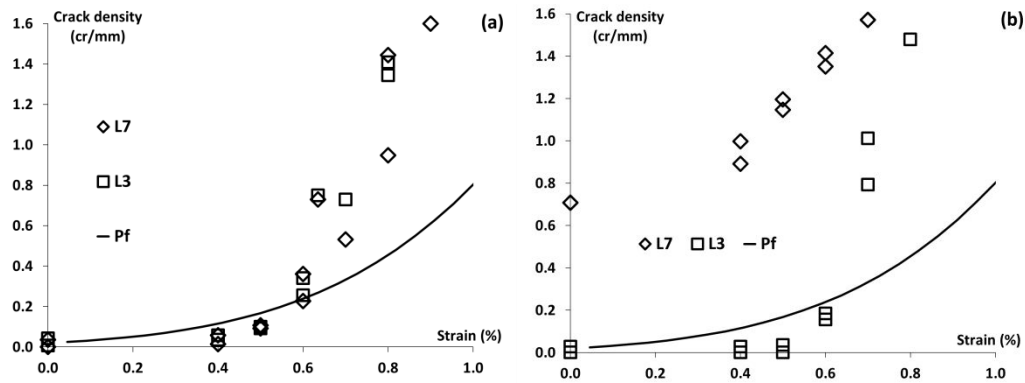


Figure III-22 Cracking in -45-layers of the 433 quasi-isotropic laminate (layers are numbered L3, L7 regarding their position with respect to mid-plane): **a) NA; b) A.**

In these figures the P_f -approach simulations, which describe cracking in +45-layers very well, are shown as solid lines. Crack density is shown separately in L3 layer which is close to the mid-plane and in L7 layer which is close to the surface.

For not aged specimens there is no systematic difference between L3 and L7 layers. The crack density in -45-layers is similar as in +45-layers only in the very beginning of cracking. After 0.6% strain the crack density in -45-layers is almost two times larger than in +45-layers. The only explanation for this difference is in stress concentrations due to damage developing in neighbouring layers. An internal +45-layer has 0- and -45-layers as adjacent layers. There are no cracks in 0-layers (except some thermal cracks) and cracks in the adjacent -45-layer are perpendicular to expected cracks in the +45-layer with small effect of their stress concentrations. In contrary, the -45-layer is surrounded by +45 layer (the same marginal effect from cracks in this layer) and by 90-layer where crack density increases first. Cracks in 90-layers cause strong stress concentration in the adjacent -45-layer. These cracks, often called stitch cracks due to their appearance [31-32], have been observed in mechanical as well as in thermal

fatigue and also in quasi-static loading. There is no difference in cracking of NA-432 and NA-433 laminates.

In aged specimens (A-432 and A-433 in **Figure III-21b** and **Figure III-22b**) the difference in cracking between L7 layers and L3 layers is very large. Whereas in the L3 layers the cracking is in average the same as in not aged specimens, the crack density in L7 layers is much higher. An obvious explanation for that is aging: layers close to the laminate mid-plane have not aged and only the surface layer and the L7 -45-layer are.

5. Conclusions

Micro-damage evolution in two quasi-isotropic CF/polyimide composites for high temperature applications, with different resin composition, was investigated showing two phenomena: thermal fatigue and thermal aging.

Firstly, the increasing intra-bundle crack density during thermal cycling was studied showing that the highest temperature in the cycle which has the lowest thermal stress level is of primary importance for damage developments. To separate the fatigue effects from possible material aging effects during the total time at high temperature, a separate group of specimens was aged for the time equal to the total time at the same highest temperature in the cycling test showing that aging is a part of the total degradation during cyclic loading.

Secondly, the composite failure resistance during aging was analysed using the aging time as a variable. The resistance to cracking reduces with aging time and the crack density after cooling down to room temperature is increasing. Results show a large edge effect in composite degradation: the number of cracks inside the specimen is

much lower than on the edge or in surface layers. Results and observed trends are explained using 3-D FEM edge stress analysis and linear elastic fracture mechanics.

Afterwards, the intralaminar cracking in tensile loading of the same materials was investigated analysing effect of thermal aging at 288°C for 30days.

Numerical analysis and following fractography showed that the intralaminar cracking state on the edge gives a good representation of the damage inside the composite.

Cracking in different layers of a laminate was quantified and analysed using Weibull transverse strength distribution for crack initiation probability. A simplified parameter determination and cracking simulation scheme is suggested and results are compared with Monte-Carlo simulations based on shear lag as well as Hashin's stress models.

Cracking in internal +45-layers could be adequately predicted based on Weibull analysis of 90-layers. The crack density in the surface +45-layer was much higher even for not aged specimens, which is explained by free surface effect on crack initiation.

Cracking in 45-layers adjacent to 90-layer is significantly accelerated by stress concentrations from cracks in the 90-layer.

Aging degraded about 1mm of the composite at the specimen edges (this region was removed before mechanical testing) and also the whole surface layer and the layer next to it whereas failure properties of central layers were not affected.

Chapter IV

Summary, conclusions and perspectives

In the first part of this thesis, the effect of the 0° -tow waviness on axial stiffness of cross-ply non-crimp fabric (NCF) composites is analysed using multiscale approach. The curved 0° and 90° -layers are represented by flat layers with effective stiffness properties and classical laminate theory (CLT) is used to calculate the macroscopic stiffness. The effective 0° -layer stiffness is calculated analysing isolated curved 0° -layers subjected not only to end loading, but also to surface loads. The surface loads are identified in a detailed FE-analysis and approximated by a sinus shaped function with amplitude depending on the waves parameters. The sinus shaped surface loads are then applied to an isolated curved 0° -layer FE-model together with end loading to calculate the effective stiffness of the layer. Finally, the effective 0° -layer stiffness was successfully used to calculate the macroscopic stiffness of the composite proving validity of the approach being used and showing that, without losing accuracy, elastic properties in the 90° -layers with bundle structure can be replaced by the transverse stiffness of the homogenized 90° -layer material.

In another approach, it is shown that the NCF composite knock-down factor characterizing the stiffness degradation has almost the same dependence on wave parameters as the knock-down factor for the curved 0° -layer. Numerical analysis showed that 90° -layer knock-down factor versus amplitude curves for different wavelength can be reduced to one master curve which can be described by a one-parameter expression with the parameter dependent on the used material. This

observation is used to obtain high accuracy for analytical predictions for knock down factors for cases with different wavelength and amplitudes based on two FE calculations only.

Finally, the axial stiffness of a symmetric NCF composite, consisting of $0^\circ/90^\circ$ unit cells with different amplitudes and wavelength of the 0° -layer, is calculated using FEM and also using analytical models with knock-down factors for curved 0° -layers which describes the effect of the local amplitude and wavelength of the 0° -layer on the effective stiffness of the layer in the unit cell. The dependence of the knock-down factor on the presence and waviness in the neighbouring unit cell is accounted for. Rule of mixtures and constant force assumptions are used when appropriate to find the macroscopic stiffness. Analytical modelling is in a good agreement with FEM.

An alternative approach is suggested where one equivalent meso- cell represent the macro-stiffness of the NCF composite. Methods for geometrical parameter determination of the equivalent meso-cell are discussed.

As perspectives for this part, we can say that further efforts are meaningful to develop analytical approximate models for curved beams with sinusoidal surface tractions and also the observed features used in the master curve approach require further investigation regarding their mechanical origin and potential of application to more complex NCF composites with 0° -layer waviness. The study of the effect of the local meso-structure defects on elastic properties can be continued on Poisson's ratio for example.

In the second part of this thesis, the damage in carbon fibre T650 8-harness satin weave fabric composites with thermosetting polyimide resin designed for high service

temperatures is studied. High thermal stresses develop after cooling down to room temperature, which lead to multiple cracking in bundles/layers of the studied quasi-isotropic laminates. The composites were subjected to two ramps of thermal cycling quantifying the increase of crack density in layers. Comparison of two ramps with the same lowest temperature shows that the highest temperature in the cycle has a significant effect on thermal fatigue resistance. During thermal aging tests at 288°C the mechanical properties are degrading with time and the crack density versus aging time was measured. Aging and fatigue effects were separately analysed showing that part of the cracking in thermal cycling tests is related to material aging during the high temperature part of the cycle. Numerical edge stress analysis and fracture mechanics were used to explain observations.

In a second stage, intra-bundle cracking due to tensile transverse thermal stresses was observed in the studied $[(+45/-45)/(90/0)]_{2s}$ laminates after the thermal aging at 288°C for 40 days which caused many new cracks. Both aged and not aged specimens were tested in uni-axial quasi-static tension quantifying damage development. Differences and similarities in cracking in different layers were analysed using probabilistic approaches (simple non-interactive as well as Monte Carlo simulations). It is shown that cracking in off-axis layers not being in contact with the 90-layer can be predicted based on Weibull analysis of the 90-layer, whereas in layer which is in contact with the 90-layer the crack density is much higher due to local stress concentrations caused by cracks in 90-layer. The thermal treatment degraded cracking resistance in the surface layer and in the next layer whereas failure resistance of layers close to the mid-plane did not change.

In perspectives, further study is needed concerning the aging effect on the stiffness and the strength of this material. More aging can be done for more time and higher temperature. The polyimide resin is continued to be developed for resistance to higher temperatures.

Acknowledgments

It is gratefully acknowledged that the work performed in the first part of this thesis is partly funded by the Swedish 5th National Aeronautical Research Program (NFFP5) through the project ReFACT, and also through the Joint European Doctoral Program in Material Science and Engineering (DocMase).

The second part was financially supported by EXCELL project funded by local government of Norbotten, SWEDEN and partial funding from the strategic innovation programme LIGHTer provided by VINNOVA are also acknowledged.

Appendix A

Interface stress amplitude approximate dependence on A/t_0 and L/t_0

Fitting the interface normal and shear stress with **(II-17)** and **(II-18)** respectively, the stress amplitudes σ_{n0} and σ_{nt0} are found. The monotonously decreasing values were fitted with the following function

$$\sigma_{n0}(Pa) = \frac{1}{C_{1n} + C_{2n}\left(\frac{L}{T}\right) + C_{3n}\left(\frac{L}{T}\right)^2} \quad (\text{A.1})$$

Constants determined by fitting

$$C_{2n} = C_{21n} + C_{22n}\left(\frac{A}{T}\right) + C_{23n}\left(\frac{A}{T}\right)^2 \quad (\text{A.2})$$

$$C_{3n} = B_n\left(\frac{A}{T}\right)^{-\alpha} \quad (\text{A.3})$$

The determined values of constants $C_{1n}, C_{21n}, C_{22n}, C_{23n}, B_n, \alpha$ for layers made of composite materials CF/EP1, CF/EP2 and GF/EP are given in **Table A.1**.

Table A.1. Values of constants for fitting maximum value of the interface normal stress ($\varepsilon_1 = 1\%$)

Material	C_{1n}	$C_{2n} = C_{21n} + C_{22n}\left(\frac{A}{T}\right) + C_{23n}\left(\frac{A}{T}\right)^2$			$C_{3n} = B_n\left(\frac{A}{T}\right)^{-\alpha}$	
		C_{21n}	C_{22n}	C_{23n}	B_n	α
CF/EP1	$5.200 \cdot 10^{-9}$	$-4.413 \cdot 10^{-10}$	$-2.612 \cdot 10^{-10}$	$7.900 \cdot 10^{-10}$	$2.337 \cdot 10^{-11}$	0.9339
CF/EP2	$5.400 \cdot 10^{-9}$	$-4.205 \cdot 10^{-10}$	$-3.707 \cdot 10^{-10}$	$8.993 \cdot 10^{-10}$	$2.682 \cdot 10^{-11}$	0.9364
GF/EP	$7.330 \cdot 10^{-9}$	$-2.609 \cdot 10^{-10}$	$-1.487 \cdot 10^{-9}$	$2.009 \cdot 10^{-9}$	$6.704 \cdot 10^{-11}$	0.9423

Amplitudes of shear stress are also fitted using the same type of expression:

$$\sigma_{nt0}(Pa) = \frac{1}{C_{1nt} + C_{2nt} \left(\frac{L}{T}\right) + C_{3nt} \left(\frac{L}{T}\right)^2} \quad (\text{A.4})$$

Parameters C_{1nt} , C_{2nt} and C_{3nt} are described by following functions:

$$C_{1nt} = C_{11nt} + C_{12nt} \exp(-C_{13nt} \frac{A}{T}) \quad (\text{A.5})$$

$$C_{2nt} = C_{21nt} + C_{22nt} \exp(-C_{23nt} \frac{A}{T}) \quad (\text{A.6})$$

$$C_{3nt} = C_{31nt} + C_{32nt} \exp(-C_{33nt} \frac{A}{T}) \quad (\text{A.7})$$

The constants for layers made of the different composite materials found by fitting are given in **Table A.2**.

Table A.2. Values of constants for fitting maximum value of the interface shear stress ($\varepsilon_1 = 1\%$)

Constants	CF/EP1	CF/EP2	GF/EP
C_{11nt}	$1.261 \cdot 10^{-8}$	$1.577 \cdot 10^{-8}$	$-1.074 \cdot 10^{-8}$
C_{12nt}	$-1.316 \cdot 10^{-6}$	$-7.652 \cdot 7$	$-9.064 \cdot 10^{-8}$
C_{13nt}	5.200	4.163	4.229
C_{21nt}	$6.325 \cdot 10^{-10}$	$1.121 \cdot 10^{-9}$	$3.984 \cdot 10^{-9}$
C_{22nt}	$2.433 \cdot 10^{-7}$	$1.513 \cdot 10^{-7}$	$3.107 \cdot 10^{-8}$
C_{23nt}	5.880	5.065	5.356
C_{31nt}	$1.124 \cdot 10^{-10}$	$8.364 \cdot 10^{-11}$	$-4.166 \cdot 10^{-11}$
C_{32nt}	$-6.445 \cdot 10^{-9}$	$-3.716 \cdot 10^{-9}$	$-2.616 \cdot 10^{-10}$
C_{33nt}	6.180	5.205	4.568

References

- [1] Varna J, Berglund LA. Mechanics of fiber composite materials-micromechanics, laminate theory and failure analysis. Division of Polymer Engineering. Luleå University of Technology.
- [2] Mattsson D., Joffe R., Varna J. Damage in NCF composites under tension: effect of layer stacking sequence. Fracture of composite materials 2008; 75(9):2666-2682.
- [3] Mattsson D. Mechanical performance of NCF composites. Luleå University of Technology Doctoral thesis 2005.
- [4] Carmisciano S., De Rosa IM., Sarasini F., Tamburrano A., Valente M. Basalt woven fiber reinforced vinylester composites: Flexural and electrical properties. Materials and design 2011; 32: 337-342.
- [5] Hogg PJ., Ahmadnia A., Guild FJ. The mechanical properties of non-crimped fabric-based composites. Composites 1993; 24 (5): 423-432.
- [6] Hogg PJ., Woolstencroft DH. Non-crimp thermoplastic composite fabrics: aerospace solutions to automotive problems. 7th Ann ASMIESD advanced composites conference Detroit 1991: 339-349.
- [7] Mounitz AP., Leong KH., Herzberg I. A review of the effect of stitching on the in-plane mechanical properties of fiber-reinforced polymer composites. Composites Part A 1997; 28: 979-991.

[8] Mattsson D., Joffe R., Varna J. Methodology of characterization of internal structure parameters governing performance in NCF composites. *Composites Part B: Engineering* 2007; 38: 44-57.

[9] Tan P., Tong L., Steven GP. Modeling for predicting the mechanical properties of textile composites-A review. *Composites Part A* 1997; 28A: 903-922.

[10] Dixit A., Harlal SM. Modeling techniques for predicting the mechanical properties of woven-fabric textile composites-A review. *Mechanics of composite materials* 2013; 49.

[11] Barkanov E. Introduction to the finite element method. Institute of materials and structures, Faculty of civil engineering, Riga Technical University 2001.

[12] Ritz W. über eine neue metode zur lösung gewisser variations problem der matematischen physik. *Journal für die reine und angewandte Mathematik* 2009; 1909(135): 1-61.

[13] Tan P., Tong L., Steven GP. Modeling for predicting the mechanical properties of textile composites- a review. *Composites Part A* 1997; 28A: 903-922.

[14] Naik NK., Shembekar PS. Elastic behavior of woven fabric composites: I-Lamina analysis. *Journal of composite materials* 1992; 26: 2197-2225.

[15] Shembekar PS., Naik NK. Elastic behavior of woven fabric composites: II-Laminate analysis. *Journal of composite materials* 1992; 26: 2226-2246.

[16] Naik NK., Shembekar PS. Elastic behavior of woven fabric composites: III-Laminate design. *Journal of composite materials* 1992; 26: 2523-2541.

- [17] Ishikawa T., Chou T. Elastic behavior of woven hybrid composites. *Journal of Composite Materials* 1982; 16: 1982, 2-19.
- [18] Ishikawa T., Chou T. One dimensional micromechanical analysis of woven fabric composites. *AIAA* 1983; 21: 1714-1721.
- [19] Ishikawa T., Chou T. Stiffness and strength behavior of woven fabric composites. *Journal of material sciences* 1982; 17: 3211-3220.
- [20] Byström J., Jekabsons N., Varna J. An evaluation of different models for prediction of elastic properties of woven composites. *Composites Part B* 2000; 31: 7-20.
- [21] Tessitore N., Riccio A. A novel FEM model for biaxial non-crimp fabric composite materials under tension. *Computers and structures* 2006; 84: 1200-1207.
- [22] Drapier S., Wisnom MR. A finite element investigation of the interlaminar shear behavior of non-crimp-fabric-based composites. *Composites Science and Technology* 1999; 59: 2351-2362.
- [23] Edgren F., Asp LE. Approximate constitutive model for non-crimp fabric composites. *Composites Part A* 2005; 36: 173-181.
- [24] Mattsson D., Varna J. Average strain in fiber bundles and its effect on NCF composite stiffness. *Journal of Engineering Materials and Technology* 2007; 129: 211-219.
- [25] Kim M., Song J. Geometry effect on mechanical properties of woven fabric composites. *Journal of Central South University of Technology* 2011; 18: 1985-1993.

[26] TamiStinchcomb WW., Reifsnider KL. Fatigue damage mechanisms in composite materials. Fatigue mechanisms, ASTM STP 675. Philadelphia, PA: American Society for Testing and Materials; 1975.

[27] Tamin MN. Damage and fracture of composite materials and structures. Advanced Structured Materials 2012; 17: 166-167.

[28] Loukil MS. Experimental and numerical studies of intralaminar cracking in high performance composites. Luleå University of Technology doctoral thesis 2013; 4.

[29] Edgren F., Mattsson D., Asp LE., Varna J. Formation of damage and its effects on non-crimp fabric reinforced composites loaded in tension. Composites Science and Technology 2004; 64: 675-692.

[30] Marklund E., Asp LE., Varna J. Modeling stiffness and strength of non-crimp fabric composites semi-laminar analysis. In: Lomov SV (ed). Non-crimp fabric Composites: manufacturing, properties and application 2011; 17: 403-438.

[31] John S., Herszberg I., Coman F. Longitudinal and transverse damage taxonomy I woven composite components. Composites Part B 2001; 32: 659-668.

[32] Gao F., Boniface L., Ogin SL., Smith PA., Greaves RP. Damage accumulation in woven-fabric CFRP laminates under tensile loading: Modeling the effect of damage on Macro-mechanical properties. Composites Science and Technology 1999; 59: 137-145.

[33] Lomov SV., Ivanov DS., Truong TC., Verpoest I., Baudry F., Vanden Bosche K., Xie H. Experimental methodology of study of damage initiation and development in textile composites in uniaxial tensile test. Composites Science and Technology 2008; 68: 2340-2349.

[34] Mikhaluk DS., Truong TC., Borovkov AI., Lomov SV., Verpoest I. Experimental observations and finite element modeling of damage initiation and evolution in carbon/epoxy non-crimp fabric composites. *Engineering Fracture Mechanics* 2008; 75: 2751-2766.

[35] Scida D., Aboura Z., Benzeggagh ML. The effect of ageing on the damage events in woven-fiber composite materials under different loading conditions. *Composites Science and Technology* 2002; 62: 551-557.

[36] Leong KH., Ramakrishna S., Huang ZM., Bibo GA. The potential of knitting for engineering composites- a review. *Composites Part A* 2000; 31: 197-220.

[37] Dransfield K., Baillie C., Yiu-Wing M. Improving the delamination resistance of CFRP by stitching – a review. *Composites Science and Technology* 1994; 50: 305-317.

[38] Dransfield K., Jain L., Mai Y-W. On the effects of stitching in CFRPs- I. Mode I delamination toughness. *Composites Science and Technology* 1998; 58: 815-827.

[39] Jain L., Dransfield K., Mai Y-W. On the effects of stitching in CFRPs- II. Mode II delamination toughness. *Composites Science and Technology* 1998; 58: 829-837.

[40] Drapier S., Wisnom MR. Finite-element investigation of the compressive strength of non-crimp-fabric based composites. *Composites Science and Technology* 1999; 59: 1287-1297.

[41] Miller AJ. The effect of microstructural parameters on the mechanical properties of non-crimp fabric composites. M.Ph. thesis Cranfield University School of Industrial and Manufacturing Science 1996.

- [42] Kurath P., Karayaka M. Deformation and failure behaviour of woven Composite Laminates. *Journal of Engineering Materials and Technology* 1994; 116: 222-232.
- [43] Wang Y., Li J., Do PB. Properties of composites laminates reinforced with E-glass multiaxial non-crimp fabrics. *Journal of Composites Material* 1995; 29(17): 2317-2333.
- [44] Bibo GA., Hogg PJ., Kemp M. Mechanical characterisation of glass- and carbon-fibre-reinforced composites made with non-crimp fabrics. *Composites Science and Technology* 1997; 57(9-10): 1221-1241.
- [45] Chun HJ., Ryu KS., Byun JH. Predictions of Elastic Properties of Multi-axial Warp Knitted Fabric Composites. *Key Engineering Materials* 2004; 261-263(II): 1499-1504.
- [46] Robitaille F., Clayton BR., Long AC., Souter BJ., Rudd CD. Geometric modelling of industrial preforms: warp-knitted textiles. *Proceedings of the Institution of Mechanical Engineers, Journal of Materials: Design and Applications* 2000; 214: 71-90.
- [47] Klopp K., Veihelmann B., Kolkmann A., Laourine E., Gries T. Use of reinforcement textiles in fiber reinforced plastics. *Technical Textiles* 2003; 46: 59-63.
- [48] Zrida H., Marklund E., Varna J., Ayadi Z. Effective stiffness of 0°-layer for stiffness determination of cross-ply non-crimp fabric composites. *Journal of reinforced plastics and composites* 2014; 33: 1339-1352
- [49] Owens GA, Schofield SE. Thermal cycling and mechanical properties assessment of carbon fibre fabric reinforced PMR-15 polyimide laminates. *Composites Science and Technology* 1988;33: 177-190.
- [50] Kim RY., Crasto SA., Schoeppner GA. Dimensional stability of composite in a space thermal environment. *Composite Science and Technology* 2000;60 (12-13): 2601-2608.

- [51] Tsotsis TK., Keller S., Lee K., Bardis J., Bish J. Aging of polymeric composite specimens for 5000 hours at elevated pressure and temperature. *Composite Science and Technology* 2001;61: 75-86.
- [52] Bowles DE., Shen J. Thermal cycling effects on the dimensional stability of P75 and P75-T300(Fabric) hybrid graphite/epoxy laminates. In: 33rd international SAMPE symposium. March 7-10, 1988.
- [53] Papanicolaou GC., Koutsomitopoulou AF., Sfakianakis A. Effect of thermal fatigue on the mechanical properties of epoxy matrix composites reinforced with Olive pits powder. *Journal of Applied Polymer Science* 2012;124: 67-76.
- [54] Kobayashi S., Terada K., Ogihara S., Takeda N. Damage-mechanics analysis of matrix cracking in cross-ply CFRP laminates under thermal fatigue. *Composite Science and Technology* 2001;61: 1735-1742.
- [55] Giannadakis K., Varna J. Effect of thermal aging and fatigue on failure resistance of aerospace composite materials. In: *IOP Conference Series: Materials Science and Engineering* 5, 2009.
- [56] Stutz HC. Lifetime assessment of epoxies by the kinetics of thermal degradation. *Journal of Applied Polymer Science* 2004; 91: 1881-1886.
- [57] Bechel VT., Camping JD., Kim RY. Cryogenic /elevated temperature cycling induced leakage paths in PMCs. *Composites Part B* 2005;36: 171-182.
- [58] Bellenger V., Decelle J., Huet N. Ageing of a carbon epoxy composite for aeronautic applications. *Composites Part B* 2005; 36: 189-194.
- [59] Lee SH., Nam JD., Ahn K., Chung KM., Seferis JC. Thermo-oxidative stability of high performance composites under thermal cycling conditions. *Journal of Composite Materials* 2001;35: 433-454.

- [60] Lévêque D., Schieffer A., Mavel A., Maire JF. Analysis of how thermal aging affects the long-term mechanical behavior and strength of polymer-matrix composites. *Composite Science and Technology* 2005;65: 395-401.
- [61] Marceau C., Hilaire B. Thermal ageing of PMR15 polyimide matrix. *Polymer Journal* 1993;34: 2458-2459.
- [62] Mangalgi PD. Polymer-matrix composites for high-temperature applications. *Defence Science Journal* 2005;55: 175-193.
- [63] Tsampas S.A., Fernberg PS. and Joffe R., "Mechanical performance of novel high T_g polyimide matrix carbon fibre-reinforced laminates" 20th International conference on composite materials, Copenhagen, 19-24 July 2015.
- [64] Varna J., Joffe R., Berglund LA., Lundström S. Effects of Voids on Failure Mechanisms in RTM Laminates, *Composite Science and Technology* 1995;53: 241-249.
- [65] Sisodia S., Gamstedt EK., Edgren F., Varna J. Effects of voids on quasi-static and tension fatigue behaviour of carbon-fibre composite laminates. *Journal of Composite Materials* 2014.
- [66] Broek D. Elementary engineering fracture mechanics. Editor. Martinus Nijhoff publishers The Hague Bosten London. Kluwer Academic Publishers 1982.
- [67] Berglund LA., Varna J., Yuan J. Transverse Cracking and Local Delamination in [04/90_n]S and [90_n/04]S Carbon Fiber / Toughened Epoxy Laminates. *Journal of Reinforced Plastic and Composites* 1992;11: 643-660.
- [68] Varna J. Modeling Mechanical Performance of Damaged Laminates. *Journal of Composite Materials* 2013;47(20-21): 2443-2474.

- [69] Joffe R., Krasnikovs A., Varna J. COD-based simulation of transverse cracking and stiffness reduction in [S/90n]s laminates. *Composite Science and Technology* 2001; 61: 637-656.
- [70] Varna J. Quantification of damage and evolution modeling in multidirectional laminates. In *Proceedings of the 27th RISÖ International symposium on material science*. Roskilde, Denmark, 2006. p.349-356.
- [71] Varna J. Micro damage Modeling in laminates, in - *Damage Growth in Aerospace Composites*. Springer 2015. p.141-173.
- [72] Quaresimin M., Carraro PA., Mikkelsen LP., Lucato N., Vivian L, Brøndsted P, Sørensen BF, Varna J, Talreja R. Damage evolution under cyclic multiaxial stress state: A comparative analysis between glass/epoxy laminates and tubes. *Composites Part B: Engineering* 2014; 61: 282-290.
- [73] Bechel VT. Permeability and damage in unloaded cryogenically cycled PMCs, 46th AIAA/ASME/ASCE/AHS/ASC Structures. In: *Structural Dynamics and Materials conference*. Austin, Texas, April, 2005.
- [74] Ben Kahla H., Varna J. Microcracking in layers of composite laminates in cyclic loading with tensile transverse and shear stress components. In: *Proceedings of 20th International Conference on Composite Materials*, 2015.
- [75] Paris F., Blazquez A., McCartney LN., Mantic V. Characterization and evolution of matrix and interface related damage in [0/90]s laminates under tension. Part I: Numerical predictions, *Composites Science and Technology*, 2010;70 :1168-1175.
- [76] Varna J. and L.A. Berglund, "*Two-Dimensional Transverse Cracking in [0m/90n]S Cross-Ply Laminates*," *European Journal of Mechanics A/Solids*,12 No5, 1993, 699-723.

[77] Yongxin Huang, Y., Varna J, Talreja R. Statistical Methodology for Assessing Manufacturing Quality Related to Transverse Cracking in Cross Ply Laminates, Composites Science and Technology.2014; 95:100-106.

[78] Herraez M., Mora D., Naya F., Lopes C.S., Gonzales C., LLorca J. Transverse cracking of cross-ply laminates: A computational micromechanics perspective. Composites Science and Technology, 2015; 110 : 196-204.

[79] Bechel V.T., Negilski M. and James J. Limiting the permeability of composites for cryogenic applications, Composites science and Technology. 2006; 6 (13): 2284-2295.

[80] Loukil M., Ayadi Z. and Varna J. ESPI analysis of crack face displacements in damaged laminates, Journal of Composites Science and Technology; 2014;94(9):80-88.

Titre : Les composites avec mesostructure en faisceaux : Propriétés élastiques et endommagement

Mots clés : Les composites textiles, endommagement, mécanique de rupture, rigidité, défauts de mesostructure.

Résumés : Les propriétés élastiques et la résistance à l'endommagement des composites textiles avec mesostructure en faisceaux ont été étudiées dans cette thèse.

Le premier chapitre de cette thèse traite la modélisation des propriétés élastiques des composites NCF (Non-Crimp Fabric) pour étudier l'effet des défauts de mesostructure sur la dégradation des propriétés mécaniques. Un modèle pour la mesostructure des composites NCF est réalisé pour étudier l'effet de l'ondulation sur la réduction de la rigidité. Cette dernière est dominée par la réduction de la rigidité de la couche 0° . La rigidité effective de la couche 0° peut être déterminée soit par modélisation d'une seule couche ondulée soumise à un chargement réparti, qui reproduit son interaction avec les couches voisines, avec application des symétries dans les conditions aux limites, ou en utilisant une approche de la courbe maîtresse. Une expression analytique est suggérée. Cette expression permet la détermination du facteur de réduction de rigidité pour toute longueur d'onde et amplitude donnés.

L'initiation et le développement des endommagements sont présentés dans le deuxième chapitre, où les composites textiles désignés aux applications à haute température ont été étudiés dans des conditions thermiques sévères pour vérifier leur stabilité thermique et leur résistance aux endommagements thermiques.

Finalement, la performance mécanique des composites destinés pour les hautes températures, est étudiée, et l'effet du vieillissement thermique a été analysé. Des modèles 3D ont été réalisés par éléments finis pour expliquer l'effet des bords sur l'évolution des fissures observées lors des essais de traction. En outre, les différences et les similarités au niveau de fissuration dans les différentes couches sont analysés à travers des approches probabilistes (Monte Carlo, Hashin and shear lag) et aussi la mécanique de la rupture.

Title: Composites with bundle mesostructure: elastic properties and damage.

Key words: Textile composites, damage, fracture mechanics, stiffness, mesostructure defects.

Summary: Textile composites with bundle meso-structure have been studied in this thesis for elastic properties and damage investigations.

The first chapter of this thesis deals with elastic properties modeling for Non-crimp fabric (NCF) based composites for investigating the effect of meso-structure defects on mechanical properties degradation. The objective of the work is to formulate a model for the NCF composite mesostructure in an attempt to investigate the effect of the waviness on stiffness reduction. The cross-ply NCF composite stiffness reduction is dominated by the stiffness reduction of the 0° -layer. The 0° -layer effective stiffness can be determined either by modeling a single curved tow subjected to distributed load, to reproduce its interaction with the neighboring layers, together with symmetry boundary conditions, or using a master curve approach, where a knock down factor is introduced to characterize the stiffness reduction and analytical expression is suggested. This expression allows for determination of knock down factor for any given wavelength and amplitude of the waviness.

The damage initiation and development is presented in the second chapter, where woven fabric composites designated for high temperature application were investigated under severe thermal conditions to study their thermal stability and their resistance to thermal damage.

Finally, the mechanical performance of the composites designated to high temperature applications was studied. The effect of aging was also investigated. 3D models were realized with Finite elements in order to explain the edge effect on the evolution of the cracks observed during the tensile tests. In addition, the differences and similarities in cracking in different layers were analysed using probabilistic approaches (a simple one as well as Monte Carlo simulations with Hashin's and also shear lag model) and fracture mechanics arguments.